Fundamental and Applied Studies on Molecular Bottlebrushes with Particular Reference to Side-Chain Conformation and Dynamics

Yuji Kinose

2021

Contents

Chapter 1

General Introduction

1-1. Structure and Interaction of Polymer

1-1-1. Conformation and Dynamics of Linear Chains

Polymer, which is a molecule with a high molecular weight, is as important a material as ceramics and metals. Polymers are lightweight materials and exhibit high moldability and both chemical and impact resistance. Generally, their physical properties are derived from their conformations, which are sometimes compared to strings. However, none of the possible conformations of a polymer can be described because its main chain consists of many covalent bonds. To analyze physical properties from the viewpoint of its conformation, the mean square end-to-end distance $\langle R^2 \rangle$ and mean square radius of gyration $\langle S^2 \rangle$ are widely used as indices of polymer conformation. Wormlike chain model[1] is one of conformation models which represent the conformation of a real polymer. In this model, the main chain of the polymer is considered an elastic wire with continuous curves. Given the parameter λ^{-1}, which represents the stiffness of the main chain, $\langle R^2 \rangle$ and $\langle S^2 \rangle$ are represented by the following equations:[1]

$$\langle R^2 \rangle = \frac{1}{\lambda^2}\left\{\lambda L - \frac{1}{2}[1 - \exp(-2\lambda L)]\right\}$$

$$\langle S^2 \rangle = \frac{1}{\lambda^2}\left\{\frac{\lambda L}{6} - \frac{1}{4} + \frac{1}{4\lambda L} - \frac{1}{8\lambda^2 L^2}[1 - \exp(-2\lambda L)]\right\}$$

Concerning the dilute solution, the self-diffusion coefficient of polymer molecules and the viscosity of the solution depend on the properties of isolated polymer (e.g., $\langle S^2 \rangle$). However, this may not apply to the case of concentrated solutions because of the intramolecular interaction (e.g., entanglement).

In the rheological measurements for bulk polymers with low molecular weights, micro-Brownian motion in the glassy regime and the change in the relative position of polymers in the flow regime are observed at high frequency (or low temperature) and low frequency (or high temperature), respectively. Between these regimes, the glass transition appears, where segmental motion of the polymer starts to occur. In contrast, for polymers with high molecular weights, the rubbery plateau region appears between the flow regime and the glass transition. In this area, the change in the relative position is suppressed by the entanglement between polymers (Figure 1-1).

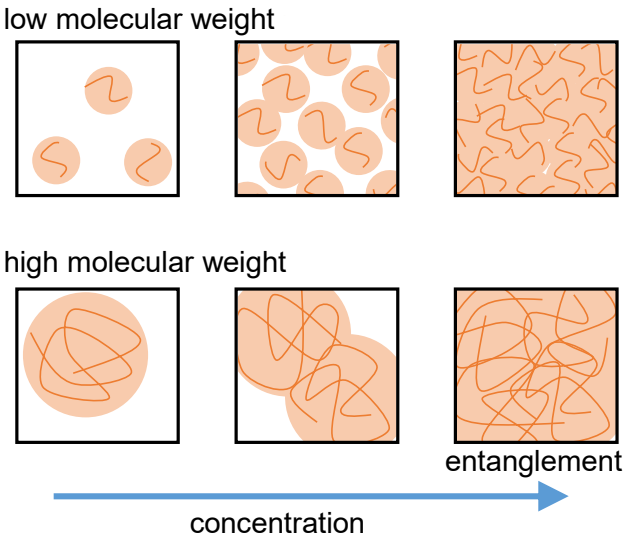

Figure 1-1. Schematic illustrations of concentration-dependent entanglement of short- and long-chain polymers.

In polymer melts, the conformational distribution of the entire system is in an equilibrium state, although each polymer molecule continuously changes its conformation owing to thermal motion. Immediately after stress is applied to distort the melt, the conformational distribution is shifted to a nonequilibrium state to generate stress. Thereafter, the conformational distribution returns to the equilibrium state through the above hierarchical motion. In the case of

a polymer with a high molecular weight, the relaxation time is elongated because the returning to equilibrium state is disturbed by their entanglement.

1-1-2. Some Characteristics of Topologically Different Polymers

The rheological properties of polymers are determined not only by their lengths but also by their branching modes. The relaxation process of the linear polymer is explained by the reptation motion in which the polymer can move along a virtual tube. In the case of polymers with branched chains such as H-shaped polymers, graft polymers, star polymers, and dendrimers, the relaxation mechanism becomes complicated because their conformations are different from those of simple linear polymers. For instance, a star polymer with long arms shows a rubbery plateau attributed to side-chain entanglement.[2] On the other hand, the arms of the dendrimer do not entangle with other polymers to exhibit the Newtonian behavior.[3] Additionally, the polymer topology can change the rheological properties. Ring polymers, which are the simplest in structure and topologically different from linear polymers, exhibit lower viscosity than linear polymers with equivalent molecular weights, which can be attributed to the ring architecture.[4]

As described above, the polymer architecture affects their conformation and rheological properties. Similarly, polymer brushes on solid surfaces exhibit intriguing rheological properties and other properties derived from viscoelasticity, for example, tribology, because their conformation is restricted by surface and neighboring brush polymers. Therefore, these properties depend not only on the composition and molecular weight but also on the density of the graft polymer. In a good solvent, swollen graft polymers are categorized into three regimes based on their graft density: dilute, semi-dilute, and concentrated regimes (Figure 1-2).[5] In a dilute regime, the low-density graft polymer does not interact with each other and has a mushroom conformation. With increasing graft density, graft polymers interact with each other and alter their conformation.

In the semi-dilute regime, the free energy interactions between neighboring polymers can be represented mainly by a binary interaction, and their equilibrium thickness (L_e) is described by the following equation:

$$L_e \propto n\sigma^{1/3}$$

Here, n and σ represent the degree of polymerization and graft density, respectively. When the graft density is further increased and enters the concentrated regime (over 10% of the surface occupancy), the L_e is described by the following equation:

$$L_e \propto n\sigma^{1/2}$$

Finally, graft polymers are extended to almost their full length.

The degree of such chain extension depends on the balance of the osmotic pressure derived from the mixing entropy and the tensile stress derived from conformational entropy. In the concentrated regime, the osmotic pressure and tensile stress are extremely strong. Hence, even if two concentrated polymer brushes (CPBs) contact each other, they will not interpenetrate each other because the conformational-entropy loss overwhelms the mixing-entropy gain of each polymer brush. By contrast, when CPB is compressed, repulsive resistance will occur owing to strong osmotic pressure. These properties provide intriguing functions to the CPB: definite size exclusion in the swollen or dry state with a definite threshold of molecular weight, good biocompatibility in aqueous systems, and extremely low friction and excellent lubrication in a good solvent.

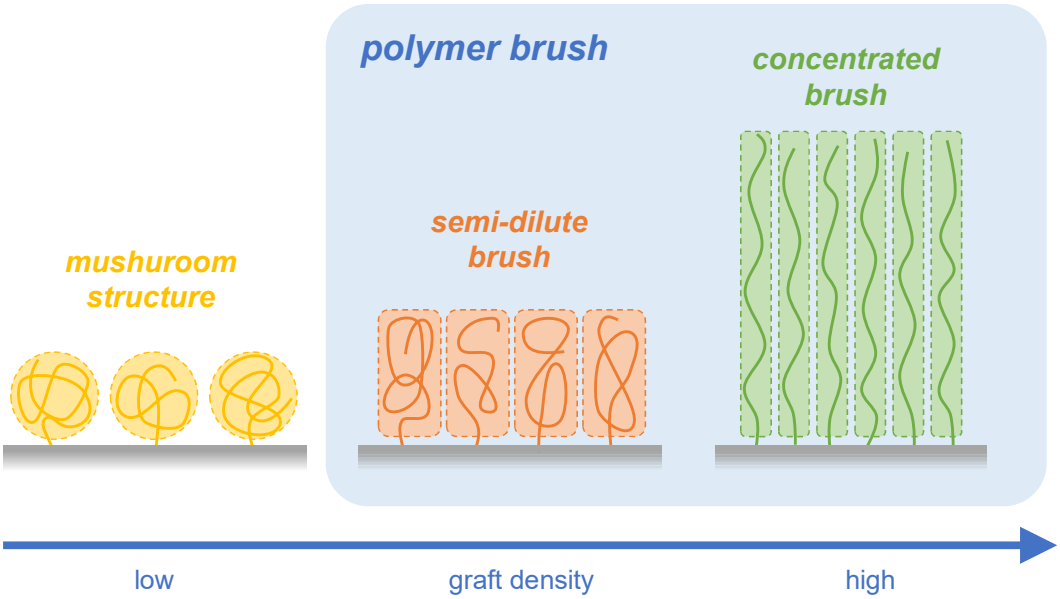

Figure 1-2. Schematic illustrations of polymers end-grafted on surface.

1-2. Particular Issues on Bottlebrushes

1-2-1. Synthetic Routes

A graft polymer with dense side chains is called a bottlebrush. A variety of synthetic strategies of bottlebrushes have been developed using precision polymerization techniques including controlled radical polymerization. From the viewpoint of their fundamental study and application, it is generally necessary to introduce side chains with low polydispersity to the main chain. Currently, there are three main strategies for precision synthesis of bottlebrushes which meet the requirement: grafting-from, grafting-to, and grafting-through methods (Figure 1-3). In the grafting-from method, a polymer is synthesized as the main chain, and then side chains are grown from the initiating groups densely tethered at the main chain by living polymerization.[7,8] In the grafting-to method, low-polydispersity polymers functionalized at one terminal end are coupled with the functional group densely tethered at the polymer as the main chain.[9] In the

grafting-through method, low-polydispersity macromonomers, which have polymerizable groups at one end, are synthesized and then polymerized.[10]

These methods have advantages and disadvantages. In the grafting-from method, the synthesis of a bottlebrush with a very long side chain and purification of products can be easily achieved. However, crosslinking intramolecularly between side chains of a bottlebrush or intermolecularly between bottlebrushes can occur if the polymerization of side chains is not appropriately controlled.[7] Additionally in some cases, it is difficult to precisely determine the molecular characteristics of side chains, for example, molecular weights and density of side chains, when side-chain components are chemically too weak against decoupling reactions of side chains from the main chain. This is not the case with the grafting-to method, in which polymers as side chains can be characterized in advance of the synthesis of the bottlebrush. However, it is difficult in this method to achieve both high molecular weight and high density of side chains owing to its steric repulsion, although improvements were carried out by a click reaction with an excellent reaction yield and high substrate specificity.[11-13] The grafting-thorough method is suitable for synthesizing a structurally well-defined bottlebrush with a side chain tethered at every repeating unit of the main chain.[14] However, increasing the molecular weight of the macromonomer makes polymerization difficult because of the steric repulsion between the bottlebrush and macromonomer, similarly to the situation in the grafting-to method. In such cases, ring-opening metathesis polymerization[15] or copolymerization with a low-molecular-weight monomer[16] is more effective approaches than the polymerization of vinyl monomers because its contour length per side chain is longer than that of vinyl polymer. The above three methods require synthetic devices such as orthogonal polymerization and functionalization of the polymer. Hence, the method should be properly adopted according to the chemical composition and the application.

1-2-2. Precision Polymerization Techniques

It is important to select a proper chemical structure of the main chain to synthesize a structurally well-defined bottlebrush. In fundamental research, the main chain of bottlebrushes is widely synthesized by controlled radical polymerization.[17,18] The process of growth in controlled radial polymerization is the same as that in free radical polymerization; after the generation of an initiating radical, a polymer grows through multiple addition of monomers. Finally, the growing polymer becomes a dead polymer by a disproportionation reaction or recombination reaction. The rate of such termination reactions depends on the concentration and diffusion rate of the radical species. The difference between controlled and free radical polymerizations is whether or not the reversible deactivation of radical species is included. In correctly controlled polymerization, the initiation reaction occurs almost simultaneously, generating radical species, most of which are readily converted to chemically stable and potentially active “dormant” species. The dormant species sometimes reproduce to radical species to add monomers. All growing ends of the polymer are converted alternately to the dormant and active states, resulting in uniform growth. When the radical concentration is sufficiently suppressed and a sufficient number of dormant species is included, the contribution of irreversible termination reactions becomes negligibly small. Thus, in this case, the radical concentration is constant during polymerization, the degree of polymerization is proportional to the monomer conversion, and the polydispersity index is low enough to meet our demand.

In the grafting-through method, ring-opening metathesis polymerization with a monomer having a norbornene skeleton is widely adopted.[15] This reaction is a type of olefin metathesis polymerization where carbon-carbon double bonds are reconnected. From the viewpoint of synthesis of the bottlebrush, one of the most important features of this polymerization is that it can synthesize polymers with long contour lengths per repeating unit.

This reduces the steric repulsion between side chains to proceed with polymerization with more bulky macromonomers as compared with radical polymerization of vinyl monomers. Another feature of ring-opening metathesis polymerization is its high block efficiency, which is suitable for synthesis of the block bottlebrush mentioned below.

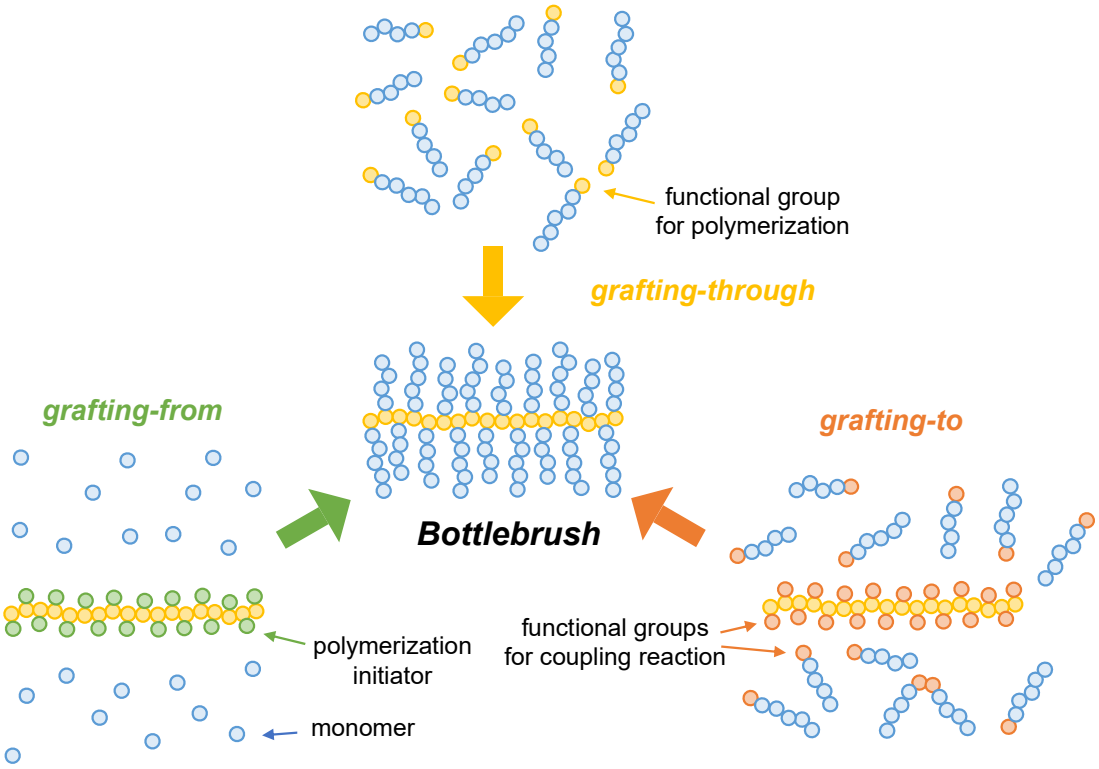

Figure 1-3. Schematic of synthesis methods of bottlebrush.

1-2-3. Novel Functions

A bottlebrush exhibits distinct functions owing to its thick and stiff cylindrical shape. An example of utilizing its stiffness is the high-performance elastomer composed of a cross-linked bottlebrush.[19] Common elastomers form continuous networks by crosslinking polymers, and the elasticity depends on the density of the crosslinking point; the lower the density of the crosslinking

point, the softer the elastomer. When the crosslinking reaction proceeds, the chain entanglements lead to topological crosslinking. At this point, the bottlebrush is advantageous because the dense side chain shows weak interpenetration, and the stiff main chain can prevent entangling to reduce crosslinking points.

The coating layer composed of bottlebrushes exhibits properties similar to those of CPB (e.g., low-friction/good-lubrication property[20]) since a bottlebrush has dense side chains. An articular cartilage is a good example to prove this point of view. The cartilage consists of the aggregate of hyaluronic acid and proteoglycans reinforced by collagen fiber in the human body[21,22] and acts as a tough and low friction material owing to electrostatic interaction.[23] To imitate the articular cartilage, Tsujii and coworkers fabricated a composite of a bottlebrush and a cellulose nanofiber with graft chains and demonstrated its toughness as well as low friction and good lubrication in water, which are derived from stiff cellulose and dense side chains of the bottlebrush, respectively. The important distinction between a bottlebrush and a CPB is the geometry of the surface on which chains are tethered. The former is a one-dimensional strand, and the latter is a two-dimensional plane. The "effective" graft density of CPB on the flat surface should not depend on the distance from the chain-tethered surface. In contrast, as the graft chain becomes longer, the "effective" side-chain density of a bottlebrush decreases because the outermost surface expands cylindrically from the main chain. In the above-mentioned composite of cellulose nanofibers and bottlebrushes, the longer the side chain, the higher the friction coefficient.

1-3. "Hetero" Bottlebrushes with different kinds of side chains

As schematically illustrated in Figure 1-4, some bottlebrushes are equipped with multiple components and classified as "hetero types" in this thesis.[24] They can obtain additionally

novel structure and properties quite different from “homo” bottlebrushes consisting of the single component of side chains, particularly when their components are immiscible. There exist different categories of hetero bottlebrushes depending on the position and sequence of different kinds of side chains along the main chain. When the side chains consist of block copolymer, the bottlebrush is called a core-shell bottlebrush. When different kinds of side chains are segmentally connected to the main chain, i.e., homo bottlebrushes of different side chains are connected at the main-chain end, such a hetero one is called a block bottlebrush. A hetero type with different kinds of side chains homogenously or statistically randomly connected to the main chain is called a mixed bottlebrush. Especially, when the side chains of a mixed bottlebrush undergo intramolecular microphase separation, the bottlebrush is called as Janus bottlebrush.[25]

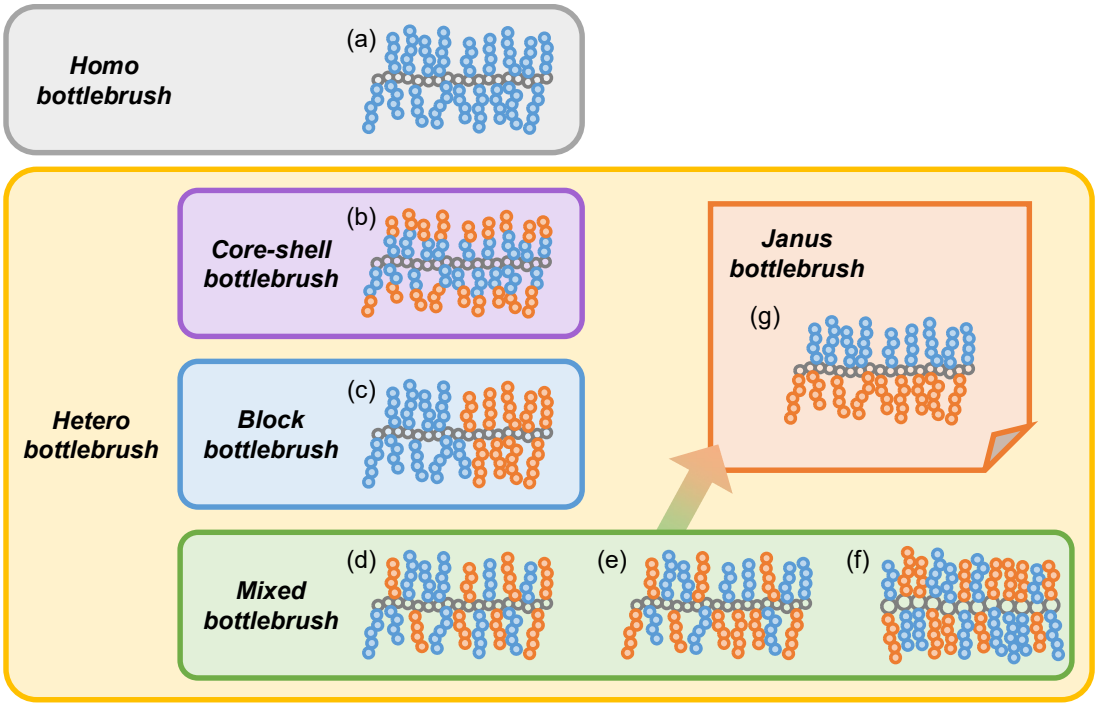

Figure 1-4. Categories of bottlebrushes of different architectures: homo type (a) and hetero types including (b) core-shell bottlebrush, (c) block bottlebrush, (d) random/statistical bottlebrush, (e) sequentially controlled bottlebrush, (f) bottlebrush with two kinds of side chains at every repeating unit, and (g) Janus bottlebrush intramolecularly phase-separated.

A variety of hetero bottlebrushes can be synthesized according to the above-mentioned strategies. For example, a mixed bottlebrush[26] can be prepared by the grafting-through method via random[27] and alternating,[28] the grafting-from method via multiple types of living polymerization with orthogonal mechanisms[29] or successive polymerization,[30] and the grafting-to method via coupling[31] or substrate-specific reactions with multifunctional polymers.[32] These methods have advantages and disadvantages similar to those of homo bottlebrushes. In addition, the combination of different methods can design a variety of chemical structures of the main and side chains. One of the most notable strategies to synthesize a Janus bottlebrush is the grafting-through method using, as a macromonomer, a block copolymer with a polymerizable group near the connecting point of the different blocks, because of the simplicity of synthesis and structural clearness of products.[33-35] In this strategy, ring-opening metathesis polymerization is widely used, because it is tolerant to steric hindrance of a bulky two-side macromonomer otherwise damaging the polymerizability.

A core-shell bottlebrush offers different function at the inner (core) and outer (shell) segment of side chain. For instance, the core-shell bottlebrush with degradable core and cross-linkable shell can be a nanotube or a nanocapsule.[36] In addition, a core-shell bottlebrush acts as a precursor[37] or a scaffold[38,39] for a wire-shape hybrid material. In this case, the shell avoids intermolecular aggregation and enhance solubility in solution. Block and Janus bottlebrushes have different symmetry planes, leading to fascinating properties in their higher-order structures.[40-42] For instance, when block bottlebrushes have sufficiently dense side chains to extend to the main chain, the main chain is arranged perpendicular to the interface between phase-separated domains. Therefore, as the domain size depends mainly on the degree of polymerization of the main chain, the block bottlebrush could form a microphase-separated structure with a large domain size,

which can be a photonic crystal. By contrast, for Janus bottlebrushes, the main chain is arranged parallel to the interface. The domain sizes are determined by the degree of polymerization of the side chains.[31] As the preorganized interface of the incompatible side chains stabilizes the microphase separation, the Janus bottlebrush could form a self-assembled structure with a much smaller domain size than a linear block copolymer with the same molecular weight. Generally, in comparison with a linier block copolymer, the block and Janus bottlebrush readily form high-order structures because their stiff main chain can more effectively suppress the intramolecular entanglement to accelerate the microphase separation. Other interesting properties of Janus bottlebrushes are self-assembling in solution,[43,44] nanocarriers of small-molecules,[45,46] and the stabilization of biphasic systems.[47,48]

1-4. Interaction Between Polymer and Liquid Crystal

A Liquid crystal (LC) is a state of matter that has properties of both solid crystals and liquids and may flow like a liquid even though its molecules are oriented like solid crystals.[49] The best-known states of LC are nematic, smectic, and cholesteric states. In the nematic state, the directors of molecules are oriented in one direction, although the relative position of molecules are not restricted. In the smectic state, molecules are arranged to form layers in the same direction and are able to freely move in the layer. In the cholesteric state, molecules are arranged to form layers, and their director in each layer varies with stacking layers. When the orientation of the bulk LC is deformed from the most stable state, the LC stores the elastic energy depending on the degree of splay, twist, and bend deformations. Additionally, the orientation can be controlled by external conditions, such as electric and magnetic fields and temperature. Therefore, the local orientation of the LC should be arranged in way to reduce the sum of their elastic energy and free energy derived from the external fields.

The orientation of LC can be controlled also by a low-molecular-weight additive, for example, chiral dopant,[50] gelator[51] and microemaulsion.[52] Similarly, the structure and properties of a LC state can be modified by the interaction between LC and polymers. For instance, the *in-situ* polymerization of monomers in the blue-phase LC widen the temperature window.[53] In general, the temperature window of the blue phase is very narrow because blue phase originally contains defects. In such a situation, the polymer is located in the disclination to stabilize the blue phase, giving a wider temperature window of the LC state. As mentioned above, the polymer network in LC can enhance the functionalities of LC devices.

1-4-1. LC Anchoring at the Interface

The motion of LC molecules on the surface is oriented to the easy axis by the interaction between the LC and the surface. In bulk, the vertical and horizontal orientation states against the surface are called homeotropic and homogenous orientations, respectively. It is important to control the easy axis for LC devices with a narrow cell gap because it affects the orientation of LC far from surface through elastic interaction of LC molecules. Additionally, the alignment of the particles dispersed in the LC can be controlled by the easy axis of the particle surface via the defect pattern around the particles.

When the director of the LC molecule on the surface deviates from the easy axis, the elastic energy is stored. This energy is called the anchoring energy. The anchoring energy f is divided into two components: zenial energy f_1 and azimuthal anchoring energy f_2. The zenithal and azimuthal anchoring strength (A_1 and A_2, respectively) are defined by the following equations:[54]

$$f_{\varphi} = \frac{1}{2} A_1 \sin^2(\varphi - \varphi_{\mathrm{p}})$$

$$f_\theta = \frac{1}{2} A_2 \sin^2(\theta - \theta_p)$$

where φ and θ, and φ_p and θ_p represent the zenial and azimuthal directions of the LC molecule and the easy axis against the surface, respectively, as shown in Figure 1-5. In the case of a strongly anchoring surface, when an external field is applied, the elastic energy is stored between the LC in bulk and on the surface because the orientation of the LC on the surface remains unchanged. This energy then acts as a driving force and helps in returning to the initial state of the LC device without external fields. In contrast, in the case of a weakly anchoring surface, the elastic energy is not stored because the orientation of the LC on the surface and the LC in the bulk is changed. Therefore, such a surface can be applied to LC devices with memory or energy saving performance because LC molecules can be rotated easily and keep the orientation.

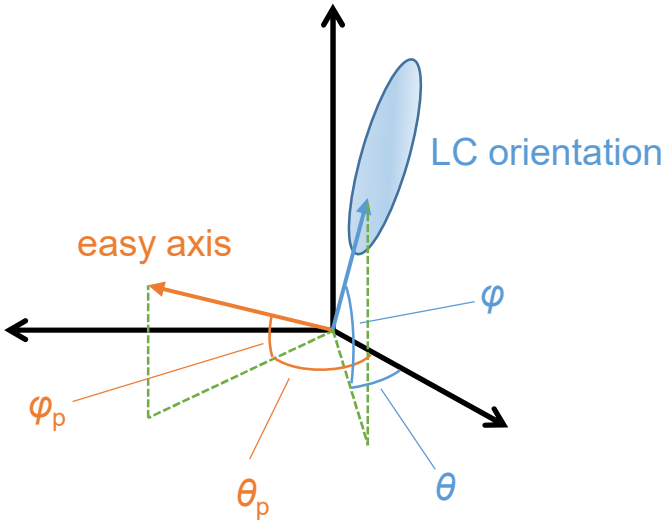

Figure 1-5. Schematic of easy axis and LC orientation.

1-5. Background and Purpose of this Thesis

1-5-1. Fundamentals of Bottlebrushes

Bottlebrushes consisting of flexible polymer segments as both side and main chains have been mainly studied in their conformation and dynamics related to e.g., the stiffness and entanglement of their main chain, in solution and bulk from the viewpoint of their molecular characteristics such as the degree of polymerization of the main and side chains, density and composition of side chains, and the affinity with solvent.[55-66] Additionally, as for Janus bottlebrushes, the effect of the composition and molecular weights of different kinds of side chains has been investigated as one of key factors determining their structure and properties. These studies provided extensive information about the design of bottlebrushes and helped in expanding the range of their applications. In those cases, the overlapping of side chains plays an important role in the main-chain conformation and bottlebrush dynamics. However, there are few studies focusing on the chemical property of the main chain of homo- as well as Janus bottlebrushes: most of the studies were targeted on bottlebrushes of flexible main chains easily and simply synthesized. Therefore, in the first part of this thesis, the author focuses on cellulose as the main chain of bottlebrushes because of its unique molecular characteristics.

Cellulose is one of the most abundant natural polymers consisting of anhydroglucose repeating units (AGUs)-linked via $\beta(1\rightarrow4)$ glycosidic bonds.[67] It has three types of hydroxyl groups in AGU. The main chain is stiffer than a typical vinyl polymer such as poly(methyl methacrylate)[68,69] and has chirality. Hence, some cellulose derivatives and cellulose nanocrystals form cholesteric liquid crystals. When cellulose is adopted as the main chain of Janus bottlebrush, its side chains are restricted in a helical pattern (Figure 1-6) to possibly form a helical higher-order structure. Therefore, the author aims to analyze the conformation of homo and Janus cellulosic bottlebrushes in dilute solution.

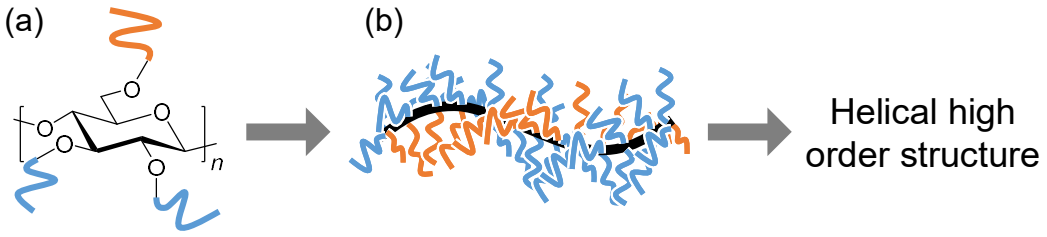

Figure 1-6. (a) First and (b) expected higher-order structures of cellulosic Janus bottlebrush.

1-5-2. Applications of Bottlebrushes

Bottlebrushes have been applied in various fields of science and technology because of their unique structure and properties. Among them, the author focuses on the application taking advantage of their novel properties as a surface modifier, especially by the analogy with the above-mentioned CPB effect. As shown in Figure 1-7, Sato and coworkers revealed that a CPB composed of poly (hexyl methacrylate) (PHMA) exhibits unique LC-anchoring properties in which the azimuthal anchoring strength is almost zero (zero azimuthal anchoring).[70] In contrast, a CPB composed of poly(methyl methacrylate) exhibits high azimuthal anchoring strength.[71] As for a CPB consisting of poly (ethyl methacrylate)[72] or polystyrene,[73] the anchoring strength depends on the temperature, that is, high and low azimuthal anchoring strength were observed at low and high temperatures, respectively. Additionally, they demonstrated that a bottlebrush film with PHMA showed zero-azimuthal anchoring properties and successfully applied this system to a LC-display device (Figure 1-8).[74] The precise surface modification to achieve not only zero anchoring but also zero-azimuthal anchoring will open up the potentials to improve the performance of the LC device. However, the mechanism of anchoring remains unclear in detail. Consequently, in the second part of this thesis, the author aims to reveal the detailed mechanism especially from the viewpoint of the structure and dynamics of bottlebrush systems.

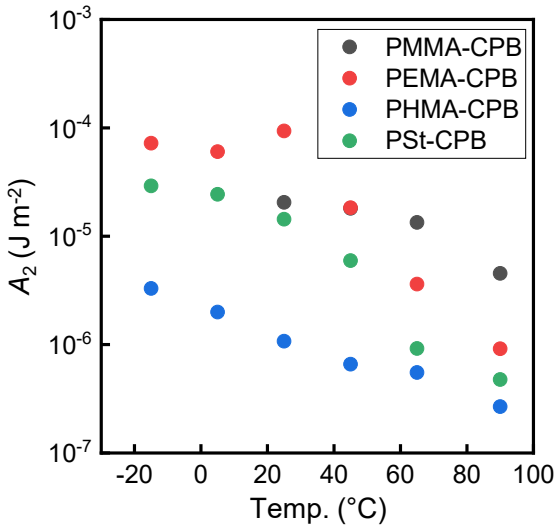

Figure 1-7. Dependency of azimuthal anchoring strength A_2 on temperature of CPB (Ref, 73):PMMA: poly(methyl methacrylate); PEMA: poly(ethyl methacrylate); PHMA: poly(hexyl methacrylate); PSt: polystyrene.

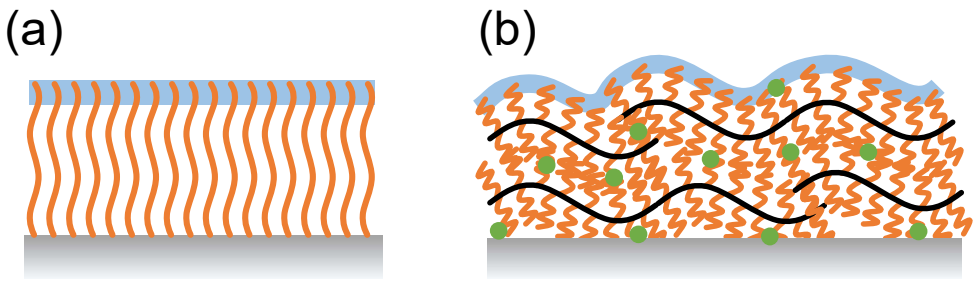

Figure 1-8. Schematic of (a) CPB and (b) crosslinked bottlebrush film.

1-6. Outline of this Thesis

The thesis is divided into two parts subsequently to the general introduction in **Chapter 1**. In **Part 1**, the synthesis of a variety of well-defined cellulosic bottlebrushes and their molecular/structural characterization including higher-order structure is described in **Chapters 2** to **5**. As **Part 2**, the interaction between bottlebrushes and LC molecules is discussed in **Chapter 6** and **7**.

In **Chapter 2**, the author attempts to establish a new synthetic route to cellulosic bottlebrushes which possess two kinds of side chains at 2,3-*O* and 6-*O* positions with high regioselectivity. The side chains, poly(ethylene oxide) (PEO) and polystyrene, are introduced because of their large Flory-Huggins interaction parameters (χ). To amplify chirality of the main chain, it is important to introduce different side chains to the main chain regioselectively and quantitatively to arrange them in a potentially helical pattern as a unique cellulosic-chain character. In addition, if the density of side chains is too low, they may not form a helix. Therefore, a cellulosic derivative with a 6-*O* hydroxyl group protected regioselectively is chosen as a starting material. The introduction of PEO and PSt is carried out using the grafting-to method via the esterification and click reactions. The side-chain density and regioselectivity are confirmed by NMR and gel permeation chromatography measurements. Based on a newly established methodology, other types of cellulosic bottlebrushes are also synthesized.

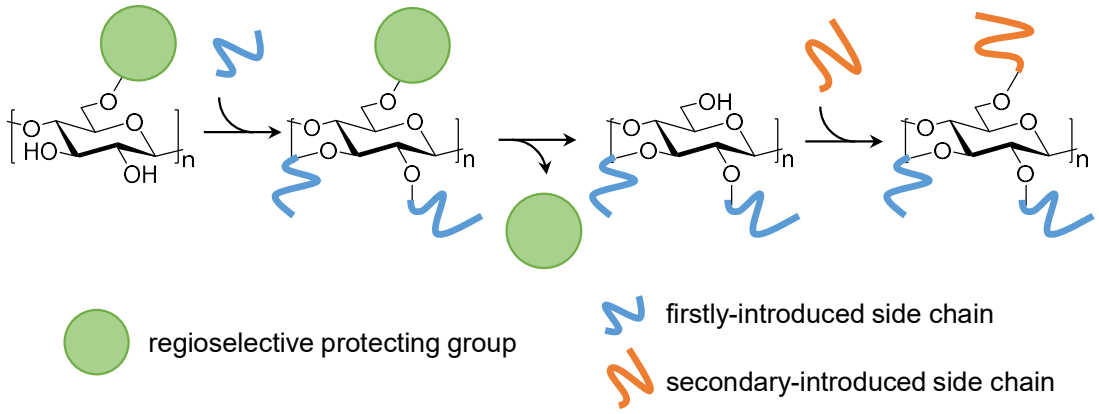

Figure 1-9. Schematic of synthetic route for Janus cellulosic bottlebrushes.

To date, comprehensive studies on the conformation of bottlebrushes have experimentally dedicated mainly to those with flexible main and side chains. In **Chapter 3**, the author focuses on the cellulosic bottlebrush with a PSt side chain in a poor solvent to reveal the

effect of the semiflexible main chain on the conformation of the whole bottlebrush. The side-chain conformation can be determined by a cross-sectional Guinier plot of data obtained by small-angle X-ray scattering (SAXS) measurement, and the main-chain conformation can be analyzed with a KP chain model using the relationship between S^2 and the degree of polymerization of the main chain obtained by a size exclusion chromatography-multi angle light scattering (SEC-MALS) measurement. The author discusses the conformation of side chains and stiffness of the main chains.

Janus bottlebrushes are building blocks for high-order structures owing to the microphase separation between immiscible side chains. However, their conformation in dilute solutions is not yet clear. In **Chapter 4**, the author analyzes the cross-sectional structure of a Janus cellulosic bottlebrush with PSt and PEO side chains as well as the semiflexible main chain. The author confirms that the cellulosic bottlebrush with PSt side chains maintains a cylindrical shape even in a poor solvent in Chapter 2. Thus, the Janus cellulosic bottlebrush is expected to form a microphase-separated structure with no intramolecular aggregation under poor solvent. The cross-sectional radius of gyration S_c of Janus cellulosic bottlebrush is determined by SAXS measurement. Then, the cross-sectional structure is estimated by comparing some models (Figure 1-10) for cross-sectional structure and the dependency of S_c on the molecular weight of the side chain. Finally, the author discusses whether or not the Janus cellulosic bottlebrush would induce intramolecular microphase separation to form e.g., fan-shaped domains.

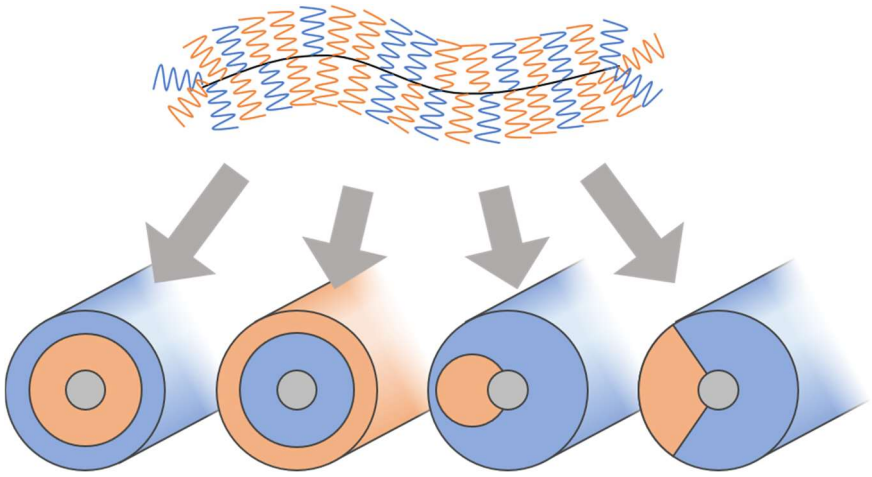

Figure 1-10. Cross-sectional models of phase-separated structures of Janus cellulosic bottlebrush in dilute solution.

In **Chapter 5**, the author newly targets, as a Janus bottlebrush, the cellulosic bottlebrush regioselectively possessing poly(ε-caprolactone) (PCL) at the 2,3-*O* position and PSt at the 6-*O* position to demonstrate that the Janus cellulosic bottlebrush could undergo microphase separation in bulk (Figure 1-11). The microphase-separated structures are observed by SAXS and a transmittance electron microscope. The results are discussed from the viewpoints of the side-chain restriction by the main chain and detailed intramolecular phase separation. The fundamental studies on the formation of higher-order structures can broaden the range of possible applications of Janus cellulosic bottlebrushes.

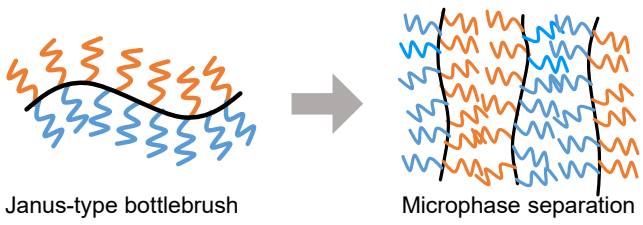

Figure 1-11. Schematic illustrations of Janus cellulosic bottlebrush with PCL and PSt side chains and its phase-separated structure in bulk.

In **Chapter 6**, the author aims to reveal the mechanism of a weak LC-anchoring on the

cross-linked bottlebrush films consisting of PHMA. For this purpose, the author investigates the temperature dependency of the azimuthal anchoring strength of the crosslinked bottlebrush films by measuring the voltage-transmittance curve at each temperature. In addition to measuring the swelling ratio of crosslinked bottlebrush films, rheological and optical measurements are carried out for a mixture of the bottlebrush and the LC instead of crosslinked bottlebrush swollen in LC. The same experiment with PEMA is carried out as a reference for PHMA. By combining the obtained results, the author discusses how the weak anchoring properties are related to the dynamics of the bottlebrush as well as the reduction of interaction. This information would be useful to design next-generation LC devices.

A LC molecule on the bottlebrush film is expected to give a time-dependent response with multiple modes, when an external field is applied. In **Chapter 7**, the author monitors the time course of transmittance in the in-plane LC cell with the PHMA bottlebrush film against the stepwise electric field applied and analyzes the obtained data with a relaxation function. The same experiment with PMMA bottlebrush is carried out as a reference for PHMA. The relaxation mode of interaction of LC and bottlebrush film is discussed.

1-7. Reference

1. Benoit, H.; Doty, P. Light Scattering from Non-Gaussian Chains. *J. Phys. Chem.* **1953**, *57*, 958-963.
2. Snijkers, F.; Ratkanthwar, K.; Vlassopoulos, D.; Hadjichristidis, N. Viscoelasticity, Nonlinear Shear Start-up, and Relaxation of Entangled Star Polymers. *Macromolecules* **2013**, *46*, 5702-5713.
3. Uppuluri, S.; Morrison, F. A.; Dvornic, P. R. Rheology of Dendrimers. 2. Bulk Polyamidoamine Dendrimers under Steady Shear, Creep, and Dynamic Oscillatory Shear. *Macromolecules* **2000**, *33*, 2551-2560.
4. Doi, Y.; Matsubara, K.; Ohta, Y.; Nakano, T.; Kawaguchi, D.; Takahashi, Y.; Takano,

A.; Matsushita, Y. Melt Rheology of Ring Polystyrenes with Ultrahigh Purity. *Macromolecules* **2015**, *48*, 3140-3147.

5. Tsujii, Y.; Ohno, K.; Yamamoto, S.; Goto, A.; Fukuda, T. Structure and Properties of High-Density Polymer Brushes Prepared by Surface-Initiated Living Radical Polymerization. In *Surface-Initiated Polymerization I*, Jordan, R., Ed. Springer: Berlin, Heidelberg, 2006; pp 1-45.
6. Goto, A.; Tsujii, Y. Surface-Initiated Living Radical Polymerizations Using Iodine, Organotellurium, and Organic Catalysts. In *Controlled Radical Polymerization at and from Solid Surfaces*, Vana, P., Ed. 2015; pp 107-122.
7. Beers, K. L.; Gaynor, S. G.; Matyjaszewski, K.; Sheiko, S. S.; Möller, M. The Synthesis of Densely Grafted Copolymers by Atom Transfer Radical Polymerization. *Macromolecules* **1998**, *31*, 9413-9415.
8. Zhang, Y.; Shen, Z.; Yang, D.; Feng, C.; Hu, J.; Lu, G.; Huang, X. Convenient Synthesis of P*t*BA-*g*-PMA Well-Defined Graft Copolymer with Tunable Grafting Density. *Macromolecules* **2010**, *43*, 117-125.
9. Schappacher, M.; Deffieux, A. New Comblike Copolymers of Controlled Structure and Dimensions Obtained by Grafting by Polystyryllithium onto Poly(chloroethyl vinyl ether) Chains. *Macromol. Chem. Phys.* **1997**, *198*, 3953-3961.
10. Tsukahara, Y.; Mizuno, K.; Segawa, A.; Yamashita, Y. Study on the Radical Polymerization Behavior of Macromonomers. *Macromolecules* **1989**, *22*, 1546-1552.
11. Gao, H.; Matyjaszewski, K. Synthesis of Molecular Brushes by "Grafting onto" Method: Combination of ATRP and Click Reactions. *J. Am. Chem. Soc.* **2007**, *129*, 6633-6639.
12. Engler, A. C.; Lee, H. I.; Hammond, P. T. Highly Efficient "Grafting Onto" a Polypeptide Backbone Using Click Chemistry. *Angew. Chem., Int. Ed.* **2009**, *48*, 9334-9338.
13. Gadwal, I.; Rao, J.; Baettig, J.; Khan, A. Functionalized Molecular Bottlebrushes. *Macromolecules* **2013**, *47*, 35-40.
14. Yamada, K.; Miyazaki, M.; Ohno, K.; Fukuda, T.; Minoda, M. Atom Transfer Radical Polymerization of Poly(vinyl ether) Macromonomers. *Macromolecules* **1999**, *32*, 290-293.
15. Varlas, S.; Lawrenson, S. B.; Arkinstall, L. A.; O'Reilly, R. K.; Foster, J. C. Self-Assembled Nanostructures from Amphiphilic Block Copolymers Prepared via Ring-Opening Metathesis Polymerization (ROMP). *Prog. Polym. Sci.* **2020**, *107*, 101278.
16. Vosloo, J. J.; Tonge, M. P.; Fellows, C. M.; D'Agosto, F.; Sanderson, R. D.; Gilbert, R. G. Synthesis of Comblike Poly(butyl methacrylate) Using Reversible

Addition−Fragmentation Chain Transfer and an Activated Ester. *Macromolecules* **2004**, *37*, 2371-2382.

17. Matyjaszewski, K. Atom Transfer Radical Polymerization (ATRP): Current Status and Future Perspectives. *Macromolecules* **2012**, *45*, 4015-4039.
18. Moad, G.; Rizzardo, E.; Thang, S. H. Living Radical Polymerization by the RAFT Process – A Third Update. *Aust. J. Chem.* **2012**, *65*, 985.
19. Daniel, W. F.; Burdynska, J.; Vatankhah-Varnoosfaderani, M.; Matyjaszewski, K.; Paturej, J.; Rubinstein, M.; Dobrynin, A. V.; Sheiko, S. S. Solvent-Free, Supersoft and Superelastic Bottlebrush Melts and Networks. *Nat. Mater.* **2016**, *15*, 183-189.
20. Liu, X. Surface Forces between Bottlebrush Polymer Layers. *Curr. Opin. Colloid Interface Sci.* **2020**, *47*, 16-26.
21. Hardingham, T.; Fosang, A. Proteoglycans: Many Forms and Many Functions. *FASEB J.* **1992**, *6*, 861-870.
22. Buckwalter, J.; Rosenberg, L. Electron Microscopic Studies of Cartilage Proteoglycans. Direct Evidence for the Variable Length of the Chondroitin Sulfate-rich Region of Proteoglycan Subunit Core Protein. *J. Biol. Chem.* **1982**, *257*, 9830-9839.
23. Seog, J.; Dean, D.; Plaas, A. H. K.; Wong-Palms, S.; Grodzinsky, A. J.; Ortiz, C. Direct Measurement of Glycosaminoglycan Intermolecular Interactions via High-Resolution Force Spectroscopy. *Macromolecules* **2002**, *35*, 5601-5615.
24. Xie, G.; Martinez, M. R.; Olszewski, M.; Sheiko, S. S.; Matyjaszewski, K. Molecular Bottlebrushes as Novel Materials. *Biomacromolecules* **2019**, *20*, 27-54.
25. Chen, K.; Hu, X.; Zhu, N.; Guo, K. Design, Synthesis, and Self-Assembly of Janus Bottlebrush Polymers. *Macromol. Rapid Commun.* **2020**, *41*, 2000357.
26. Le, A. N.; Liang, R.; Zhong, M. Synthesis and Self-Assembly of Mixed-Graft Block Copolymers. *Chemistry* **2019**, *25*, 8177-8189.
27. Stephan, T.; Muth, S.; Schmidt, M. Shape Changes of Statistical Copolymacromonomers: From Wormlike Cylinders to Horseshoe- and Meanderlike Structures. *Macromolecules* **2002**, *35*, 9857-9860.
28. Ishizu, K.; Shen, X. X.; Tsubaki, K. I. Radical Copolymerization Reactivity of Methacryloyl-Terminated Poly(ethylene glycol methylether) with Vinylbenzyl-Terminated Polystyrene Macromonomers. *Polymer* **2000**, *41*, 2053-2057.
29. Shi, G. Y.; Zou, P.; Pan, C. Y. Synthesis and Characterization of Asymmetric Centipede-like Copolymers with Two Side Chains at Each Repeating Unit via ATRP and Ring-Opening Polymerization. *J. Polym. Sci., Part A: Polym. Chem.* **2008**, *46*, 5580-5591.

30. Bolton, J.; Rzayev, J. Tandem RAFT-ATRP Synthesis of Polystyrene–Poly(Methyl Methacrylate) Bottlebrush Block Copolymers and Their Self-Assembly into Cylindrical Nanostructures. *ACS Macro Lett.* **2011**, *1*, 15-18.
31. Hou, C.; Hu, J.; Liu, G.; Wang, J.; Liu, F.; Hu, H.; Zhang, G.; Zou, H.; Tu, Y.; Liao, B. Synthesis and Bulk Self-Assembly of Well-Defined Binary Graft Copolymers. *Macromolecules* **2013**, *46*, 4053-4063.
32. Cakir, N.; Yavuzarslan, M.; Durmaz, H.; Hizal, G.; Tunca, U. Heterograft Brush Cpolymers via Romp and Triple Click Reaction Strategies Involving CuAAC, Diels-Alder, and Nitroxide Radical Coupling Reactions. *J. Polym. Sci., Part A: Polym. Chem.* **2013**, *51*, 899-907.
33. Li, Y.; Themistou, E.; Zou, J.; Das, B. P.; Tsianou, M.; Cheng, C. Facile Synthesis and Visualization of Janus Double-Brush Copolymers. *ACS Macro Lett.* **2011**, *1*, 52-56.
34. Xu, B.; Feng, C.; Huang, X. A Versatile Platform for Precise Synthesis of Asymmetric Molecular Brush in One Shot. *Nat. Commun.* **2017**, *8*, 333.
35. Nguyen, H. V.; Gallagher, N. M.; Vohidov, F.; Jiang, Y.; Kawamoto, K.; Zhang, H.; Park, J. V.; Huang, Z.; Ottaviani, M. F.; Rajca, A.; Johnson, J. A. Scalable Synthesis of Multivalent Macromonomers for ROMP. *ACS Macro Lett.* **2018**, *7*, 472-476.
36. Huang, K.; Jacobs, A.; Rzayev, J. De Novo Synthesis and Cellular Uptake of Organic Nanocapsules with Tunable Surface Chemistry. *Biomacromolecules* **2011**, *12*, 2327-34.
37. Yuan, J.; Xu, Y.; Walther, A.; Bolisetty, S.; Schumacher, M.; Schmalz, H.; Ballauff, M.; Muller, A. H. Water-Soluble Organo-Silica Hybrid Nanowires. *Nat. Mater.* **2008**, *7*, 718-22.
38. Djalali, R.; Li, S.-Y.; Schmidt, M. Amphipolar Core−Shell Cylindrical Brushes as Templates for the Formation of Gold Clusters and Nanowires. *Macromolecules* **2002**, *35*, 4282-4288.
39. Pang, X.; He, Y.; Jung, J.; Lin, Z. 1D Nanocrystals with Precisely Controlled Dimensions, Compositions, and Architectures. *Science* **2016**, *353*, 1268-1272.
40. Sveinbjornsson, B. R.; Weitekamp, R. A.; Miyake, G. M.; Xia, Y.; Atwater, H. A.; Grubbs, R. H. Rapid Self-Assembly of Brush Block Copolymers to Photonic Crystals. *Proc. Natl. Acad. Sci. U. S. A.* **2012**, *109*, 14332-14336.
41. Miyake, G. M.; Weitekamp, R. A.; Piunova, V. A.; Grubbs, R. H. Synthesis of Isocyanate-Based Brush Block Copolymers and Their Rapid Self-Assembly to Infrared-Reflecting Photonic Crystals. *J. Am. Chem. Soc.* **2012**, *134*, 14249-14254.
42. Cheng, L. C.; Gadelrab, K. R.; Kawamoto, K.; Yager, K. G.; Johnson, J. A.;

Alexander-Katz, A.; Ross, C. A. Templated Self-Assembly of a PS- Branch-PDMS Bottlebrush Copolymer. *Nano Lett.* **2018**, *18*, 4360-4369.

43. Fenyves, R.; Schmutz, M.; Horner, I. J.; Bright, F. V.; Rzayev, J. Aqueous Self-Assembly of Giant Bottlebrush Block Copolymer Surfactants as Shape-Tunable Building Blocks. *J. Am. Chem. Soc.* **2014**, *136*, 7762-7770.
44. Palacios-Hernandez, T.; Luo, H.; Garcia, E. A.; Pacheco, L. A.; Herrera-Alonso, M. Nanoparticles from Amphiphilic Heterografted Macromolecular Brushes with Short Backbones. *Macromolecules* **2018**, *51*, 2831-2837.
45. Tran, T. H.; Nguyen, C. T.; Gonzalez-Fajardo, L.; Hargrove, D.; Song, D.; Deshmukh, P.; Mahajan, L.; Ndaya, D.; Lai, L.; Kasi, R. M.; Lu, X. Long Circulating Self-Assembled Nanoparticles from Cholesterol-Containing Brush-Like Block Copolymers for Improved Drug Delivery to Tumors. *Biomacromolecules* **2014**, *15*, 4363-4375.
46. Luo, H.; Szymusiak, M.; Garcia, E. A.; Lock, L. L.; Cui, H.; Liu, Y.; Herrera-Alonso, M. Solute-Triggered Morphological Transitions of an Amphiphilic Heterografted Brush Copolymer as a Single-Molecule Drug Carrier. *Macromolecules* **2017**, *50*, 2201-2206.
47. Li, Y.; Zou, J.; Das, B. P.; Tsianou, M.; Cheng, C. Well-Defined Amphiphilic Double-Brush Copolymers and Their Performance as Emulsion Surfactants. *Macromolecules* **2012**, *45*, 4623-4629.
48. Xie, G.; Krys, P.; Tilton, R. D.; Matyjaszewski, K. Heterografted Molecular Brushes as Stabilizers for Water-in-Oil Emulsions. *Macromolecules* **2017**, *50*, 2942-2950.
49. Andrienko, D. Introduction to Liquid Crystals. *J. Mol. Liq.* **2018**, *267*, 520-541.
50. Eelkema, R.; Feringa, B. L. Amplification of Chirality in Liquid Crystals. *Org. Biomol. Chem.* **2006**, *4*, 3729-45.
51. Abdallah, D. J.; Weiss, R. G. Organogels and Low Molecular Mass Organic Gelators. *Adv. Mater.* **2000**, *12*, 1237-1247.
52. Yamamoto, J.; Tanaka, H. Transparent Nematic Phase in a Liquid-Crystal-Based Microemulsion. *Nature* **2001**, *409*, 321-5.
53. Kikuchi, H.; Yokota, M.; Hisakado, Y.; Yang, H.; Kajiyama, T. Polymer-Stabilized Liquid Crystal Blue Phases. *Nat. Mater.* **2002**, *1*, 64-8.
54. Vilfan, M.; Copic, M. Azimuthal and Zenithal Anchoring of Nematic Liquid Crystals. *Phys. Rev. E: Stat., Nonlinear, Soft Matter Phys.* **2003**, *68*, 031704.
55. Nakamura, Y.; Norisuye, T. Backbone Stiffness of Comb-Branched Polymers. *Polym. J.* **2001**, *33*, 874-878.
56. Terao, K.; Takeo, Y.; Tazaki, M.; Nakamura, Y.; Norisuye, T. Polymacromonomer

Consisting of Polystyrene. Light Scattering Characterization in Cyclohexane. *Polym. J.* **1999**, *31*, 193-198.

57. Terao, K.; Nakamura, Y.; Norisuye, T. Solution Properties of Polymacromonomers Consisting of Polystyrene. 2. Chain Dimensions and Stiffness in Cyclohexane and Toluene. *Macromolecules* **1999**, *32*, 711-716.
58. Terao, K.; Hokajo, T.; Nakamura, Y.; Norisuye, T. Solution Properties of Polymacromonomers Consisting of Polystyrene. 3. Viscosity Behavior in Cyclohexane and Toluene. *Macromolecules* **1999**, *32*, 3690-3694.
59. Hokajo, T.; Terao, K.; Nakamura, Y.; Norisuye, T. Solution Properties of Polymacromonomers Consisting of Polystyrene V. Effect of Side Chain Length on Chain Stiffness. *Polym. J.* **2001**, *33*, 481-485.
60. Sugiyama, M.; Nakamura, Y.; Norisuye, T. Dilute-Solution Properties of Polystyrene Polymacromonomer Having Side Chains of over 100 Monomeric Units. *Polym. J.* **2007**, *40*, 109-115.
61. Hatanaka, Y.; Nakamura, Y. Dilute Solution Properties of Polymacromonomer Consisting of Polybutadiene Backbone and Polystyrene Side Chains. *Polymer* **2013**, *54*, 1538-1542.
62. Kikuchi, M.; Lien, L. T. N.; Narumi, A.; Jinbo, Y.; Izumi, Y.; Nagai, K.; Kawaguchi, S. Conformational Properties of Cylindrical Rod Brushes Consisting of a Polystyrene Main Chain and Poly(*n*-hexyl isocyanate) Side Chains. *Macromolecules* **2008**, *41*, 6564-6572.
63. Kikuchi, M.; Nakano, R.; Jinbo, Y.; Saito, Y.; Ohno, S.; Togashi, D.; Enomoto, K.; Narumi, A.; Haba, O.; Kawaguchi, S. Graft Density Dependence of Main Chain Stiffness in Molecular Rod Brushes. *Macromolecules* **2015**, *48*, 5878-5886.
64. Zhang, B.; Gröhn, F.; Pedersen, J. S.; Fischer, K.; Schmidt, M. Conformation of Cylindrical Brushes in Solution: Effect of Side Chain Length. *Macromolecules* **2006**, *39*, 8440-8450.
65. Subbotin, A.; Saariaho, M.; Ikkala, O.; ten Brinke, G. Elasticity of Comb Copolymer Cylindrical Brushes. *Macromolecules* **2000**, *33*, 3447-3452.
66. Wintermantel, M.; Gerle, M.; Fischer, K.; Schmidt, M.; Wataoka, I.; Urakawa, H.; Kajiwara, K.; Tsukahara, Y. Molecular Bottlebrushes. *Macromolecules* **1996**, *29*, 978-983.
67. Klemm, D.; Heublein, B.; Fink, H. P.; Bohn, A. Cellulose: Fascinating Biopolymer and Sustainable Raw Material. *Angew. Chem., Int. Ed. Engl.* **2005**, *44*, 3358-3393.
68. Jiang, X.; Kitamura, S.; Sato, T.; Terao, K. Chain Dimensions and Stiffness of Cellulosic and Amylosic Chains in an Ionic Liquid: Cellulose, Amylose, and an

Amylose Carbamate in BmimCl. *Macromolecules* **2017**, *50*, 3979-3984.
69. Tamai, Y.; Konishi, T.; Einaga, Y.; Fujii, M.; Yamakawa, H. Mean-Square Radius of Gyration of Oligo- and Poly(methyl methacrylate)s in Dilute Solutions. *Macromolecules* **1990**, *23*, 4067-4075.
70. Sato, O.; Kasai, T.; Sato, M.; Sakajiri, K.; Tsujii, Y.; Kang, S.; Watanabe, J.; Tokita, M. High-Density Poly(hexyl methacrylate) Brushes Offering a Surface for Near-Zero Azimuthal Anchoring of Liquid Crystals at Room Temperature. *J. Mater. Chem. C* **2013**, *1*, 7992-7995.
71. Tokita, M.; Sato, O.; Inagaki, Y.; Nomura, A.; Tsujii, Y.; Kang, S.; Fukuda, T.; Watanabe, J. High-Density Poly(methyl methacrylate) Brushes as Anchoring Surfaces of Nematic Liquid Crystals. *Jpn. J. Appl. Phys.* **2011**, *50*, 071701.
72. Sato, O.; Iwata, N.; Kasai, T.; Tsujii, Y.; Kang, S. M.; Watanabe, J.; Tokita, M. Nematic Liquid Crystal Anchoring Strengths of High Density Polymer Brush Surfaces. *Liq. Cryst.* **2015**, *42*, 181-188.
73. Sato, O.; Kasai, T.; Nomura, A.; Tsujii, Y.; Kang, S.; Tokita, M.; Watanabe, J. Viscoelastic PS Brush Surface Offering Strong Anchoring at Low Temperature and Near-Zero Anchoring at High Temperature for LC Molecules. *Liq. Cryst.* **2012**, *40*, 221-227.
74. Sato, O.; Okuno, H.; Adachi, I.; Watanabe, J.; Tokita, M.; Sakakibara, K.; Kinose, Y.; Goto, A.; Tsujii, Y. Novel In-Plane Switching Liquid Crystal Display with an Extremely High Transmittance Using a Well-Designed Bottlebrush as a Zero-Azimuth Anchoring Material. *Jpn. J. Appl. Phys.* **2019**, *58*, 066503.

Chapter 2

Regioselective Synthesis of Cellulosic Bottlebrushes with High Density of Side Chains

2-1. Introduction

Bottlebrushes have been studied because of its have many fascinating properties derived from densely attached side chain. Among them, Janus bottlebrush, which is the bottlebrush with immiscible two (or more) kinds of side chains uniformly along the main chain, has attracted much attention as a building block of higher order structure and a stabilizer of stabilizers of biphasic systems. However, up to now, the backbone of Janus bottlebrush is limited mainly to flexible chain, such as poly(methyl methacrylate) (PMMA), polystyrene (PSt) and polynorbornene.

Cellulose is known as one of most abundant natural polymers and has anhydroglucose units (AGUs) jointed by β-(1,4)-glycosidic bonds. Cellulose is categorized as a semi-flexible polymer, being stiffer than common vinyl polymers such as PMMA and PSt. More intriguingly, cellulose possesses a chiral center in its repeating unit, possibly inducing a helical conformation. For instance, its helical second-order structures are analyzed using crystallographic experiments[1] or molecular dynamics simulations.[2] Additionally, some cellulose derivatives are used as one of most attractive and effective chiral stationary phases for chiral column chromatography.[3] This is attributed to the side chains helically arranged by the chiral main chain. Such an inherent conformation could lead to the formation of helical higher-order structures. Some cellulose derivatives such as hydroxypropylcellulose (HPC) is known to form a cholesteric liquid crystal in a concentrated aqueous solution.[4-6] In addition, Cowie and coworkers reported that a cellulose derivative, 6-*O*-trityl-2,3-di-*O*-PEO cellulose regioselectively substituted with poly(ethylene

oxide) (PEO, *MW* = 350 g/mol) side chains also displayed a cholesteric liquid crystalline texture in bulk at room temperature, indicating that the higher order structure was dominated by the chiral main chain even though its volume fraction was small.[7]

The author focused on a Janus cellulosic bottlebrush, which has cellulose as the main chain and two kinds of polymers as side chains. When incompatible side chains are sufficiently densely and highly regioselectively substituted along the cellulosic main chain, their intramolecular microphase separation is expected to enhance the potential helicity of the cellulose chain: two helical or chiral domains can be formed around the main chain, resulting in helical or chiral higher-order structures. Even though some cellulosic bottlebrushes have been already synthesized,[8-11] a more sophisticated methodology is required to introduce two kinds of side chains with controlled regioselectivity and density.

In this chapter, the author set a goal to establish a synthetic route for a well-defined cellulosic Janus bottlebrush with two kinds of imcompatible side chains densely and regioselectively introduced. In order to ensure the regioselectivity of side chains, the author used MeOTr-cellulose as a staring material.[12] MeOTr is a regioselective protecting group for the 6-*O* hydroxyl group and enables to synthesize not only a homo cellulosic bottlebrush with a kind of side chains at 2,3-*O* positions (2A3A-cellulose) and a hetero (Janus) bottlebrush with different kinds of side chains at 2,3-*O* and 6-*O* positons (2A3A6B-cellulose).

Two method can be adopted to introduce side chains to cellulose chain: one is grafting-to method and the other is grafting-from method. The former has an advantage in characterizing the side chain before introduction. On the other hand, in the latter method, introduction of dense side chain is achieved, and the degree of polymerization is adjusted flexibly. In this chapter, the author demonstrated two synthetic routs, sequentially repeated (two-step) grafting-to reactions

and the combination of grafting-from polymerization and grafting-to reaction, to regioselectively introduce different kinds of side chain.

In the two-step grafting-to method, the author selected PEO and PSt as side chains because of their big difference in Flory-Huggins interaction parameter (χ).[13] Sequential introduction of the two polymers was attempted via the Williamson ether reaction for the PEO chain at 2,3-*O* positions[7] and the copper-catalyzed alkyne-azide cycloaddition (CuAAC) click reactions[14,15] for the PSt chain at 6-*O* position. The degree of substitution of the side chains was confirmed with nuclear magnetic resonance (NMR) and size exclusion chromatography (SEC) measurements.

Another Janus cellulosic bottlebrush of poly(ε-caprolactone) (PCL) at 2,3-*O* positions and PSt at 6-*O* position was synthesized by the combination of different synthetic strategies: ε-caprolactone (CL) was first polymerized from the hydroxyl groups of MeOTr-cellulose (via the grafting-from method) followed by introduction of PSt via CuAAC click reaction (via the grafting-to method). This Janus bottlebrush is expected to be a good model compound for microphase separation since there are many reports about the microphase separation of block copolymer consisting of PCL and PSt as well as PEO and PSt.

Based on similar methodology, a homo bottlebrush, 6A-cellulose, was also synthesized. 2A3A-cellulose and 6A-cellulose will be used to clarify the molecular characteristics of cellulosic chain to design cellulosic bottlebrushes of Januss as well as homos in the following chapters.

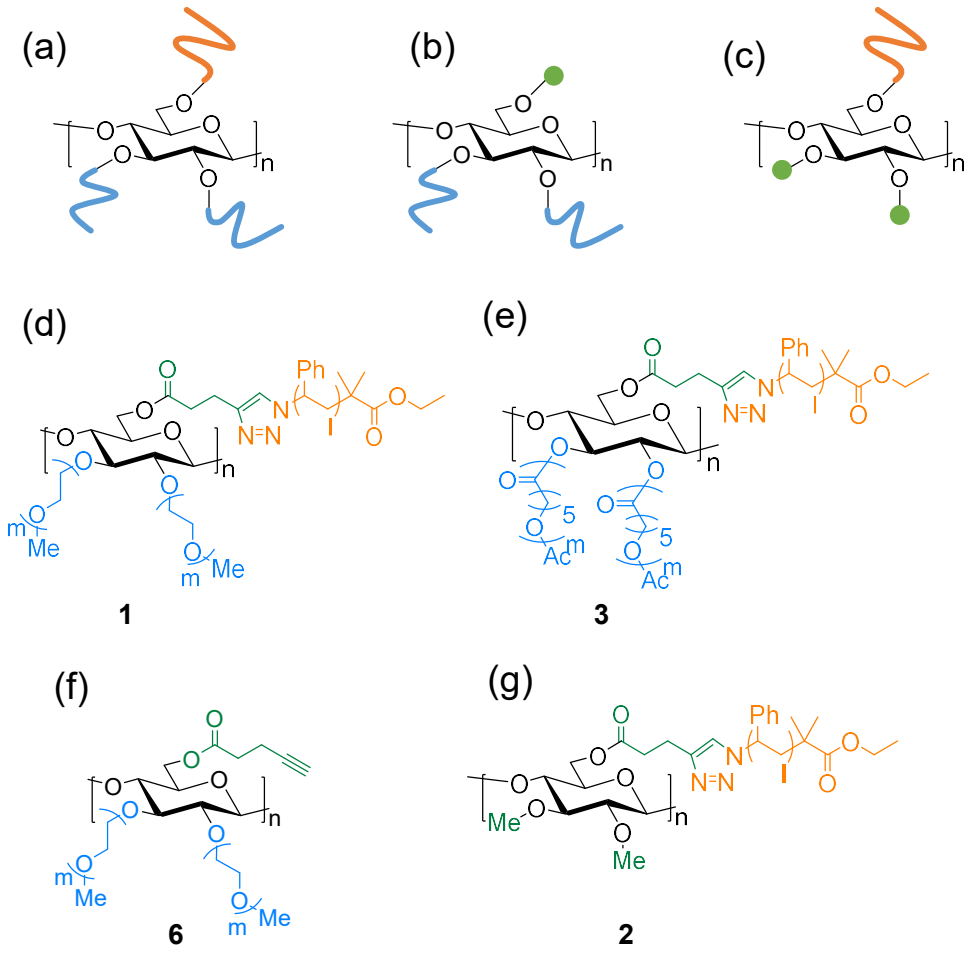

Figure 2-1. Schematic structures of 2A3A6B-cellulose (a), 2A3A-cellulose and 6A-cellulose (c), and chemical structures of the corresponding derivatives PEO-PSt-cellulose, **1** (d) and PCL-PSt-cellulose, (e), PEO-cellulose, **2** (f) and PSt-cellulose **6** (g).

2--2. Experimental Section

2-2-1. Materials

All reactions involving non-aqueous conditions were conducted in oven-dried glassware under Ar atmosphere. The starting material, 6-*O*-*p*-methoxytritylcellulose (MeOTr-cellulose, **6**) was synthesized from microcrystalline cellulose (MCC) (1.02331.0500, Merck, Germany) according to Gömez and coworkers.[12] The degree of substitution (*DS*) of *p*-methoxytrityl

(MeOTr) group was estimated to be 1.06 from the elemental analysis. The starting material, 2,3-di-*O*-methylcellulose (**4**), was synthesized from **6** according to the reported procedure.[10] The *DS* of the methyl groups (DS_{Me}) was estimated to be 1.8 from the ^{1}H NMR spectrum after derivatization with propionate. Methoxy poly(ethylene oxide) iodide (PEO-I) (MW = 860, DP_n = 16) was synthesized from monomethoxy poly(ethylene oxide) (MeO-PEO) (MW = 750, Sigma-Aldrich, US) according to Yue and coworkers. Azido-terminated PSt (PSt-N_3) was synthesized through atom transfer radical polymerization (ATRP) and substitution reaction according to Matyjaszewski and coworkers.[16] The number-average molecular weight (M_n) and polydispersity index (M_w/M_n) of PSt-N_3 were 6.4×10^3 and 1.1, 3.3×10^3 and 1.1, 2.2×10^3 and 1.1, 4.0×10^3 and 1.1, 9.2×10^3 and 1.1 and 1.6×10^4 and 1.1 for the synthesis of **1a** and **2a**, **1b** and **2b**, **1c** and **2c**, **3a**, **3b**, and **3c** respectively. The percentage of azidation of PSt-N_3 was estimated to be over 90 % from their ^{1}H-NMR spectrum. Commercial chemicals were of the highest grade available and were used without further purification if not stated otherwise.

2-2-2. Synthesis of Bottlebrushes

2-2-2-1. PSt-bottlebrush

*2,3-di-O-Methyl-6-O-pentynoylcellulose (**5**)*. 1-Ethyl-3-(3-dimethylaminopropyl)carbodiimide hydrochloride (EDC•HCl) (1.01 g, 5.28 mmol), 4-pentynoic acid (0.388 g, 3.95 mmol), and 4-dimethylaminopyridine (DMAP) (0.642 g, 5.26 mmol) were added into a solution of **7** (0.500 g, 2.63 mmol per AGU) in anhydrous DMF (20 mL). After stirring for 2.5 h at 80 °C, the mixture was stirred for 1 d at room temperature, and then stirred at 60 °C for 1 d. The reaction mixture was filtered and poured into a mixture of methanol (MeOH) and distilled water (1:1, v/v). The precipitate was collected by centrifugation, washed with MeOH, and dried under vacuum at 80 °C. The crude product was dissolved in THF (10 mL) and poured into a mixture of MeOH and

distilled water (1:1, v/v). The precipitate was collected by filtration, washed with a mixture of MeOH and distilled water (1:1 v/v), and dried under vacuum at 80 °C for 1 d to yield **5** (0.352 g, 48 %). SEC: M_w = 6.2 × 10^4 g mol^{-1}, M_w/M_n = 1.3. ^{1}H NMR (800 MHz, 27 °C, $C_2D_2Cl_4$): 2.07 (–C≡CH), 2.52 (–C*H*$_2$–CH$_2$–C≡CH), 2.58 (–C*H*$_2$–C≡CH), 2.96 (H2), 3.25 (H3), 3.3–4.0 (OMe, H4, H5), 4.28 (H6), 4.32 (H1), 4.55 (H6′). ^{13}C NMR (800 MHz, 27 °C, $C_2D_2Cl_4$): 14.2 (–*C*H$_2$–C≡CH), 33.1 (–*C*H$_2$–CH$_2$–C≡CH), 60.2 (3-*O*-Me), 60.6 (2-*O*-Me), 63.0 (C6), 69.5 (–C≡*C*H), 72.5 (C5), 78.1 (C4), 82.8 (–*C*≡CH), 83.3 (C2), 84.6 (C3), 102.8 (C1), 171.3 (C=O). $DS_{pentynoyl}$ (*DS* of the pentynoyl groups) = 1.2 (calculated from ^{1}H-NMR).

*6-O-PSt$_{60}$-2,3-di-O-methylcellulose (**1a**)*. **5** (9.7 mg, 0.034 mmol per AGU) was dissolved in DMF (4.7 mL), and PSt-N$_3$ (M_n = 6.4×10^3 g mol^{-1}, *DP* = 60; 365 mg, 0.0568 mmol) and ascorbic acid (62.7 mg, 0.356 mmol) were added into the solution. After adding copper(II) sulfate pentahydrate ($CuSO_4$•$5H_2O$) (8.9 mg, 0.036 mmol) under Ar, the reaction was stirred at 60 °C for 2 d. The reaction mixture was passed through an alumina column and dried under vacuum to yield a crude product. It was dissolved in CH_2Cl_2 (1 mL) and poured into a mixture of hexane and cyclohexane (6:1, v/v), and the precipitate was collected by centrifugation. This procedure was repeated twice, and the final product was dried under vacuum at 60 °C to yield **2a** (234 mg, 95 %). SEC-MALS: M_w = 8.1 × 10^5 g mol^{-1}, M_w/M_n = 1.6. ^{1}H NMR (600 MHz, $CDCl_3$): 0.8–1.1 (–CH$_2$–C*H*$_3$, –C–(CH$_3$)$_2$), 1.2–2.5 (–C*H*$_2$–C*H*Ph–), 2.5–5.5 (ring H, –C*H*$_2$–CH$_3$, –O-Me, –N–C*H*(Ph)–CH$_2$–), 6.2–7.5 (arom-H, N–CH=C).

*6-O-PSt$_{30}$-2,3-di-O-methylcellulose (**1b**)*. **5** (21.0 mg, 0.0744 mmol per AGU) was dissolved in DMF (9.4 mL), and PSt-N$_3$ (M_n = 3.3×10^3 g mol^{-1}, *DP* = 30; 381 mg, 0.117 mmol), ascorbic acid (125 mg, 0.708 mmol), and $CuSO_4$•$5H_2O$ (1.8 mg, 0.0070 mmol) were added. The reaction and

purification conditions were the same as those of **2a**. Yield: 172 mg (60 %). SEC-MALS: M_w = 4.6 × 10^5 g mol^{-1}, M_w/M_n = 1.7.

*6-O-PSt$_{20}$-2,3-di-O-methylcellulose (**1c**)*. **5** (27.4 mg, 0.0971 mmol per AGU) was dissolved in DMF (14 mL), and PSt-N_3 (M_n = 2.2×10^3 g mol^{-1}, *DP* = 20; 386 mg, 0.173 mmol), ascorbic acid (107 mg, 0.607 mmol), and $CuSO_4$•$5H_2O$ (26.2 mg, 0.105 mmol) were added. The reaction and purification conditions were the same as those of **2a**. Yield: 202 mg (72 %). SEC-MALS: M_w = 3.2 × 10^5 g mol^{-1}, M_w/M_n = 1.7.

2-2-2-2. PEO-PSt-bottlebrush

6-O-MeOTr-2,3-di-O-PEO$_{16}$-cellulose (7). The bottlebrush **6** was synthesized according to the modified method of the reported procedure.[7] NaOH (3.35 g, 83.7 mmol) was added into the solution of **7** (1.90 g, 4.37 mmol per AGU) in anhydrous dimethyl sulfoxide (DMSO) (57 mL). After 3 h, one-half of the solution of PEO-I (DP_n = 16; 71.1 g, 82.7 mmol) in anhydrous DMSO (38 mL) was added dropwise over 40 min at room temperature, followed by stirring at 50 °C for 1 day. After 3 day, another one-half portion of PEO-I solution was added over 30 min into the reaction mixture and stirred for 3 h at 50 °C. The reaction mixture was extracted with CH_2Cl_2 (200 mL) and washed with distilled water (5 times), and then the organic phase was dried over Na_2SO_4, concentrated to yield crude product. Then, the crude product was dissolved into CH_2Cl_2 (25 mL) and added the mixture of ethyl acetate and hexane (1: 3 v/v). The precipitate obtained was dried in vacuum oven and the same procedures were repeated 10 times to yield **77** (5.20 g, 75%). SEC: M_w = 1.9×10^5, M_w/M_n = 2.2. ^{1}H NMR (600 MHz, $CDCl_3$): 2.5-5.0 (-O-CH_2-, -Ph-O-CH_3, ring-H), 3.38 (-CH_2-O-CH_3), 3.55 (-CH_2-O-CH_3), 6.0 – 8.5 (-Ph).

*2,3-di-O-PEO$_{16}$-cellulose (**8**)*. The bottlebrush **8** was synthesized according to the modified method of the reported procedure.[10,12] **7** (4.50 g, 2.84 mmol per AGU) was dissolved in tetrahydrofuran (THF) (180 mL) and aq. HCl (35%) (9.0 mL) was added to the solution and stirred at room temperature for 5 h. The reaction mixture was neutralized with triethylamine and concentrated. The sticky mixture was dissolved into CH_2Cl_2 (100 mL) and washed with distilled water (4 times), and then the organic phase was dried over Na_2SO_4, concentrated to yield crude product. This crude product was added into distilled water and the precipitate was removed by centrifugation. The supernatant fluid was filtered and dried under vacuum to yield **8** (3.27 g, 88 %). SEC: $M_w = 1.1\times10^5$, $M_w/M_n = 1.9$. ^{1}H NMR (600 MHz, $CDCl_3$): 2.6-5.0 (-O-C*H*$_2$-, ring-H), 3.38 (-O-C*H*$_3$), 3.55 (-C*H*$_2$-O-CH$_3$). DS_{PEO} (calculated from ^{1}H-NMR) = 1.6.

*6-O-Pentynoyl-2,3-di-O-PEO$_{16}$-cellulose (**9**)*. 1-Ethyl-3-(3-dimethylaminopropyl)carbodiimide hydrochloride (EDC•HCl) (0.962 g, 5.02 mmol), pentynoic acid (0.328 g, 3.34 mmol) and 4-dimethylaminopyridine (0.615 g, 5.03 mmol) were added into the solution of **8** (1.00 g, 0.746 mmol per AGU) in anhydrous dimethylformamide (DMF) (20 mL). The mixture was stirred for 1 d at room temperature, and then stirred for 2 d at 50 °C. The reaction mixture was diluted with distilled water, dialyzed with dialysis membrane (MWCO: 8 kD) for 1 d, and lyophilized to yield **9** (1.04 g, 100%). SEC: $M_w = 6.2\times10^4$, $M_w/M_n = 1.5$. ^{1}H NMR (800 MHz, 80 °C, $C_2D_2Cl_4$): 2.15 (-C≡CH), 2.55 (-C*H*$_2$-CH$_2$-C≡CH), 2.61 (-C*H*$_2$-C≡CH), 3.39 (3H, s, -CH$_2$-O-C*H*$_3$), 3.56 (3H, s, -C*H*$_2$-O-CH$_3$), 3.4 - 3.8 (-CH$_2$-), 2.8 - 5.5 (ring-H). ^{13}C NMR (800 MHz, 80 °C, $C_2D_2Cl_4$): 14.2 (-*C*H$_2$-C≡CH), 33.3 (-*C*H$_2$-CH$_2$-C≡CH), 58.6 (-O-CH$_3$), 62.9 (C6), 69.8 (-C≡*C*H), 69 - 71 (-O-CH$_2$-), 71.1-73.2 (C5), 71.8 (-*C*H$_2$-O-CH$_3$), 78.1 (C4), 82.0 (C2), 82.9 (-*C*≡CH), 83.2 (C3), 102.6 (C1), 170.9 (C=O). $DS_{pentynoyl}$ (calculated from ^{1}H-NMR) = 1.0.

*2,3-di-O-PEO$_{16}$-6-O-PSt$_{60}$-cellulose (**2a**)*. **9** (50.0 mg, 0.0358 mmol per AGU) was dissolved in DMF (4.4 mL), and PSt-N_3 (M_n = 6.4×10^3, *DP* = 60; 376 mg, 0.0585 mmol) and ascorbic acid (57.4 mg, 0.326 mmol) were added into the solution. Copper (II) sulfate pentahydrate ($CuSO_4$•$5H_2O$) (8.0 mg, 0.032 mmol) was added into the solution under Ar atmosphere and stirred at 60 °C for 2 d. The reaction mixture was passed through alumina column and dried under vacuum to yield a brown crude product, which was dissolved in CH_2Cl_2 (1 mL). The solution was poured into the mixture of hexane and cyclohexane (3: 2, v / v) and the precipitate was collected by centrifugation. This procedure was repeated twice, and the final product was dried under vacuum at 60 °C for 6 h to yield **1a** (216 mg, 75 %). SEC-MALS: M_w = 9.7×10^5, M_w/M_n = 2.3. ^{1}H NMR (600 MHz, $CDCl_3$): 0.8 - 1.1 (-CH_2-C*H*$_3$, -C-(CH_3)$_2$), 1.2 - 2.5 (-C*H*$_2$-C*H*Ph-), 2.5- 5.5 (-O-CH_2-, ring H, -C*H*$_2$-CH_3, -N-C*H*(Ph)-CH_2-), 3.38 (-O-CH_3), 3.55 (-C*H*$_2$-O-CH_3), 6.2-7.5 (arom-H, N-C*H*=C).

*2,3-di-O-PEO$_{17}$-6-O-PSt$_{31}$-cellulose (**2b**)*. **9** (100 mg, 0.0715mmol per AGU) was dissolved in DMF (8.6 mL), and PSt-N_3 (M_n = 3.3×10^3, *DP* = 30; 392 mg, 0.117 mmol), ascorbic acid (114 mg, 0.648 mmol), and $CuSO_4$•$5H_2O$ (16.2 mg, 0.0648 mmol) were added for the reaction. Yield: 259 mg (76 %). SEC-MALS: M_w = 6.1×10^5, M_w/M_n = 2.4.

*2,3-di-O-PEO$_{16}$-6-O-PSt$_{20}$-cellulose (**2c**)*. **9** (150 mg, 0.107mmol per AGU) was dissolved in DMF (13 mL), and PSt-N_3 (M_n = 2.2×10^3, *DP* = 20; 397 mg, 0.175 mmol), ascorbic acid (173 mg, 0.980 mmol), and $CuSO_4$•$5H_2O$ (24.4 mg, 0.0977 mmol) were added for the reaction. Yield: 302 mg (75 %). SEC-MALS: M_w = 4.8×10^5, M_w/M_n = 2.4.

2-2-2-3. PCL-PSt-bottlebrush

*6-O-MeOTr-2,3-di-O-PCL-cellulose (**10**)*. **6**, distilled CL, and $Sn(Oct)_2$ (0.05 eq. relative to AGU) were mixed in a gastight Schlenk tube equipped with a Teflon cock in a grove box. The mixture

became homogeneous under heating at 130 °C and stirred for 24 h. After the reaction, the product was precipitated with toluene/ *n*-hexane mixture (5:3, v/v), dissolved in THF, and re-precipitation in toluene/ *n*-hexane mixture to yield **10** as a white solid.

10a. **6** (0.38 g, 1.8 mmol per OH) was reacted with CL (5.0 g, 44 mmol, [CL]/[OH] = 25) in the presence of $Sn(Oct)_2$ (0.013 g, 0.089 mmol) for 10 h. The conversion of CL, determined by ^{1}H-NMR, was almost quantitative. Yield: 4.0 g (75 %). $M_n = 2.7\times10^5$ g mol^{-1} and $M_w/M_n = 3.2$.

10b. **6** (0.95 g, 4.4 mmol per OH) was reacted with CL (25 g, 219 mmol, [CL]/[OH] = 50) in the presence of $Sn(Oct)_2$ (0.031 g, 0.21 mmol) for 24 h. Conversion: almost quant.; Yield: 24.1 g (96 %); $M_n = 4.9\times10^5$ g mol^{-1}; $M_w/M_n = 1.8$.

10c. **6** (0.19 g, 0.88 mmol per OH) was reacted with CL (7.5 g, 66 mmol, [CL]/[OH] = 75) in the presence of $Sn(Oct)_2$ (0.0068 g, 0.047 mmol). Conversion: almost quant.; Yield: 6.0 g (78 %); $M_n = 7.3\times10^5$ g mol^{-1}; $M_w/M_n = 1.5$.

*6-O-MeOTr-2,3-di-O-AcPCL-cellulose (**11**)*. **10c** (5.7 g) was treated with acetic anhydride (25 mL) and pyridine (25 mL) at rt for 2 days under Ar atmosphere. The acetylated polymers **11** were obtained through precipitation in methanol (5.08 g, 89 % yield).

*2,3-di-O-AcPCL-cellulose (**12**)*. The solution of **11** (3 g) in CH_2Cl_2 (75 mL) was stirred with $FeCl_3\cdot6H_2O$ (2.25 g, 3 eq. per AGU) at rt for 1 h under Ar atmosphere. The product was passed through alumina to remove insoluble salts, and the filtrate was concentrated to dryness. The sample was purified by the precipitation with methanol (2.64 g). The reaction yield was evaluated to be 87 % by comparing SEC peak areas.

*2,3-di-O-AcPCL-6i-O-pentynoyl-cellulose (**13**)*. The solution of **12** (2.5 g) in DMF (50 mL) was stirred with pentynoic acid (0.24 g, 15 eq. per AGU), EDC·HCl (0.64 g, 20 eq per AGU), and DMAP (0.41 g, 20 eq per AGU) at 60 ˚C for 3 d under Ar atmosphere. The product was concentrated, dissolved in CH_2Cl_2, and precipitated in methanol. The re-precipitation was repeated several times and the precipitate was collected and dried under vacuum to yield **13** (2.24 g) at 90 % yield.

*2,3-di-O-AcPCL-6i-O-PSt-cellulose (**3**)*. The solution of **13** in DMF (about 2 mM per AGU) was stirred with PSt-N_3 (M_n = ca. 4, 9, or 16 kg mol^{-1}; 1.2 -2 eq), $CuSO_4 \cdot 5H_2O$ (1 eq) and ascorbic acid (10 eq) at 60 ˚C under Ar atmosphere. An aliquot of the solution (0.1 mL) was removed using a syringe, diluted with THF to a known concentration, and analyzed by SEC in order to estimate the conversion of PS-N_3 by the peak area decrement. After the reaction, the solution was dissolved in CH_2Cl_2, passed through alumina, and precipitated in cyclohexane. The re-precipitation in cyclohexane was repeated several times to yield **3a-c**.

3a. **13** (0.20 g, 0.014 mmol per AGU) and PSt-N_3 ($M_n = 4.0\times10^3$ g mol^{-1}, M_w/M_n = 1.1; 0.069 g, 0.017 mmol) were dissolved in DMF (6.7 mL) in the presence of $CuSO_4 \cdot 5H_2O$ (0.0035 g, 0.014 mmol) and ascorbic acid (0.025 g, 0.14 mmol). Yield: 0.14 g (56 %); $M_n = 4.4\times10^5$ g mol^{-1}; M_w/M_n = 2.4.

3b. **13** (0.20 g, 0.014 mmol per AGU) and PSt-N_3 ($M_n = 9.2\times10^3$ g mol^{-1}, M_w/M_n = 1.1; 0.22 g, 0.024 mmol) were dissolved in DMF (6.7 mL) in the presence of $CuSO_4 \cdot 5H_2O$ (0.0035 g, 0.014 mmol) and ascorbic acid (0.025 g, 0.14 mmol.: Yield: 0.29 g (88 %); $M_n = 5.2\times10^5$ g mol^{-1}; M_w/M_n = 2.1.

3c. **13** (0.15 g, 0.011 mmol per AGU) and PSt-N_3 (M_n = 1.6×10^4 g mol^{-1}, M_w/M_n = 1.1; 0.27 g, 0.017 mmol) were dissolved in DMF (5 mL) in the presence of $CuSO_4 \cdot 5H_2O$ (0.013 g, 0.053 mmol) and ascorbic acid (0.093 g, 0.53 mmol). Yield: 0.23 g (71 %); M_n = 3.4×10^5 g mol^{-1}; M_w /M_n = 1.6.

2-2-3. Measurements

Nuclear magnetic resonance (NMR) spectra (600 and 800 MHz) were obtained from AVANCE III 600 or AVANCE III 800 (Bruker, MA, USA) with $CDCl_3$ and $C_2D_2Cl_4$. ^{13}C resonances were assigned by combination of heteronuclear single quantum correlation (HSQC) and H-detected multiple bond coherence (HMBC) spectra. SEC analysis for Janus bottlebrush **3** and intermediates **5** – **7** and **9** – **13** (Scheme 2-1) was conducted with a Shodex GPC-101 system (for SEC), which was equipped with a KF-G (Shodex) guard column, two KF-806 (Shodex) columns, and an RI-101 differential refractometer (Shodex) at a flow rate of 0.8 mL min^{-1} at 40 °C. The eluent was THF and standards were PMMA for **5, 7**–**9** and PSt for **3** and **10**. SEC-MALS analysis for **1a**–**c** and **2a**–**c** was carried out on DAWN HELEOS II instrument (Wyatt Technology, Corp., Santa Barbara, CA, USA, λ = 658 nm) at room temperature (for MALS) combined with the above-mentioned Shodex GPC-101 system except that DMF with LiBr (10 mM) was used as the eluent. The click reaction for synthesis of **1a**–**c** and **2a**–**c** was monitored by SEC using a Tosoh SEC system equipped with a CCPS pump (Tosoh Corp., Tokyo, Japan), KF-G guard column (Shodex), two KF-806L columns (Shodex), a CO-8020 column oven (Tosoh) at 40 °C, and a UV-8020 UV detector (Tosoh). THF with triethylamine (0.5 v%) was used as the eluent at a flow rate of 0.8 mL min^{-1}.

To determine the absolute values of molecular weights from the SEC-MALS data, the refractive index increment $(dn/dc)_1$ of **1** and **2** were calculated from the following equation, respectively:[17]

$$\left(\frac{dn}{dc}\right)_{\mathbf{1}} = \left(\frac{dn}{dc}\right)_{\mathrm{PSt}} w_{\mathrm{PSt}} + \left(\frac{dn}{dc}\right)_{\mathrm{EC}} (1 - w_{\mathrm{PSt}}) \quad (2\text{-}1)$$

$$\left(\frac{dn}{dc}\right)_{\mathbf{2}} = \left(\frac{dn}{dc}\right)_{\mathrm{PEO}} w_{\mathrm{PEO}} + \left(\frac{dn}{dc}\right)_{\mathrm{PSt}} w_{\mathrm{PSt}} + \left(\frac{dn}{dc}\right)_{\mathrm{EC}} (1 - w_{\mathrm{PEO}} - w_{\mathrm{PSt}}) \quad (2\text{-}2)$$

where $(dn/dc)_{PEO}$, $(dn/dc)_{PSt}$, and $(dn/dc)_{EC}$ were the refractive index increments for homopolymer PEO, PSt, and ethyl cellulose (EC), respectively, and w_{PEO} and w_{PSt} were the weight fractions of PEO and PSt in bottlebrushes **1** and **2**, respectively. Instead of the dn/dc value of unsubstituted cellulose, the value for EC was used as the main chain because unsubstituted cellulose does not dissolve in DMF-LiBr. The values $(dn/dc)_{PEO}$, $(dn/dc)_{PSt}$, and $(dn/dc)_{EC}$ were measured to be 0.047, 0.158 and 0.045 mL g^{-1}, respectively, using a differential refractometer (Optilab rEX, Wyatt Technology, λ = 658 nm, at 25 °C). The reasonability of Eq. 1 was confirmed using Janus cellulosic bottlebrush.

Scheme 2-1. Synthesis of cellulosic bottlebrush **1** and cellulosic Janus bottlebrush **2** and **3**[a]

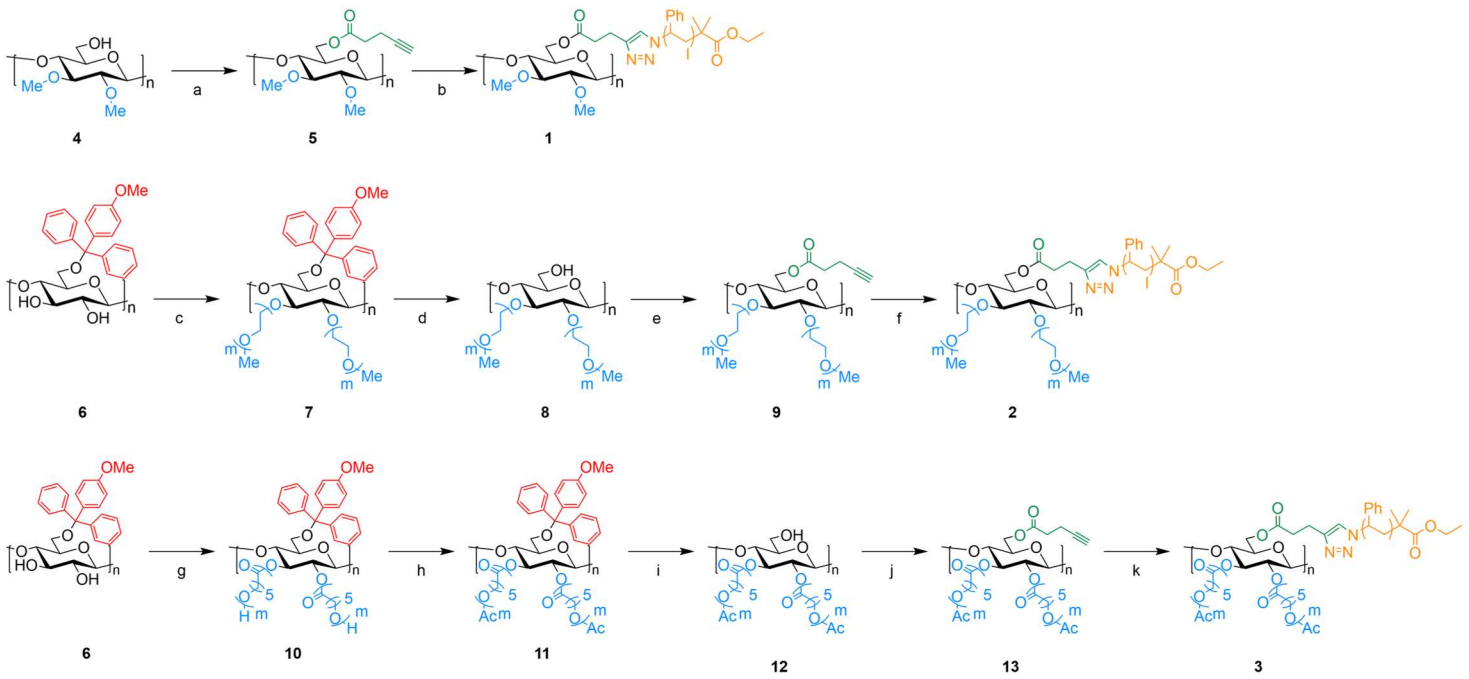

[a]Reagents and conditions: (a) 4-pentynoic acid, EDC•HCl, DMAP, DMF, 80 °C, 2.5 d → rt, 1 d → 60 °C, 1 d; 47 %; (b) PSt-N_3 (l = 60 (for **1a**), 30 (for **1b**), 20 (for **1c**)), $CuSO_4$•$5H_2O$, ascorbic acid, DMF, 60 °C, 2 d; 95 % (**2a**), 60 % (**2b**), 72 % (**2c**); (c) PEO-I, NaOH, DMSO, 50 °C, 4 d, 75 %; (d) HCl, H_2O, THF, rt, 5 h, 88 %; (e) pentynoic acid, EDC•HCl, DMF, rt, 1 d→50 °C, 2 d, 98 %; (f) PSt-N_3 (DP_n = 60 (for **2a**), 30 (for **2b**), 20 (for **2c**)), $CuSO_4$•$5H_2O$, ascorbic acid, DMF, 60 °C, 2 d, 75 % (**1a**), 76 % (**1b**), 75 % (**1c**); (g) CL, $Sn(Oct)_2$, 130 °C, 24h; (h) acetic anhydride, pyridine, r.t., overnight; (i) $FeCl_3 \cdot 6H_2O$, CH_2Cl_2, r.t., 1h; (j) pentynoic acid, EDC·HCl, DMAP, DMF, r.t., 3d; (k) PS-N_3, $CuSO_4 \cdot 5H_2O$, ascorbic acid, DMF, 60 °C, several days.

2-3. Results and Discussion

2-3-1. Synthetic Strategy

Figure 2-1 shows the schematic structures of homo and Janus bottlebrushes targeted in this thesis, and Scheme 2-1 shows their synthetic routes. Trityl group family is known to be applied to a regioselective protecting group for 6-*O* position of cellulose. Among them, MeOTr group is superior to other trityl groups in the viewpoint of the regioselectivity of protection and rapidness of deprotection.[12] Therefore, The author synthesized Janus cellulosic bottlebrush **2** and **3**, and their with regioselectivity from MeOTr-cellulose as a starting material.

In the synthetic route 1, firstly, the author synthesized cellulosic derivative with pentynoyl group at 6-*O* position from 2,3-*O*-dimethylcellulose. Then, introduction of PSt chain was carried out with Cu(I)-catalyzed Huisgen 1,3-dipolar cycloaddition (CuAAC) reaction, one of the most common click reactions. Generally, in the grafting-to method, the reactivity decreases with increasing degree of substitution because of the steric repulsion by already introduced side chains. In this viewpoint, the CuAAC reactions was expected to be suitable for quantitative introduction of side chains because of excellently high reactivity.[14,15]

In the synthetic route 2, the firstly-introducing side chain requires the resistance against an acid condition, under which MeOTr group is removed afterward. Additionally, it requires a big difference in χ parameter from the secondary-introducing side chain.[13] Hence, the author selected PEO as the firstly-introducing side chain. Cowie and coworkers esterified the 2,3-*O* position of tritylcellulose with a monofunctionalized PEO in the presence of NaH to yield 6-*O*-trityl-2,3-di-*O*-PEOcellulose with a DS_{PEO} of ~ 1.9, which is almost quantitative introduction of side chains.[7] Thus, in the same way, the author introduced monofunctionalized PEO at 2,3-*O* positions of **2** via the Williamson ether reaction. After the removal of MeOTr group from **7**, the bottlebrush **8** was modified with pentynoyl group at the 6-*O* position (**9**). Then, PSt chains was introduced to **5** via

grafting-to method with CuAAC reaction to yield **2**.

In the synthetic route 3, the author adopted a grafting-form method for firstly-introducing side chain. Generally, the grafting-from method is superior in the introduction of side chain with high density and high molecular weight. In this route, poly(ε-caprolactone) (PCL) was introduced to the starting material **4** as firstly-introducing side chain because ε-caprolactone could be polymerized directly form the hydroxyl groups at 2,3-*O* positions of **4**. Then, after removal of MeOTr groups, PSt was introduced with CuAAC click reaction.

2-3-2. Preparation and Characterization of Homo Cellulosic Bottlebrush (1a–c)

The pentynoyl group was introduced to residual hydroxyl groups of 2,3-di-*O*-methylcellulose (**4**) (DS_{Me} = 1.8) with the ester condensation reagent EDC•HCl to yield **5**. The ^{1}H NMR spectrum showed peaks ascribed to the protons of the pentynoyl group, cellulose ring, and methyl groups (Figure 2-6a). The $DS_{pentynoyl}$ value was calculated to be 1.2 from the ^{1}H-NMR spectrum of **5**, indicating that the pentynoyl group was quantitatively introduced to the residual hydroxyl group, mainly to *O*-6 position of **5**. The regioselectivity of **5** is confirmed by their ^{13}C NMR spectrum (Figure 2-6b). Figure 2-6b shows sharp peaks at 102.8, 63.0, and 171.3 ppm, attributed to C-1, C-6, and the carbonyl carbon of the pentynoyl group, respectively. This clearly shows that the pentynoyl group was highly regioselectively introduced at the *O*-6 position.

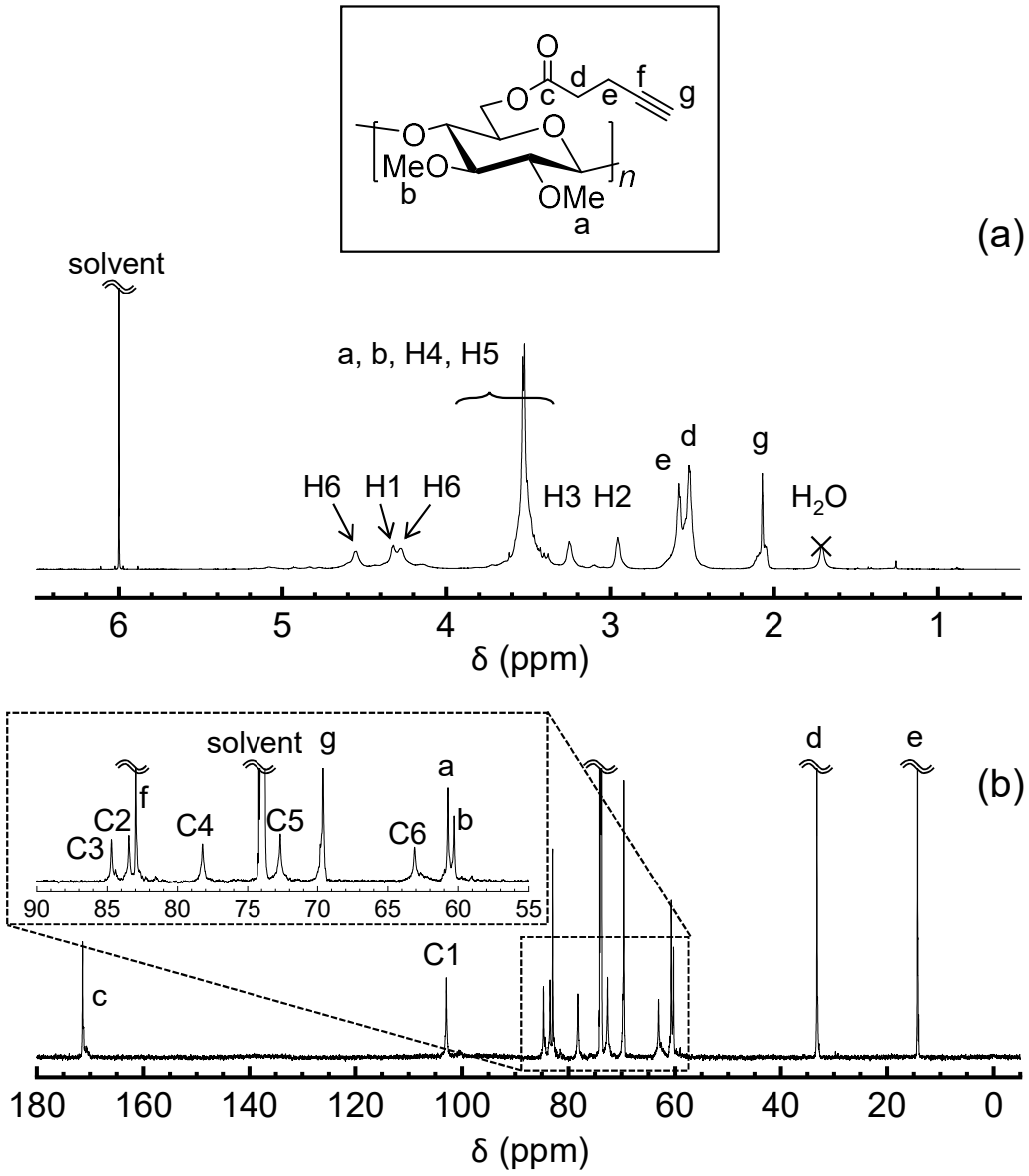

Figure 2-6. (a) ^{1}H and (b) ^{13}C NMR spectra of **5** ($C_2D_2Cl_4$, 27 °C, 800 MHz).

CuAAC click reactions between **5** and the PSt-N_3 species were carried out in the same condition for Janus cellulosic bottlebrushes. The DP_{PSt} values were calculated only via SEC analysis because the ^{1}H NMR spectra of **1a–c** purified after the completed reaction of showed almost only peak contributed to PSt chains (Figure 2-7) and it is difficult to calculate the weight fraction of PSt chain in the whole of cellulosic bottlebrush. Figure 2-8 shows the SEC profiles of the mixtures of **5** and the PSt-N_3 before (dotted line) and after (solid line) the coupling reaction,

as detected by UV. Note that the starting material **5** was invisible by UV detection. The profiles after the reaction show a decreased peak assigned to the PSt-N_3 starting material. On the other hand, an additional peak corresponding to **1** appears in a high molecular weight range. From the area ratio of these two peaks, the value of DP_{PSt} were calculated to be 1.1, 1.1, and 1.2 for **1a**, **1b**, and **1c**, respectively. SEC profiles indicated that PSt chains were qualitatively introduced to **5** since those values were almost equivalent to the $DS_{pentynoyl}$ (= 1.2). Consequently, the author concluded that the grafting-to method with CuAAC reaction was suitable to for quantitative introduction of PSt chains to the cellulose derivative.

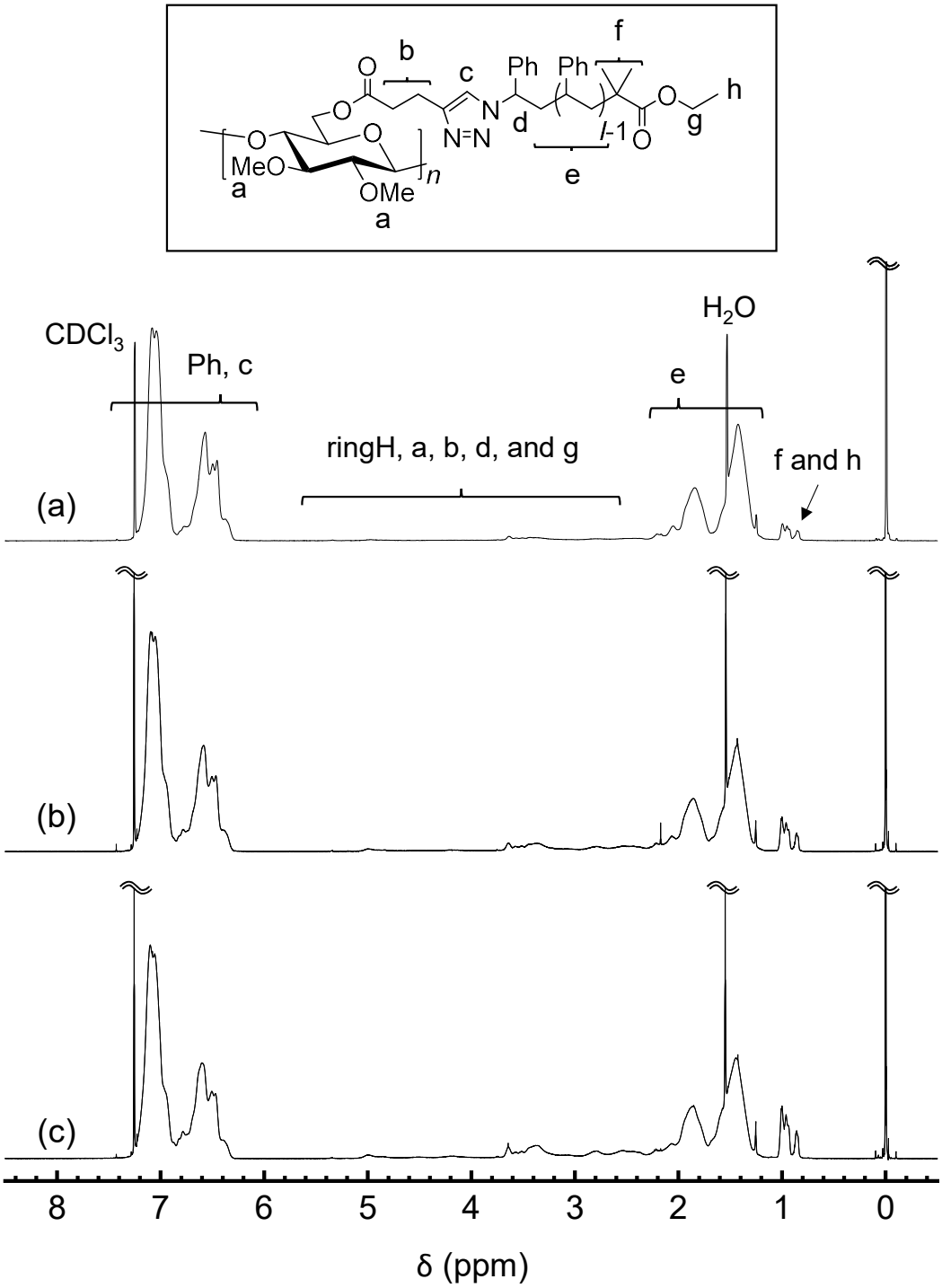

Figure 2-7. ^{1}H NMR spectrum of **1a** (a), **1b** (b) and **1c** (c) ($CDCl_3$, rt, 600 MHz).

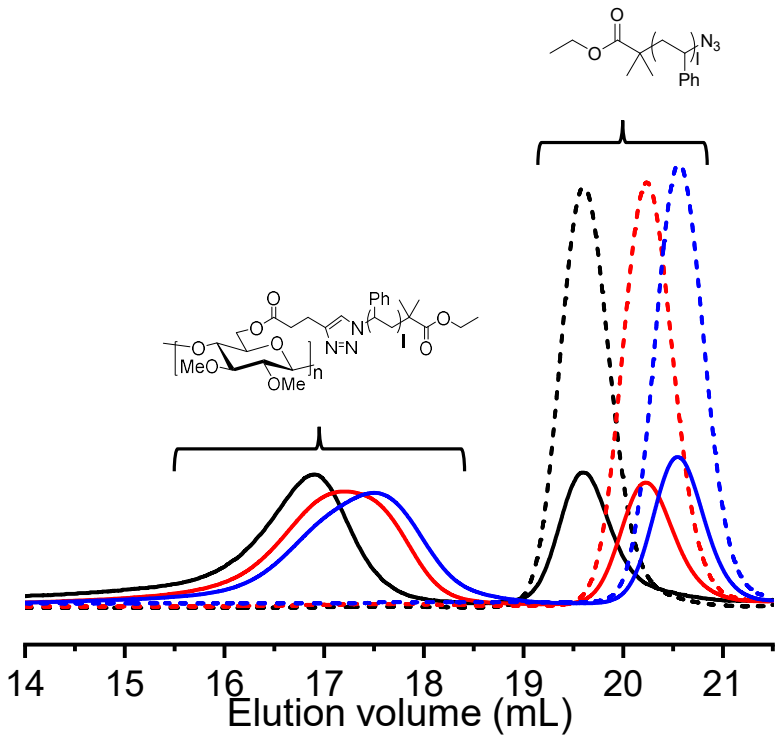

Figure 2-8. SEC charts before (dotted line) and after (solid line) the coupling reaction between **5** and PSt-N_3 for l = 60 (black), 30 (red), and 20 (blue) for the synthesis of **1a**, **1b**, and **1c**, respectively; UV detector (wavelength: 254 nm); THF/triethylamine (0.5 vol%) as eluent).

2-3-3. Preparation and Characterization of Janus Cellulosic Bottlebrush (2a–c)

Firstly, the residual hydroxyl groups of **6** were etherified with PEO-I (MW = 860, DP_n = 16) using NaOH to yield **7**, following the deprotection of MeOTr group with HCl to yield **8**. In the ^{1}H NMR spectrum of **8** (Figure 2-2), the peak derived from methylene of PEO appears at δ = 3.34 ppm but that from MeOTr group disappears at around 7 ppm, indicating that the etherification and the removal of MeOTr group proceeded. DS_{PEO} was evaluated to be 1.6 from ^{1}H NMR spectra of the completely propionated **8**. Subsequently, the pentynoyl group was introduced through ester condensation reaction to yield **9**. The ^{1}H NMR spectrum of **9** exhibited

the peaks derived from protons of pentynoyl group, cellulose ring proton, and PEO side chains (Figure 2-3a). DS_{PEO} and $DS_{pentynoyl}$ were evaluated to be 1.6 and 1.04, respectively, from ^{1}H NMR spectra. In addition, the peaks assigned to C-1, C-6 and carbonyl carbon of pentynoyl group at 102.6, 62.9, and 170.9 ppm, respectively, in ^{13}C NMR spectrum (Figure 2-3b) confirm regioselective functionalization with PEO and pentynoyl groups at *O*-2,3 and *O*-6 positions, respectively. Since the reactivity of hydroxyl group at 6-*O* position is higher than that at 2,3-*O* position, pentynoyl groups might be introduced mainly to 6-*O* position, though the cellulosic bottlebrush **8**, the precursor of **9**, had unsubstituted hydroxyl groups at 2,3-*O* position. In comparison with **5**, however, the ^{13}C NMR spectrum of **9** showed broader peak. This could be explained by the following two reasons. One is that **5** had fewer substituted groups of the main chain not to lose the mobility of main chain Another is that **5** went through a regioselective and qualitative introduction of side chains.

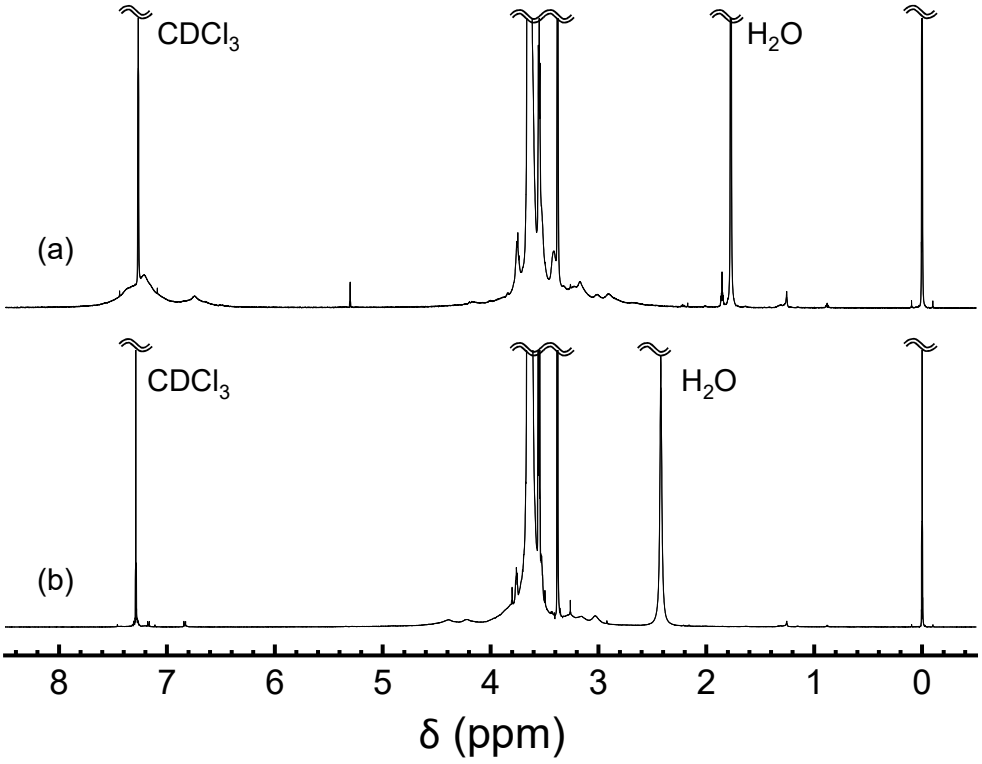

Figure 2-2. ^{1}H-NMR spectrum of **7** (a) and **8** (b) in $CDCl_3$.

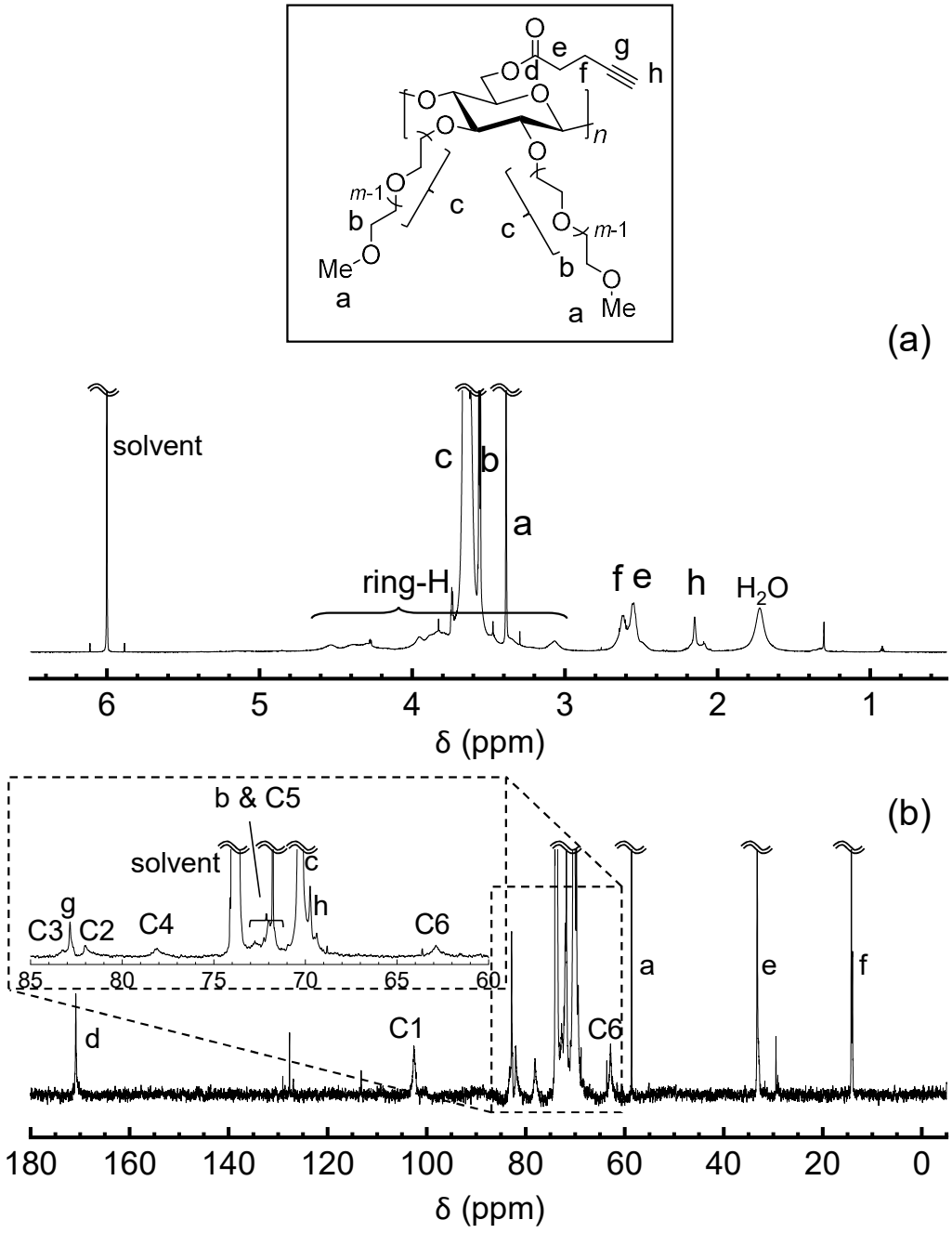

Figure 2-3. (a)^{1}H and (b)^{13}C NMR spectra of **9** ($C_2D_2Cl_4$, 80 ºC, 800 MHz).

CuAAC click reaction between **9** and three kinds of PSt-N_3 (M_n = 6.4 × 10^3, DP_n = 60; M_n = 3.3 × 10^3, DP_n = 30; M_n = 2.2 × 10^3, DP_n = 20) was carried out with $CuSO_4$•$5H_2O$ and ascorbic acid to obtain **2a**–**c**. Figure 2-4 represents ^{1}H NMR spectra of **2a**–**c**. There are the peaks

derived from ring proton and PEO side chains (2.70 - 5.25 ppm) and those of the ethoxycarbonylisopropyl group at the end of PSt chain (δ = 0.8 - 1.1 ppm; peak h and j). The amount of PSt chain of **2a**–**c** proved to be 1.0, 1.0 and 1.1 chains per AGU from the peak ratio of these two peaks, respectively. Figure 2-5 shows the SEC profiles of the mixture of **9** and PSt-N_3 before (dotted line) and after (solid line) the coupling reaction, detected by UV (λ = 254 nm). The former profile showed only one peak derived from unreacted PSt-N_3 since **6** was UV-inactive, while the latter exhibited both the decreased peak of the unreacted PSt-N_3 and the additional peak corresponding to **2** in a high molecular weight range. By comparing these two peak areas, the *DP* for PSt side chains (DP_{PSt}) were calculated to be 1.0, 1.0 and 1.1 for **2a**, **2b** and **22c**, respectively. The match of DP_{PSt} evaluated in the different ways supports that cycloaddition reaction between **9** and PSt-N_3 proceeded quantitatively. Additionally, the values of DP_{PSt} for **2a**–**c** reached to the value of $DS_{pentynoyl}$ of **6** (1.04), indicating that qualitative coupling reaction between PEOcellulose (**9**) and PSt chains. From above results, the author concluded that the compounds **2a**–**c** were the target Janus cellulosic bottlebrush which possessed two kind of side chains with high density and regioselectively.

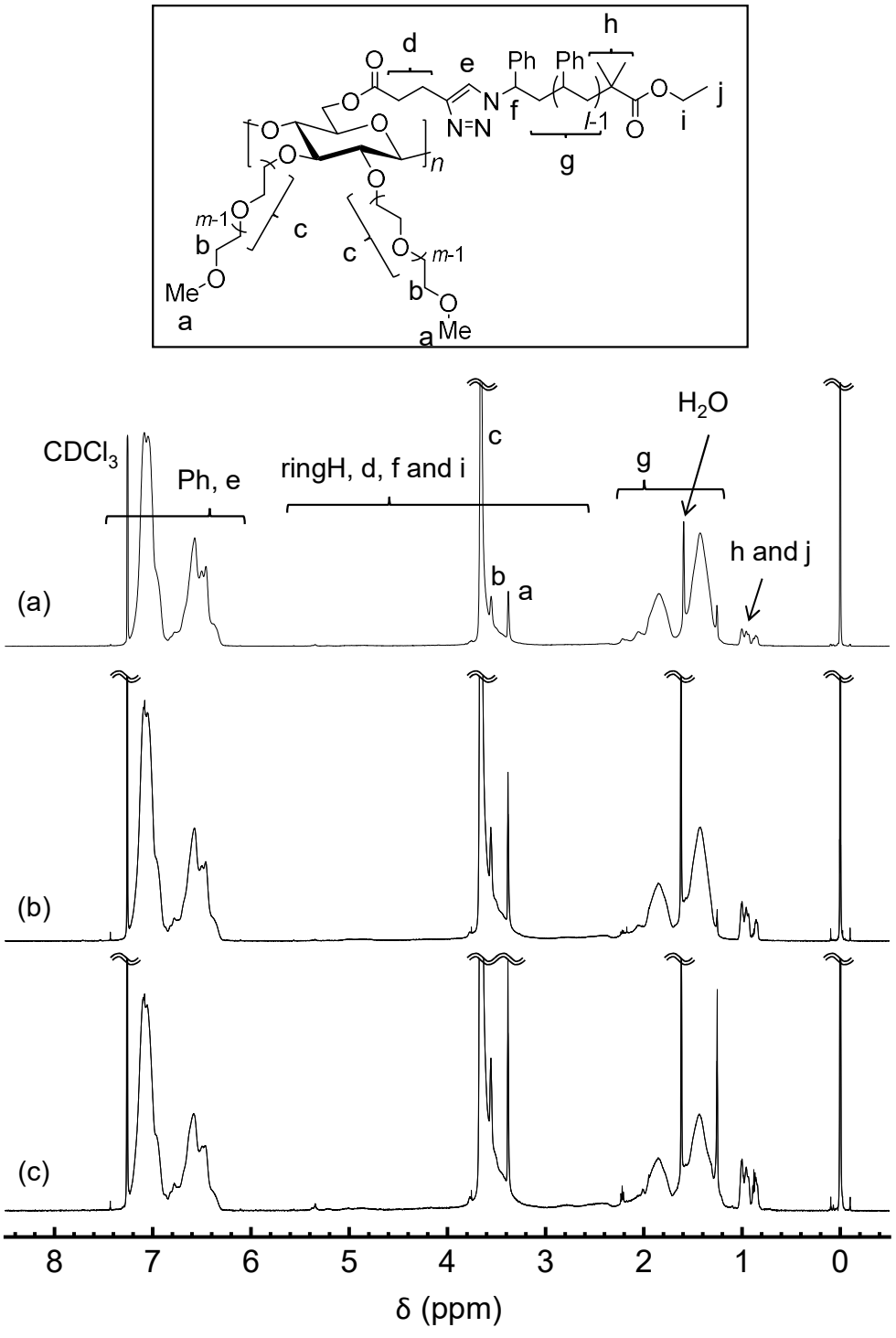

Figure 2-4. ^{1}H NMR spectrum of **2a** (a), **2b** (b) and **2c** (c) ($CDCl_3$, rt, 600 MHz).

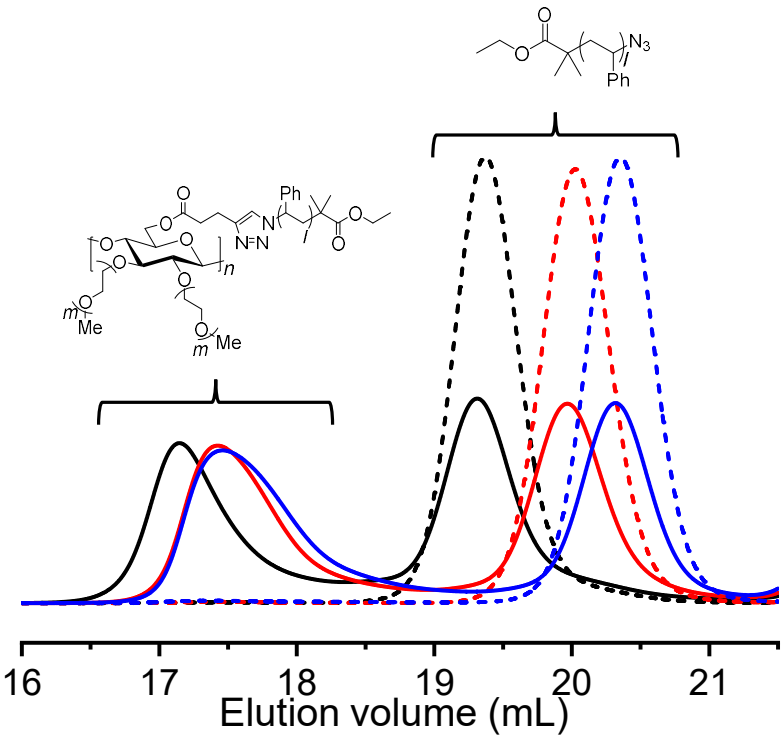

Figure 2-5. SEC charts before (dotted line) and after (solid line) the coupling reaction

Table 2-1. Characteristics of cellulosic bottlebrushes **1a–c** and **2a–c**.

		sample	MW_{PEO} or MW_{Me}	DS_{PEO} or DS_{Me}	$DS_{pentynoyl}$	DS_{PSt}	$M_{n,PSt}$ (g/mol)	M_0 (g/mol)	$w_{backbone}$[a]	w_{PEO}[a]	w_{PSt}[a]	dn/dc[b] (mL/g)	M_w[c] (mL/g)	DP_w[c]	M_w/M_n[c]
Janus	PEO-PSt-cellulose	**2a**	732	1.6	1.0	1.0	6.4×10^3	8.1×10^3	0.03	0.14	083	0.139	9.7×10^5	1.2×10^2	2.3
		2b	732	1.6	1.0	1.0	3.3×10^3	4.7×10^3	0.05	0.24	0.71	0.126	6.1×10^5	1.3×10^2	2.4
		2c	732	1.6	1.0	1.1	2.2×10^3	3.8×10^3	0.06	0.31	0.63	0.117	4.8×10^5	1.3×10^2	2.4
Homo	PSt-cellulose	**1a**	14	1.8	1.2	1.1	6.4×10^3	7.4×10^3	0.04	—	0.96	0.154	8.1×10^5	1.1×10^2	1.6
		1b	14	1.8	1.2	1.1	3.3×10^3	3.8×10^3	0.07	—	0.93	0.150	4.6×10^5	1.2×10^2	1.7
		1c	14	1.8	1.2	1.2	2.2×10^3	2.9×10^3	0.10	—	0.90	0.148	3.2×10^5	1.1×10^2	1.7
	PEO-cellulose	**9**	732	1.6	1.8	—	—	1.4×10^3	—	—	—	—	6.2×10^4 [d]	4.4×10^2 [d]	1.5 [d]

[a]Weight fraction of the main chain and PSt chains. [b]Refractive index increment calculated from Eq. 1. [c]Determined by SEC-MALS in DMF/LiBr with PMMA standard.

Table 2-1 summarizes the characteristics of Janus bottlebrushes **1a**–**c** and cellulosic bottlebrush **2a**–**c**. The DP_w (instead of M_w) and DP_w/DP_n (= M_w/M_n) values of main chains of Janus cellulosic bottlebrushes **1a**–**c** and cellulosic bottlebrushes **2a**–**c** were almost same, respectively, where DP_w = 1.2 – 1.3×10^2 for **1a**–**c** and DP_w = 1.1 – 1.2×10^2 for **2a**–**c**. Thus, the author concluded that **1a**–**c** and **2a**–**c** were molecularly dispersed and hence their molecular wights correctly measured without their intramolecular aggregation or adsorption to the column in DMF/LiBr by SEC-MALS. All Janus cellulosic bottlebrushes **1a**–**c** and cellulosic bottlebrushes **2a**–**c** had longer stretched main chain than 15 nm and shorter stretched side chain than 15 nm, meaning that their conformation is not star-like but cylinder-like bottlebrush. the author expects that Janus cellulosic bottlebrushes **1a**–**c** form helical second or higher order structure. The more detailed analysis of second structure is discussed in the following chapters.

2-3-4. Preparation and Characterization of Janus Cellulosic Bottlebrush (3a–c)

The preparation of Janus cellulosic bottlebrushes **6** with PCL and PS was accomplished via a protecting group strategy (Scheme 2-1). Firstly, PCL was grafted onto MeOTr-cellulose (**4**) using $Sn(Oct)_2$ as a catalyst by ring-opening polymerization, yielding PCL-grafted cellulose **10** **(**Table 2-2). The PCL chain length was controlled by the initial feed ratio [CL]/[OH] of 25, 50, and 75. The starting material **6** was soluble in CL, so that the bulk polymerization was performed with keeping homogeneous state throughout the polymerization. The *DP* of PCL side chains (DP_{PCL}) was estimated from the ^{1}H-NMR spectrum (Figure 2-9), based on the comparison of the signals at 4.06 ppm (ε-methylene protons of the grafts) and at 3.65 ppm (ε'-methylene protons of the graft ω-end).[18] The *DS* of the PCL grafts (DS_{PCL}) was then estimated based on the comparison between the initial feed ratio [CL]/[OH] and the DP_{PCL}. When [CL]/[OH]=75, the DS_{PCL} was 1.5,

close to the value of complete substitution (that is, 2). The sample **10c** was then used to the following reaction.

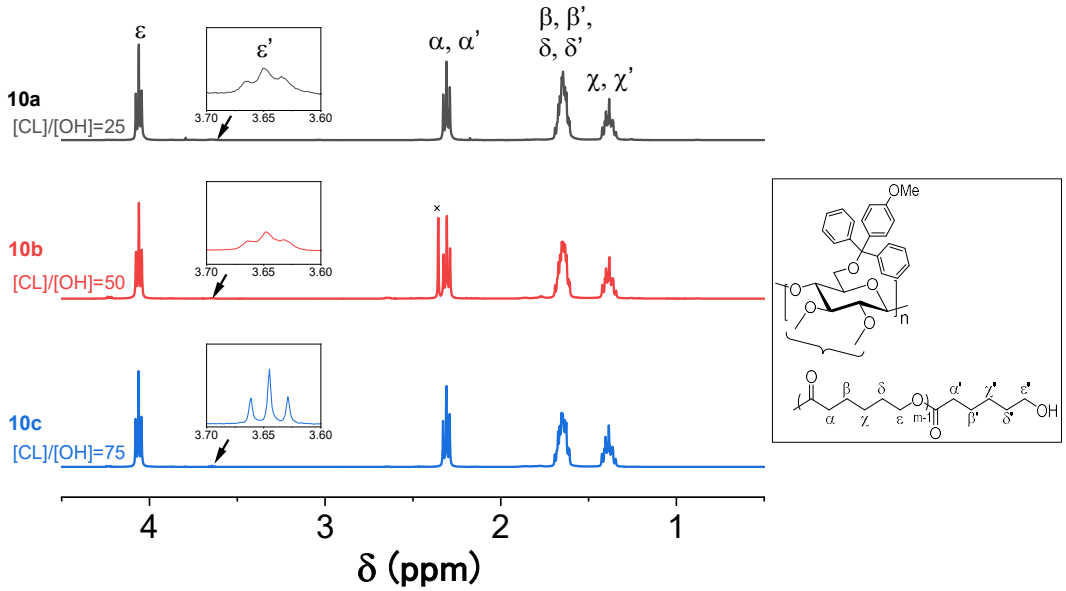

Figure 2-9. ^{1}H-NMR spectra for **10a-c** in $CDCl_3$.

Table 2-2. Ring-opening polymerization of CL with MeOTr-cellulose (**4**).[a]

Sample	[CL]/[OH][b]	Conv.[c] (%)	M_n[d] (10^5 g mol^{-1})	M_w/M_n[d]	DP_{PCL}[e]	DS_{PCL}[e]
10a	25	> 99	2.7	3.2	50	1.0
10b	50	> 99	4.9	1.8	104	1.0
10c	75	> 99	7.3	1.5	100	1.5

[a][Sn(Oct)$_2$] = 0.05 mol L^{-1}; polymerization temperature: 130 °C, time: 24h. [b]Molar ratio of CL and hydroxyl groups of **6**. [c]Conversion of CL, determined by ^{1}H-NMR. [d]Determined by SEC in THF using PSt standards. [e]Determined by ^{1}H-NMR.

The unreacted/PCL-terminal hydroxyl groups of **10c** were acetylated and subjected to remove the MeOTr groups in an acidic condition. This step is crucial, since PCL chains are labile to acid

hydrolysis. We first used HCl, but acid hydrolysis of PCL side chains proceeded rapidly. Then, the detritylation using a Lewis acid $FeCl_3$ was applied. Figure 2-10a exhibits that the area of the UV-detected SEC profile of **12** was decreased to be 76 % as compared to the UV-area of the starting material **11**. In addition, the hydrolyzed portion of the PCL side chains was successfully inhibited, judging from the fact that the RI-peak was not changed significantly.

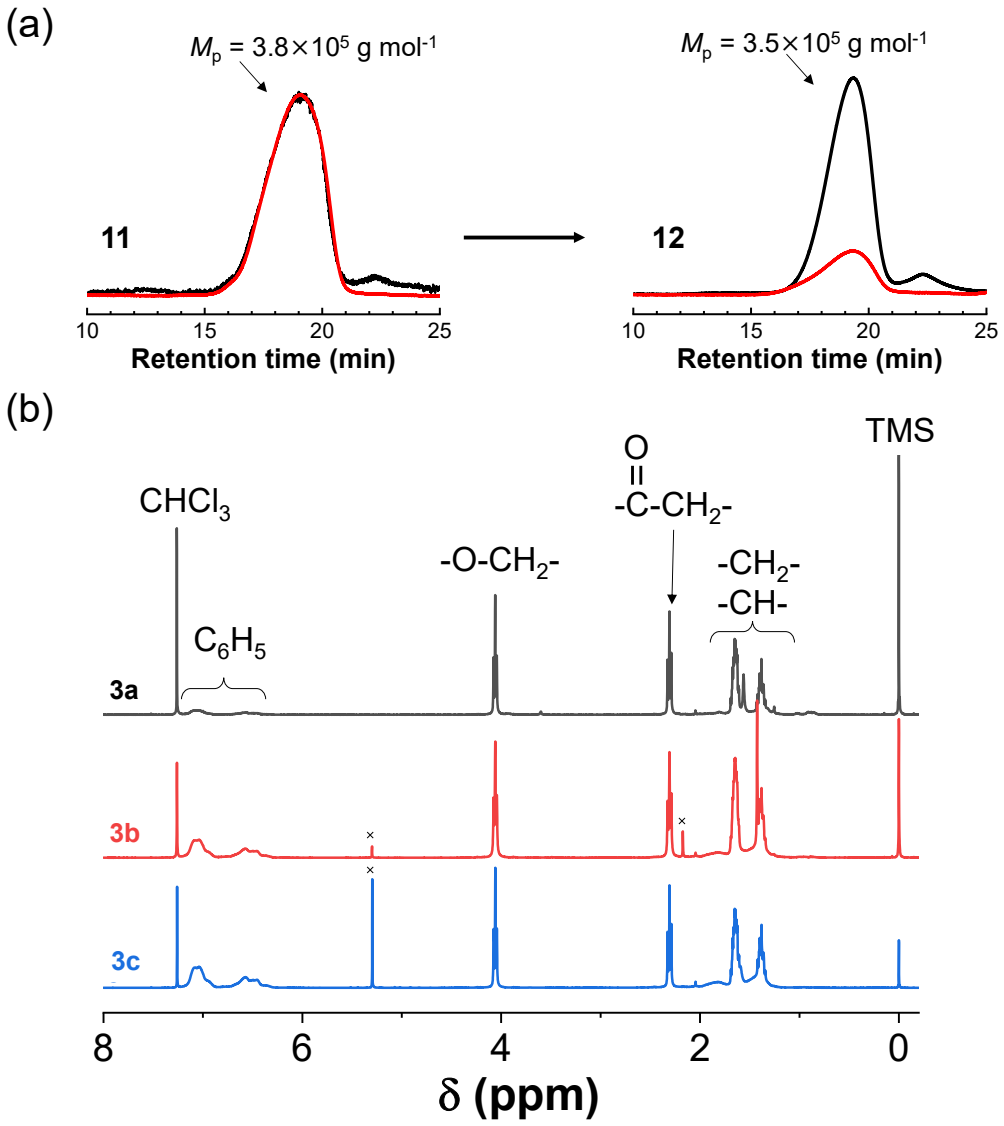

Figure 2-10. (a) Normalized SEC profiles for **11** and **12** (detector: RI (black) and UV-vis (red)). (b) ^{1}H-NMR spectra of **3a-c** in $CDCl_3$.

After the introduction of pentynoyl group at the 6-*O* position, the grafting of the PSt chains, synthesized via ATRP and the subsequent terminal azidation, was conducted through the CuAAC click reaction to prepare Janus bottlebrushes **3a-c** (Table 2-3). The degree of the introduction of the PSt chains (DS_{PSt}) was estimated by SEC analysis. The final DS_{PSt} values of **3a**, **3b**, and **3c** were calculated to be 0.84, 0.75, and 0.64 for PSt with 4.0, 9.2, and 16.0×10^4 g mol^{-1}, respectively (Table 2-3). Figure 2-10b shows the ^{1}H-NMR of **3a-c**. Though peaks from the cellulosic backbone were hardly observed, the peaks of the grafted PCL and PSt were clearly observed. The volume fraction was calculated from the comparison of the peak areas between the PSt aromatic protons at around 6.2 – 7.2 ppm and the PCL ε-methylene protons at 4.0 ppm.

Table 2-3. Results of the grafting of PSt-N_3.[a]

Sample	Grafted PSt-N_3	Bottlebrush			
	M_n (g mol^{-1})	DS_{PSt}	f_{PSt} : f_{PCL}[b]	M_n (g mol^{-1})	M_w /M_n
3a	4.0×10^3	0.84	0.20 : 0.80	4.4×10^5	2.4
3b	9.2×10^3	0.75	0.44 : 0.56	5.2×10^5	2.1
3c	16.0×10^4	0.64	0.54 : 0.46	3.4×10^5	1.6

[a] DP_{PCL} of **3** was assumed to be 100 (see **10c**, Table 2-2). [b] Volume fraction ratio of PSt and PCL, determined by ^{1}H-NMR.

2-4. Conclusion

In this chapter, the author established the methodology to synthesize a series of cellulosic bottlebrushes; homo bottlebrush with one- and two-arm, and hetero bottlebrush with three-arm (Janus bottlebrush). As for Janus cellulosic bottlebrush **2a-c**, the click reaction allowed almost quantitative grafting-to reaction with the secondary-introducing PSt side chains with molecular weights up to 6000 g/mol against steric hindrance around the reaction position. The author confirmed that these bottlebrushes had side chains with high regioselectivity and high

density via the characterization with ^{1}H NMR and SEC measurements. On the other hand, the DS_{PSt} values did not reached to 1 in Janus cellulosic bottlebrush **3a-c**. There may be a possibility that the steric hindrance form PCL chain as well as low $DS_{pentynoyl}$ value of the precursor **13**. However, this strategy is prior to twice grafting-to method from the viewpoint of easier synthesis of high molecular weight of side chain.

Acknowledgment

High-resolution 600 and 800 MHz NMR spectra were acquired with the NMR spectrometer in the Joint Usage/Research Center (JURC) at the Institute for Chemical Research, Kyoto University.

2-5. References

1. French, A. D.; Johnson, G. P. What Crystals of Small Analogs Are Trying to Tell Us about Cellulose Structure. *Cellulose* **2004**, *11*, 5-22.
2. Conley, K.; Godbout, L.; Whitehead, M. A.; van de Ven, T. G. Origin of the Twist of Cellulosic Materials. *Carbohydr. Polym.* **2016**, *135*, 285-299.
3. Ikai, T.; Okamoto, Y. Structure Control of Polysaccharide Derivatives for Efficient Separation of Enantiomers by Chromatography. *Chem. Rev.* **2009**, *109*, 6077-6101.
4. Harkness, B. R.; Gray, D. G. Chiroptical Properties of 6-*O*-a-(1-Naphthylmethyl)-2,3-di-*O*-Pentylcellulose. *Macromolecules* **1991**, *24*, 1800-1805.
5. Redl, F. X.; Lutz, M.; Daub, J. Chemistry of Porphyrin-Appended Cellulose Strands with a Helical Structure: Spectroscopy, Electrochemistry, and in situ Circular Dichroism Spectroelectrochemistry. *Chem. Eur. J.* **2001**, *7*, 5350-5358.
6. Gray, D. G. Chemical Characteristics of Cellulosic Liquid Crystals. *Faraday Discuss. Chem. Soc.* **1985**, *79*, 257-264.
7. Yue, Z.; Cowie, J. M. G. Preparation and Chiroptical Properties of a Regioselectively Substituted Cellulose Ether with PEO Side Chains. *Macromolecules* **2002**, *35*, 6572-6577.

8. Yuan, W.; Zhang, J.; Zou, H.; Shen, T.; Ren, J. Amphiphilic Ethyl Cellulose Brush Polymers with Mono and Dual Side Chains: Facile Synthesis, Self-Assembly, and Tunable Temperature-pH Responsivities. *Polymer* **2012**, *53*, 956-966.
9. Yan, Q.; Yuan, J.; Zhang, F.; Sui, X.; Xie, X.; Yin, Y.; Wang, S.; Wei, Y. Cellulose-Based Dual Graft Molecular Brushes as Potential Drug Nanocarriers: Stimulus-Responsive Micelles, Self-Assembled Phase Transition Behavior, and Tunable Crystalline Morphologies. *Biomacromolecules* **2009**, *10*, 2033-2042.
10. Ifuku, S.; Kadla, J. F. Preparation of a Thermosensitive Highly Regioselective Cellulose/*N*-Isopropylacrylamide Copolymer through Atom Transfer Radical Polymerization. *Biomacromolecules* **2008**, *9*, 3308-13.
11. Olszewski, M.; Li, L.; Xie, G.; Keith, A.; Sheiko, S. S.; Matyjaszewski, K. Degradable Cellulose-Based Polymer Brushes with Controlled Grafting Densities. *J. Polym. Sci., Part A: Polym. Chem.* **2019**, *57*, 2426-2435.
12. Gömez, J. A. C.; Erler, U. W.; Klemm, D. O. 4-Methoxy Substituted Trityl Groups in 6-O Protection of Cellulose: Homogeneous Synthesis, Characterization, Detritylation. *Macromol. Chem. Phys.* **1996**, *197*, 953-964.
13. Grulke, E. A. Solubility Parameter Values. In *Polymer Handbook*, 4th ed.; Brandrup, J.; Immergut, E. H.; Grulke, E. A., Eds. Wiley: New York, 1999; pp VI-675 - VI-714.
14. Gao, H.; Matyjaszewski, K. Synthesis of Molecular Brushes by "Grafting onto" Method: Combination of ATRP and Click Reactions. *J. Am. Chem. Soc.* **2007**, *129*, 6633-6639.
15. Zhao, P.; Yan, Y.; Feng, X.; Liu, L.; Wang, C.; Chen, Y. Highly Efficient Synthesis of Polymer Brushes with PEO and PCL as Side Chains via Click Chemistry. *Polymer* **2012**, *53*, 1992-2000.
16. Matyjaszewski, K.; Nakagawa, Y.; Gaynor, S. G. Synthesis of wWll-Defined Azido and Amino End-Functionalized Polystyrene by Atom Transfer Radical Polymerization. *Macromol. Rapid Commun.* **1997**, *18*, 1057-1066.
17. Benoit, H.; Froelich, D. Application of Light Scattering to Copolymers. In *Light Scattering from Polymer Solutions*, Huglin, M. B., Ed. Academic Press: London and New York, 1972; pp 467-501.
18. Aoi, K.; Aoi, H.; Okada, M. Synthesis of a Poly(vinyl alcohol)-Based Graft Copolymer Having Poly(e-caprolactone) Side Chains by Solution Polymerization. *Macromol. Chem. Phys.* **2002**, *203*, 1018.

Chapter 3

Conformations of Side and Main Chains of Homo Cellulosic Bottlebrushes in Solution

3-1. Introduction

A bottlebrush is a graft or comb-like polymer with highly dense side chains along a main chain. In a good solvent, the side chains are stretched to the direction perpendicular to the main chain because of the excluded-volume effect among side chains. Therefore, the main chain is stretched and stiffened to recover the conformational enthalpy of side chains. With increasing density of side chains and/or increasing affinity between the side chain and solvent, the bottlebrush becomes thicker, and hence the main chain becomes stiffer owing to the excluded-volume effect among side chains. The conformations of main and side chains are theoretically, experimentally, and computationally studied. Especially, the conformation of main chain is quantified with the Kratky-Porod wormlike (KP) chain model, which is equivalent to an elastic wire model.[1] The KP model contains a stiffness parameter λ^{-1}, which increases with increasing stiffness of the main chain.

Nakamura and coworkers synthesized bottlebrushes consisting of main and side chains of polystyrene (PSt) and experimentally revealed the effect of degree of polymerization of side chain and solvent quality on the conformation of the main chain.[2-4] Additionally, they synthesized bottlebrushes which have polybutadiene as a main chain and PSt as side chains and studied the effect of the side-chain density along the main chain on their conformation.[5] Most of the experimental studies including their works targeted the bottlebrushes with flexible synthetic polymer segments in a sufficiently good solvent. Much less work has been experimentally done

on bottlebrushes with a semi-flexible main chain and highly dese side chains in a good as well as poor solvent.

Cellulose is one of naturally occurring polymers, consisting of anhydroglucose units (AGUs) joined by β-(1,4)-glucosidic bonds. Cellulose has a stiff main chain and a chiral center in the repeating unit to show fascinating properties.[6] For instance, cellulose and its derivatives could form cholesteric liquid crystals[7] and be used for chiral column chromatography.[8] From the viewpoints not only of the fundamental aspects but also of highly potential applications, their conformation in a solution have attracted much attention. The author set a goal of this chapter to reveal the side-chain conformation and its effect on the main-chain stiffness for a cellulosic bottlebrush with a PSt side chain every repeating AGU in a poor solvent (for the side chain). Owing to such a rather low density, the side chain was expected to have a sufficient space as to study the cross-over in the side-chain conformation from globule to stretched coil as a function of side-chain length.[9] The author carried out the small X-ray scattering (SAXS) and size-exclusion chromatography-multi angle light scattering (SEC-MALS) measurements for the bottlebrushes (PSt-cellulose) with cellulose as main chain and PSt as side chain at the 6-*O* position in order to estimate the thickness and the main-chain stiffness of the bottlebrushes in DMF/LiBr. The determined parameter was compared with those for cellulosic derivatives and the PSt-PSt bottlebrush to discuss the relationship between the effect of the intrinsic stiffness of cellulosic main chain on the bottlebrush characteristics.

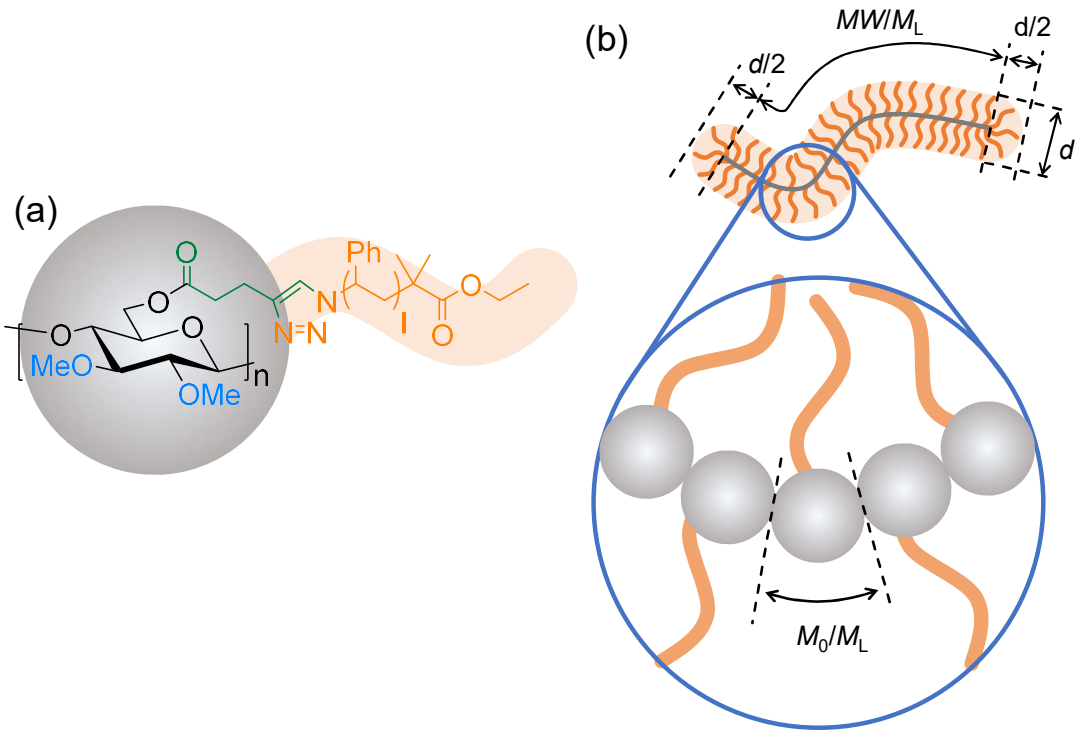

Figure 3-1. (a) Chemical structure of the cellulosic bottlebrushes **2** with PSt side chains: l = 60 (**1a**), 30 (**1b**), and 20 (**1c**). (b) Schematic illustration of the conformation of **2** in dilute solution: d, bottlebrush diameter; d, apparent contribution of side chains located at both ends of the main chain; MW, molecular weight; M_L, molecular weight per unit contour length; M_0, molecular weight per repeating unit.

3-2. Experimental Section

3-2-1. Samples.

The studied cellulosic bottlebrushes of a PSt side chain (of different molecular weights) in every AGU were synthesized and characterized in the previous chapter. Their molecular characteristics are listed in Table 3-1.

Table 3-1. Characteristics of PSt-cellulose **1a–c**.

sample	DS_{Me}	DS_{PSt}	$M_{n,PSt}$	$w_{main\ chain}$[a]	w_{PSt}[a]	dn/dc[b]	M_w[c]	DP_w[c]	M_w/M_n[c]
1a	1.8	1.1	6400	0.04	0.96	0.154	8.1×10^5	1.1×10^2	1.6
1b	1.8	1.1	3300	0.07	0.93	0.150	4.6×10^5	1.2×10^2	1.7
1c	1.8	1.2	2200	0.10	0.90	0.148	3.2×10^5	1.1×10^2	1.7

[a]Weight fraction of the main chain and PSt chains. [b]Refractive index increment calculated from Equation 2-2. [c]Determined by SEC-MALS in LiBr/DMF.

3-2-2. Instrumentation and Measurements.

SEC-MALS analysis for PSt-cellulose was carried out using a DAWN HELEOS instrument (Wyatt Technology Corp., Santa Barbara, CA, USA, λ = 658 nm) at room temperature (for MALS) combined with Shodex GPC-101 system (for SEC), which was equipped with a KF-G (Shodex) guard column, two KF-806L (Shodex) columns, and an RI-71S differential refractometer (Shodex). Dimethylformamide (DMF) with LiBr (10 mM) was used as the eluent. To determine the weight-average molecular weight M_w, the mean-square radius of gyration $\langle S^2 \rangle$, and polydispersity index M_w/M_n with MALS, the Berry plot was used. The refractive index increment (dn/dc) of **1a–c** was calculated using Equation 2-2 in chapter 2:[10]

SAXS measurements were carried out at room temperature using BL40B2 at SPring-8 (Hyogo, Japan). Each SAXS profile was obtained using an imaging plate (RIGAKU R-AXIS VII) with a frame size of 3000 × 3000 pixels and a pixel size of 100 × 100 μm^2. The X-ray wavelength was 1.000 Å. The camera length was calibrated to be 1654 mm using the diffraction peaks of silver behenate. The excess scattering intensity $I(q)$ was obtained as the difference of scattering intensity between the solution and the pure solvent. Each solution of PSt-cellulose at a concentration of 0.5

w/v% in DMF/LiBr (10 mM) was introduced into a flat cell (width, 3 mm) equipped with a pair of thin quartz glass windows (thickness, 20 μm).

3-3. Results and Discussion

3-3-1. Cross-Sectional Diameters of Bottlebrushes and Conformation of Side Chain.

In order to estimate the conformation of side chain of bottlebrush **1a–c**, their thickness was evaluated by SAXS measurements in DMF/LiBr. When the bottlebrush is stretched and take a cylindrical conformation, its cross-sectional radius of gyration (S_c) is described by the following cross-sectional Guinier approximation:[11]

$$\ln[qI(q)] = C - \frac{1}{2}{S_c}^2 q^2 \tag{3-1}$$

where q, $I(q)$ and C represent scattering vector, scattering intensity and the constant factor, respectively. Here, q is defined by the following equation:

$$q = \frac{4\pi \sin\theta}{\lambda} \tag{3-2}$$

where θ and λ are the scattering angle and wavelength, respectively. It should be noted that Equation 3-3 holds within the ranges satisfying the requirements, $q^2\langle S^2\rangle_s \geq 1$ and $q^2 {S_c}^2 \leq 1$.[12] Figure 3-2 shows the SAXS profiles: $qI(q)$ is plotted against q^2 in a semi logarithmic scale according to Equation 3-1. The S_c values for **1a**, **1b**, and **1c** were calculated to be 3.6, 2.5, and 2.1 nm, respectively, from the slopes of the broken lines under the above-mentioned requirements. The diameters (d) of the bottlebrushes were determined as 10, 7.1, and 5.9 nm for **1a**, **1b**, and **1c**, respectively, using the following equation:

$${S_c}^2 = \frac{d^2}{8} \tag{3-3}$$

Note that this calculation is based on the assumption that the electron density of the cross-sections of cellulosic bottlebrushes **1a–c** is constant. In Figure 3-3, the estimated *d* values are plotted as a function of the degree of polymerization (*l*) of the side chain in a double logarithmic scale. All the data are larger than the counter length of main chain between two neighboring side chains *h* (= 0.52 nm / DS_{PSt}, plotted by open symbols in the figure), indicating that the side chains of **1a–c** are interacted each other and somehow stretched in the radical direction.

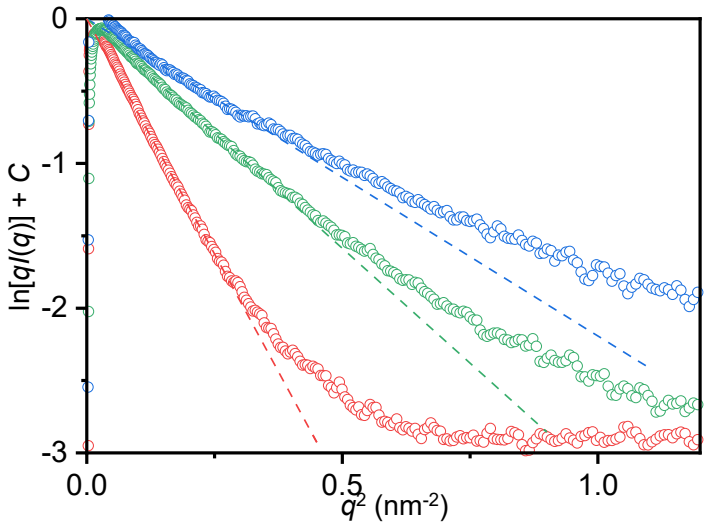

Figure 3-2. Cross-sectional Guinier plots for **1a** (blue circles), **1b** (green circles), and **1c** (red circles) in DMF/LiBr. The broken lines represent the Guinier approximations for the cross-sections of the corresponding samples.

Sheiko and coworkers performed a scaling analysis for the graft polymer with flexible side chains in poor solvent and presented the phase diagram of graft polymer in poor solvent as shown in Figure 3-4 (reproduced and modified with permission from Ref. 9). The horizontal axis indicates the scaled grafting density ($X = l^{1/2}h^{-1}$), and the vertical axis indicates the scaled distance from the Theta temperature ($Z = l^{1/2}|\tau|$, $\tau = T / T_\Theta - 1$: T_Θ is Θ temperature). In the region I and II, an isolated side chain takes a mushroom state and a collapsed globule state, respectively. In the region III, a bottlebrush forms a pearl-necklace structure. In the region IV and V, side chains form axially

uniform stretched and collapsed brush, respectively. In the region IV and V, the thickness of a bottlebrush scales as $d \cong l^{2/3}h^{-1/3}$ and $d \cong l^{1/2}(h|\tau|)^{-1/2}$, respectively. Figure 3-3 suggests that the d value follows a power law with an exponent of 0.50 ($d \cong l^{1/2}$). This means that **1a–c** takes not a pearl-neckless state but a collapsed brush as in the region V of Figure 3-4. This is consistent with the fact that DMF is a poor solvent for PSt and that the side chain is confined but somehow stretched by the interaction between neighboring side chains.

As far as the author knows, this is the first report experimentally showing that the diameter of bottlebrushes in a poor solvent follows a power law with an exponent of 0.5. This analysis on the side-chain conformations is also the key to the following advanced discussion on the main-chain stiffness and helicity of **2**.

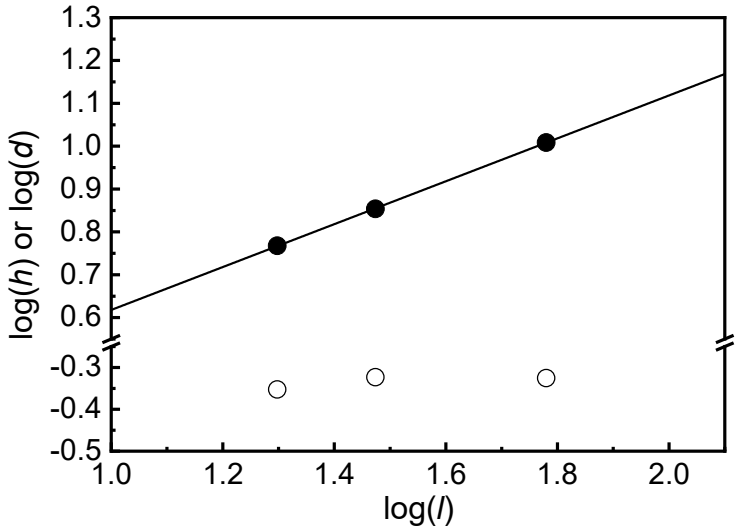

Figure 3-3. Counter length of main chain between two neighboring side chains (h) (open circle) and the dependence of diameter (d) on the degree of polymerization (DP) of the side chains for **1** in DMF/LiBr (closed circle). The line represents a power law fit of the data (parameters in Table 3-2).

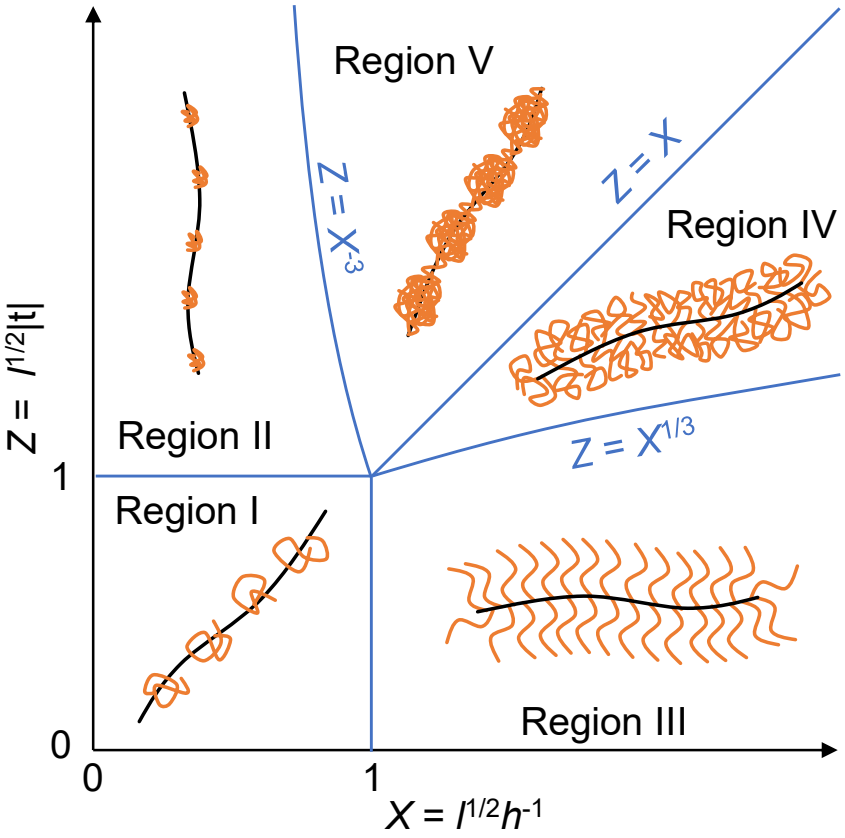

Figure 3-4. Phase diagram of graft polymer in poor solvent (Ref. 9).

3-3-2. Conformation of Main Chain.

The author carried out SEC-MALS measurements to determine the mean-square radius of gyration ($\langle S^2 \rangle$) as a function of molecular weight of the bottlebrush **1a–c** and to discuss the main-chain conformation. Figure 3-5 shows the SEC profiles as well as M_w and $\langle S^2 \rangle$ determined by MALS.

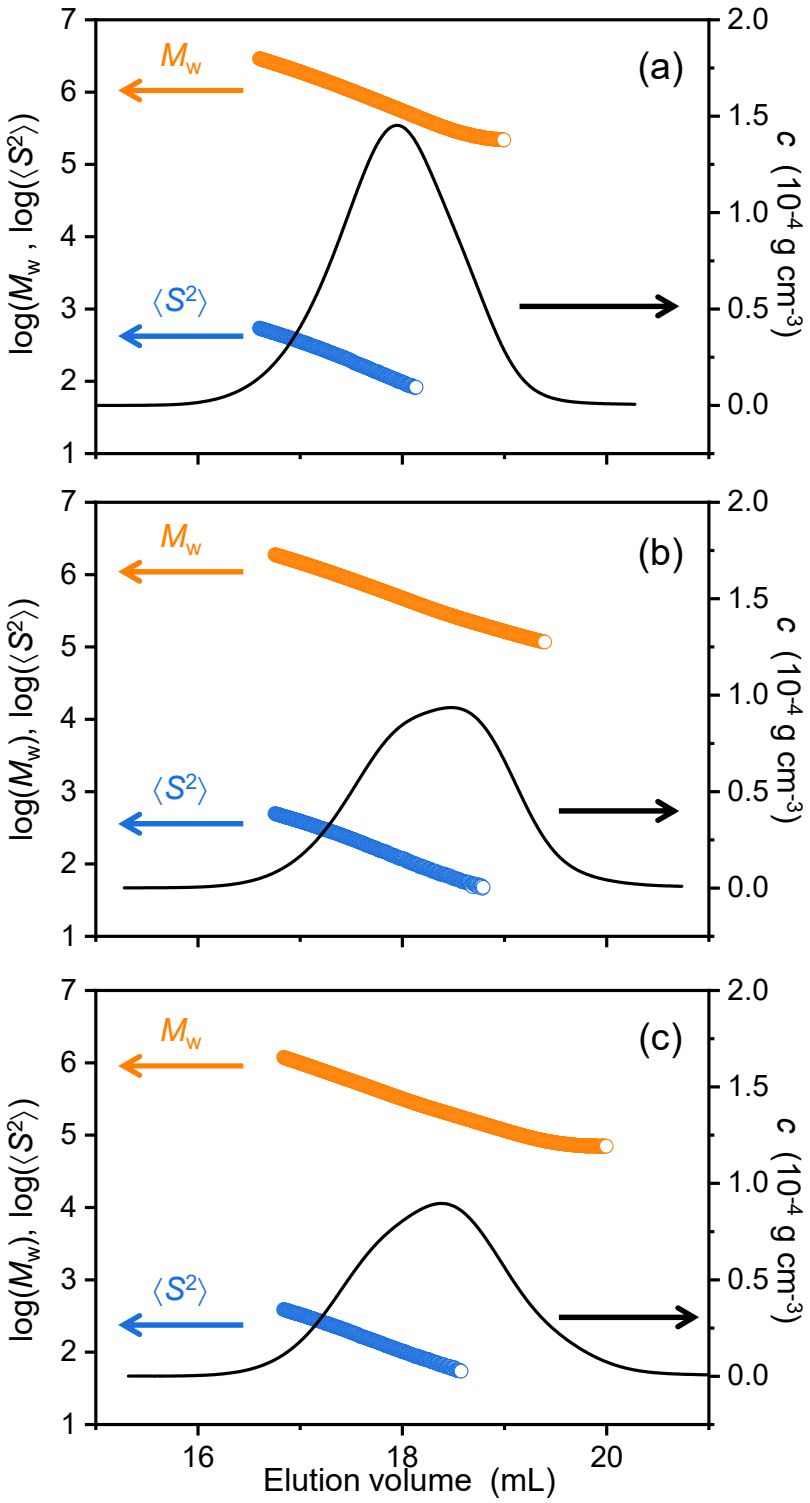
(a)
(b)
(c)
M_w
$\langle S^2 \rangle$
log(M_w , log($\langle S^2 \rangle$))
log(M_w), log($\langle S^2 \rangle$))
c (10^{-4} g cm^{-3})
Elution volume (mL)
16
18
20

Since the $\langle S^2 \rangle$ value determined by SEC-MALS contains $\langle S^2 \rangle_M$ and S_c^2, the $\langle S^2 \rangle_M$ value can be calculated using the following equation:[13]

$$\langle S^2 \rangle_M = \langle S^2 \rangle - {S_c}^2 \tag{3-4}$$

Figure 3-6 plots thus estimated $\langle S^2 \rangle_M$ value as a function of DP_w for **1a–c** in a double logarithmic scale, where DP_w represents the weight-average degree of polymerization of main chain and is calculated using the average molecular weight (M_0) per AGU including the side chains:

$$DP_{w,main} = \frac{M_w}{M_0} \tag{3-5}$$

Since a bottlebrush has a finite thickness, $\langle S^2 \rangle_M$ is giving by the following equation based on the KP chain model with a stiffness parameter, λ^{-1};

$$\langle S^2 \rangle_M = \frac{1}{\lambda^2}\left\{\frac{\lambda L}{6} - \frac{1}{4} + \frac{1}{4\lambda L} - \frac{1}{8\lambda^2 L^2}[1 - exp(-2\lambda L)]\right\} \tag{3-6}$$

where L represent the contour length of main chain. For the L value, the side chains near both ends of the main chain should be taken into account as a correction value equivalent to the cross-sectional diameter d of the bottlebrush (as shown in Figure 3-1b). Thus, L is calculated by the following equation:

$$L = \frac{M_w}{M_L} + d \tag{3-7}$$

where M_L is the molecular weight per unit contour length.

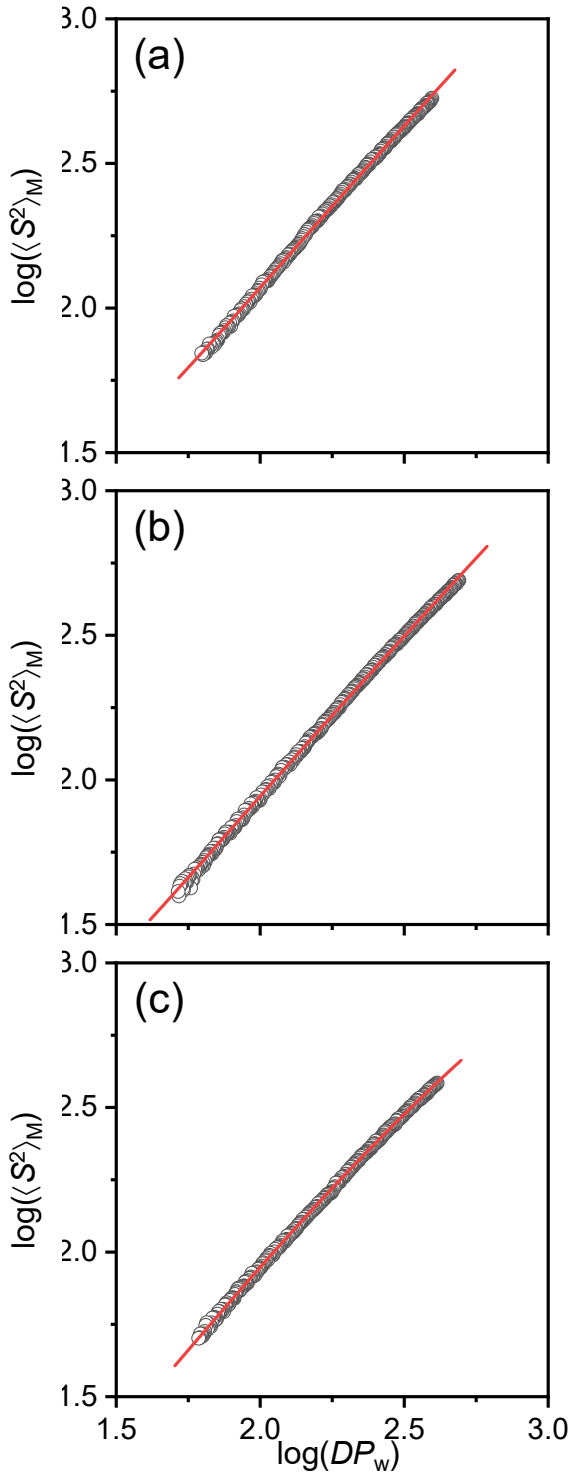

Figure 3-6. DP_w dependence of $\langle S^2 \rangle_M$ for (a) **1a**, (b) **1b**, and (c) **1c** in DMF/LiBr (black circles). The red curves represent the theoretical values calculated for the perturbed KP chain model (parameters in Table 3-2).

For estimating the M_L, the author assumed that the ratio of M_0 to M_L, corresponding to the contour length per repeating unit, is equal to the length of AGU along the long axis of cellulose crystal (0.52 nm)[14] using the following equation,

$$\left(\frac{M_0}{M_L}\right)_{\mathbf{1}} = 0.52\ (\mathrm{nm}) \tag{3-8}$$

The red curves in Figure 3-6 are the theoretical values determined from the KP chain model using Equation 3-6 with the parameters M_L and λ^{-1} (listed in Table 3-2), which well reproduced the experimental data. Figure 3-7 shows the plots of DP_w vs $\langle S^2\rangle_M/ DP_w$ for the experimental and theoretical data in order to discuss the validity of the KP chain model and the accuracy of the determined λ^{-1} value: the theoretical data are calculated with the determined λ^{-1} value and the λ^{-1} ± 1 values. Obviously, the theoretical curves with the determined λ^{-1} value better reconstructed the experimental data. Thus, the author concluded that the KP chain model could well describe the conformation of main chain of **1** and reasonably precisely estimate the λ^{-1} value in the range of molecular weights analyzed.

Table 3-2. Results of SAXS and SEC-MALS measurements for cellulosic bottlebrushes **1**.

sample	SAXS		SEC–MALS	
	S_c (nm)	d (nm)	M_L ($\times 10^4$ nm^{-1})	λ^{-1} (nm)
1a	3.6	10	1.4	17
1b	2.5	7.1	7.4	12
1c	2.1	5.9	5.5	12

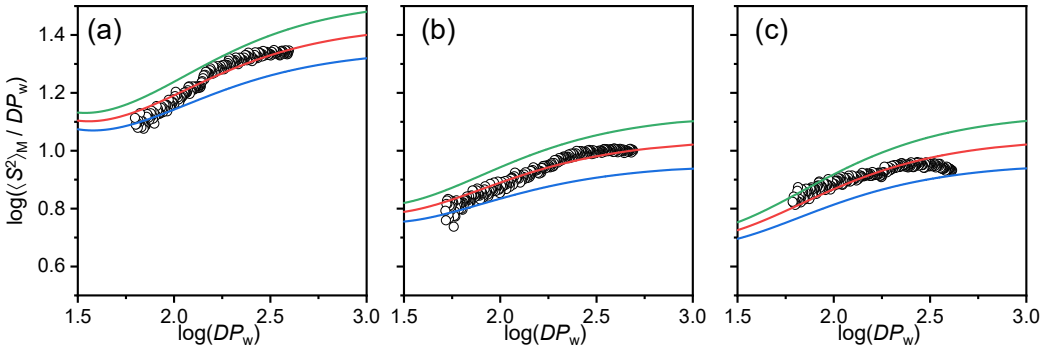

Figure 3-7. The dependence of $\log(\langle S^2\rangle_M / DP_w)$ on $\log(DP_w)$ for (a) **1a**, (b) **1b**, and (c)**1c**. The red curves represent the theoretical value of the unperturbed KP chain model with the determined λ^{-1} values listed in Table 3-2, whereas the blue and yellow curves represent the theoretical value of the KP chain model with the determined λ^{-1} values plus 1 and minus 1, respectively.

Finally, the λ^{-1} value was reasonably estimated to be 17, 12, and 12 nm for **1a–c**, respectively. Off course, these values are much larger than those of common vinyl polymers such as PMMA and PSt. Interestingly, these values are comparable to those of (non-substituted) cellulose (λ^{-1} = 7 nm in 3-butyl-1-methylimidazolium chloride (BMIC)[15] and 18 nm in *N*,*N*-dimethylacetamide (DMAc)/LiCl[16] and its derivatives including cellulose triacetate (λ^{-1} = 14 nm in DMAc),[17] cellulose tristearate (λ^{-1} = 25 nm in THF),[18] and cellulose tris(phenylcarbamate) (λ^{-1} = 21 nm in THF).[19] In general, the main chain of a bottlebrush may be stiffened by the side chains radically stretched owing to their excluded volume effects, but this is not the case with the cellulosic bottlebrushes **1a–c**.

Nakamura and coworkers experimentally showed that a bottlebrush of PSt as both main and side chains (PSt-PSt bottlebrushes) become stiffer with increasing molecular weight of the side chain in a Θ-solvent as well as in a good solvent (open circles in Figure 3-8).[2-4, 20] Additionally, they theoretically derived the following equation using the first order perturbation theory:[21]

$$\lambda^{-1} = {\lambda_0}^{-1} + {\lambda_b}^{-1} \tag{3-9}$$

where λ_0^{-1} is the contribution due to the internal rotation sterically hindered by the side chain near the main chain and λ_b^{-1} is the one derived from the excluded-volume interactions among side chains. On the assumption that the conformation of the side chains takes the Gaussian model, λ_b^{-1} of a bottlebrush in a Θ-solvent is represented as follows:[21]

$${\lambda_b}^{-1} = 0.02334\left(\frac{l}{b}\right)^2\left(\frac{\beta_3}{h^3}\right) \tag{3-10}$$

where h, b and β_3 represent contour length of the main chain per side chain, effective bond length of each side chain, and ternary cluster integral, respectively. The theoretical curve (a solid curve in Figure 3-8) is calculated using Equation 3-9 and 3-10 with h = 0.27 nm for the PSt-PSt bottlebrush. As shown in Figure 3-8(a), the theoretical curve obtained with the parameters listed in Table 3-3 well reproduces the experimental data (plotted by open symbols) and clearly shows that the main chain of a bottlebrush become stiffer as the side chain become longer.

Based on this consideration, one can directly compare the results of the cellulosic bottlebrushes with those of the PSt-PSt one, even though their side-chain density is different. Figure 3-8(b) shows the l dependency of λ^{-1}; the closed symbols are the experimental data for the cellulosic bottlebrushes, the solid curve is the theoretical data calculated for the hypothetic PSt-PSt bottlebrush with the model parameters listed in Table 3-3 including h = 0.52 nm (the same as the cellulosic bottlebrushes), and the dotted curves indicates the already mentioned λ^{-1} values for (non-substituted) cellulose. It should be noted that the λ^{-1} values of the cellulosic bottlebrushes are larger and less dependent on the side-chain length as compared with those for the hypothetic PSt-PSt bottlebrushes. This can be ascribed to different contribution to the main-chain stiffness. Figure 3-8(b) can be understood to suggest the crossover in the origin of main-chain stiffness of the cellulosic bottlebrush as a function of side-chain length in a Θ-solvent (even in a poor solvent).

In the region of side-chain length sufficiently small, the main-chain stiffness is dominated by the intrinsic stiffness of cellulose chain and hence remains constant independent of the side-chain length. With increasing side-chain length, the excluded-volume interaction between neighboring side chains increases and hence the main-chain stiffness increases via the crossover region. It should be noted that the cross-over side-chain length was roughly estimated to be 60 in *l* (equivalent molecular weight, 6000), which is so high as to understand that the grafting-to approach to synthesize the bottlebrushes proceeds in a controlled fashion.

Table 3-3. Model parameters of the first order perturbation theory for PSt-PSt bottlebrush and hypothetic PSt-PSt bottlebrush.

sample	λ_0^{-1} *(nm)*	*h* (nm)	*b* (nm)	β_3 ($\times 10^{-3}$ nm^6)
PSt-PSt bottlebrush	8	0.27	0.74	4
hypothetic PSt-PSt bottlebrush	8	0.52	0.74	4

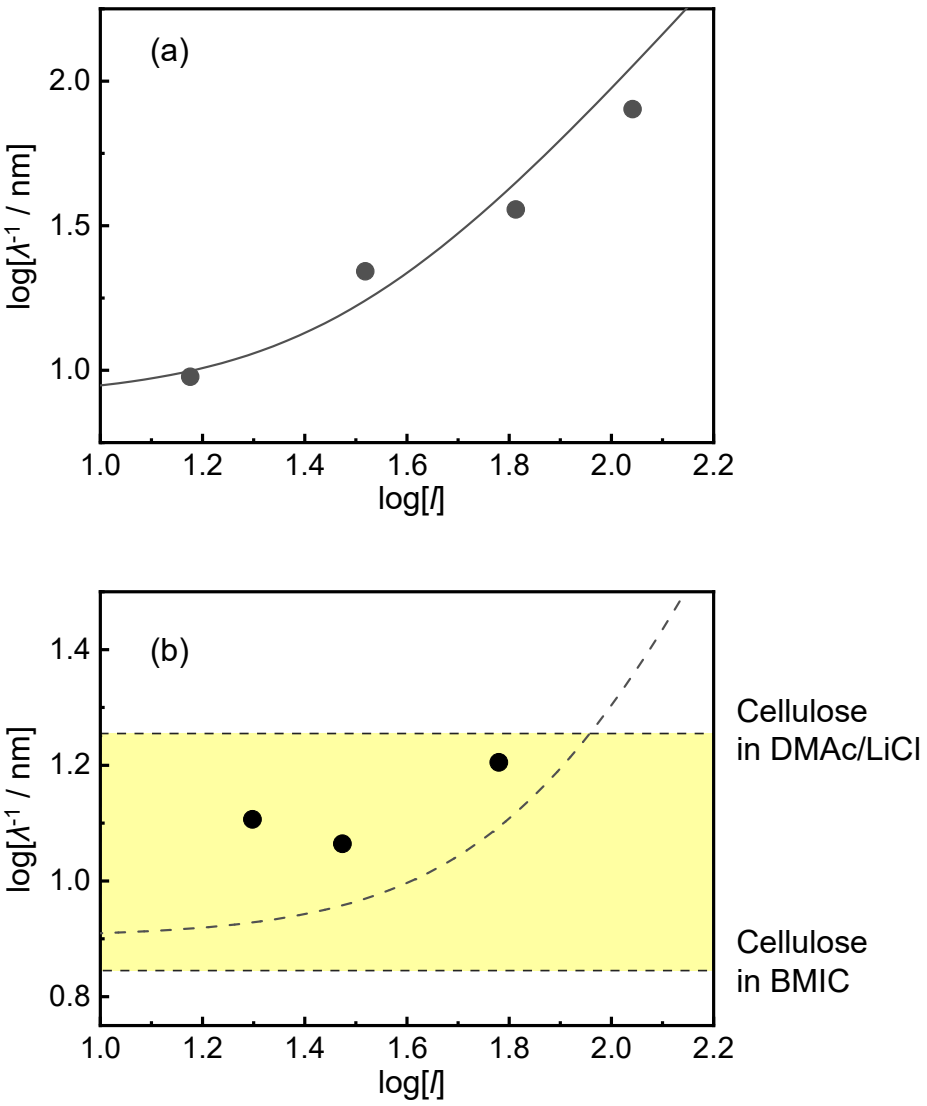

Figure 3-8. (a) The dependence of λ^{-1} on the degree of polymerization (l) of the side chains for PSt-PSt bottlebrush in a Θ-solvent. the solid lines represents the theoretical curve for the PSt-PSt bottlebrush calculated with h = 0.27 nm; (b) The dependence of λ^{-1} on the degree of polymerization (l) of the cellulosic bottlebrush **1** in a poor solvent. The broken curve represents the theoretical curve for the PSt-PSt bottlebrush calculated with h = 0.52 nm in a Θ-solvent.

3-4. Conclusion

The author has fully characterized a cellulosic bottlebrush with one PSt-side chain every AGU by SEC-MALS and SAXS measurements and reveal the conformation of side and main chains in DMF/LiBr, which is a poor solvent for PSt. Their conformations in dilute solution were characterized by the value of $\langle S_c^2 \rangle$ and the dependence of $\langle S^2 \rangle$ on the *DP* of the main chain. The diameter *d* of the cellulosic bottlebrushes (associated with $\langle S_c^2 \rangle$) was larger than the contour length of main chain per side chain and followed a power law with an exponent of 0.50. These results suggested that the side chains are confined in a poor solvent but somewhat extended in the radial direction. The main-chain conformation of cellulosic bottlebrushes was well reproduced with the KP chain model, successfully estimating the stiffness parameter λ^{-1}. The determined stiffness of main chain of bottlebrush was almost independent of the *DP* of the PSt side chains and comparable to that of cellulose and its derivatives with small substituents. This means that the excluded-volume effect among neighboring side chains was too small to affect the main-chain conformation of the cellulosic bottlebrush in a studied range of molecular weight of side chain. Furthermore, the *l* dependency of λ^{-1} value was evaluated for the hypothetic bottlebrushes of flexible main and side chains (PSt-PSt bottlebrushes) assuming the same side-chain density to those of the studied cellulosic bottlebrushes. This clarify the crossover in the origin of the main-chain stiffness from the intrinsic character to the effect of excluded-volume interaction between side chains with increasing side-chain length. Below 6000 in PSt molecular weight, the intrinsic stiffness of semi-flexible cellulose plays an important role to keep the main-chain conformation of bottlebrushes even when the attractive interaction works among side chains with a compact conformation in a poor solvent. The author also expects that a cellulosic bottlebrush may keep an originally equipped chain character, e.g., main-chain helicity, hence exhibiting fascinating structure and properties in the side-chain length up to the PSt molecular weight as high as 6000.

3-5. Acknowledgment

The synchrotron SAXS experiments were performed at BL40B2 (Proposal Nos. 2016B1208 and 2017B1727) in SPring-8 with the approval of the Japan Synchrotron Radiation Research Institute (JASRI). The authors thank Dr. Noboru Ohta (JASRI/SPring-8) for assistance in the experiments on the BL40B2 beamline.

3-6. References

1. Benoit, H.; Doty, P. Light Scattering from Non-Gaussian Chains. *J. Phys. Chem.* **1953**, *57*, 958-963.
2. Terao, K.; Nakamura, Y.; Norisuye, T. Solution Properties of Polymacromonomers Consisting of Polystyrene. 2. Chain Dimensions and Stiffness in Cyclohexane and Toluene. *Macromolecules* **1999**, *32*, 711-716.
3. Hokajo, T.; Terao, K.; Nakamura, Y.; Norisuye, T. Solution Properties of Polymacromonomers Consisting of Polystyrene V. Effect of Side Chain Length on Chain Stiffness. *Polym. J.* **2001**, *33*, 481-485.
4. Sugiyama, M.; Nakamura, Y.; Norisuye, T. Dilute-Solution Properties of Polystyrene Polymacromonomer Having Side Chains of over 100 Monomeric Units. *Polym. J.* **2007**, *40*, 109-115.
5. Hatanaka, Y.; Nakamura, Y. Dilute Solution Properties of Polymacromonomer Consisting of Polybutadiene Backbone and Polystyrene Side Chains. *Polymer* **2013**, *54*, 1538-1542.
6. Klemm, D.; Heublein, B.; Fink, H. P.; Bohn, A. Cellulose: Fascinating Biopolymer and Sustainable Raw Material. *Angew. Chem., Int. Ed. Engl.* **2005**, *44*, 3358-3393.
7. Gray, D. G. Chemical Characteristics of Cellulosic Liquid Crystals. *Faraday Discuss. Chem. Soc.* **1985**, *79*, 257-264.
8. Ikai, T.; Okamoto, Y. Structure Control of Polysaccharide Derivatives for Efficient Separation of Enantiomers by Chromatography. *Chem. Rev.* **2009**, *109*, 6077-6101.
9. Sheiko, S. S.; Borisov, O. V.; Prokhorova, S. A.; Moller, M. Cylindrical Molecular Brushes under Poor Solvent Conditions: Microscopic Observation and Scaling Analysis. *Eur. Phys. J. E.* **2004**, *13*, 125-131.
10. Benoit, H.; Froelich, D. Application of Light Scattering to Copolymers. In *Light Scattering from Polymer Solutions*, Huglin, M. B., Ed. Academic Press: London and New York, 1972; pp 467-501.

11. Glatter, O.; Kratky, O. *Small Angle X-ray Scattering*. Academic Press: London, 1982.
12. Wataoka, I.; Kobayashi, K.; Kajiwara, K. Effect of the Carbohydrate Side-Chain on the Conformation of a Glycoconjugate Polystyrene in Aqueous Solution. *Carbohydr. Res.* **2005**, *340*, 989-995.
13. Yamakawa, H.; Yoshizaki, T. *Helical Wormlike Chains in Polymer Solutions*. 2nd ed.; Springer, Berlin Heidelberg: Berlin, 2016.
14. Sugiyama, J.; Vuong, R.; Chanzy, H. Electron Diffraction Study on the Two Crystalline Phases Occurring in Native Cellulose from an Algal Cell Wall. *Macromolecules* **1991**, *24*, 4168-4175.
15. Jiang, X.; Kitamura, S.; Sato, T.; Terao, K. Chain Dimensions and Stiffness of Cellulosic and Amylosic Chains in an Ionic Liquid: Cellulose, Amylose, and an Amylose Carbamate in BmimCl. *Macromolecules* **2017**, *50*, 3979-3984.
16. Yanagisawa, M.; Isogai, A. SEC-MALS-QELS Study on the Molecular Conformation of Cellulose in LiCl/Amide Solutions. *Biomacromolecules* **2005**, *6*, 1258-1265.
17. Kawanishi, H.; Tsunashima, Y.; Okada, S.; Horii, F. Change in Chain Stiffness in Viscometric and Ultracentrifugal Fields: Cellulose Diacetate in N, N-Dimethylacetamide Dilute Solution. *J. Chem. Phys.* **1998**, *108*, 6014-6025.
18. Yoshida, Y.; Isogai, A. Preparation and Characterization of Cellulose β-ketoesters Prepared by Homogeneous Reaction with Alkylketene Dimers: Comparison with Cellulose/Fatty Acid Esters. *Cellulose* **2007**, *14*, 481-488.
19. Kasabo, F.; Kanematsu, T.; Nakagawa, T.; Sato, T.; Teramoto, A. Solution Properties of Cellulose Tris(phenyl carbamate). 1. Characterization of the Conformation and Intermolecular Interaction. *Macromolecules* **2000**, *33*, 2748-2756.
20. Terao, K.; Takeo, Y.; Tazaki, M.; Nakamura, Y.; Norisuye, T. Polymacromonomer Consisting of Polystyrene. Light Scattering Characterization in Cyclohexane. *Polym. J.* **1999**, *31*, 193-198.
21. Nakamura, Y.; Norisuye, T. Backbone Stiffness of Comb-Branched Polymers. *Polym. J.* **2001**, *33*, 874-878.

Chapter 4

Intramolecular Phase Separation of Janus Cellulosic Bottlebrushes in Solution

4-1. introduction

Recent advance in precise polymer synthesis brings a new type of bottlebrushes possessing different kinds of side chains (hetero bottlebrush). Among them, the bottlebrush which have the structure like different bottlebrushes connected in series, is called block bottlebrush.[1] On the contrary, the bottlebrushes possessing immiscible side chains uniformly along the main chain is called Janus-type bottlebrush.[2,3] Janus bottlebrush could act surfactant with low critical micelle concentration because of its large cross-sectional area to contact solvent.[4,5] Meanwhile, Janus bottlebrush self-assembles into micelle[6] or vesicles[7,8] in solution, of which shapes are influenced by the curvature of Janus bottlebrushes. The distinct feature for Janus bottlebrush is that the intramolecular phase separation contributes to low entropy loss in forming bulk microphase separation. Janus bottlebrush could form microphase separation with smaller domain pitch than diblock copolymers with the same chemical composition.[9,10] Additionally, the stiffened main chain enables to reduce entanglement, leading rapid progression of microphase separation. Thus, it is important to figure out the intramolecular phase separation of isolated Janus bottlebrush.

Up to now, the second structure of Janus bottlebrush in solution has been theoretically[11] and computationally[12-14] studied. As for Janus bottlebrush with rigid main chain it was reported that the lower the affinity between solvent and side chains is, the more the intramolecular phase separation proceeds (i) (Figure 4-1a).[12] Additionally, in poor solvent for side chains, it was showed that the Janus bottlebrush with stiff main chain and low-dense side chains takes pearl-necklace structure (ii) (Figure 4-1b),[13] and that the Janus bottlebrush with flexible main chain forms

intramolecular spherical aggregation (iii) (Figure 4-1c).[14] However, experimental study for the second structure of Janus bottlebrush has not been sufficiently explored. Therefore, in this chapter, the author aimed to observe the microphase separation of isolated Janus bottlebrush in solution.

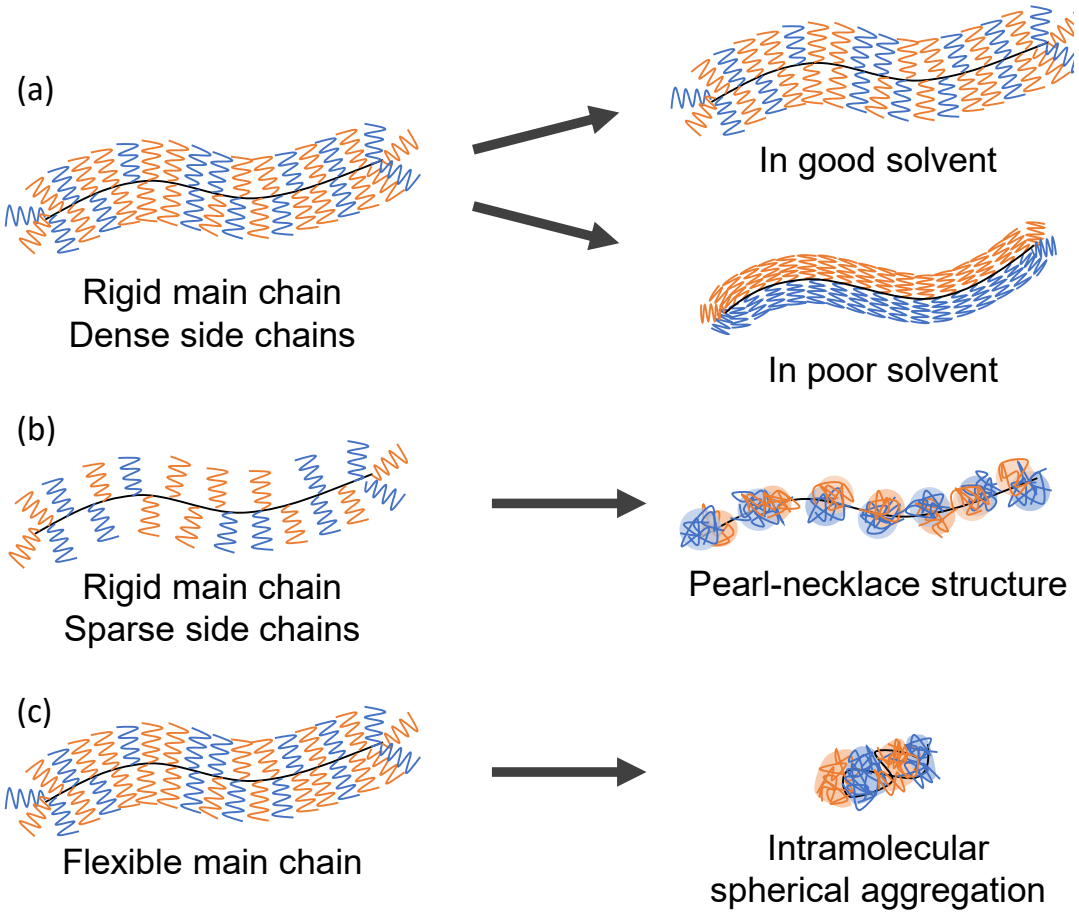

Figure 4-1. Schematic illustration of the second structure of Janus bottlebrushes with rigid man chain and dense side chains (a), rigid main chain and sparse side chains (b), and flexible main chain (c).

In this study, the author planned to prepare a Janus bottlebrush with dense side chain

and stiff main chain as a model shown in Figure 4-1a, and then to figure out the conformation in poor solvent by scattering experiment. The author thinks that cellulose is the best main chain as the model Janus bottlebrushes, since cellulose is semi-flexible with three hydroxyl groups in anhydroglucose unit (AGU), to which different side chains can be densely introduced.[15] The author previously revealed that the cellulosic homo bottlebrushes possessing polystyrene (PSt) side chains (*DP* = 20, 30 and 60) at *O*-6 position with high density (PSt-cellulose) formed cylindrical conformation in poor solvent for PSt chains (DMF). Based on that, in this section, the author analyzed cross-sectional microphase separated structure of PEO-PSt-cellulose. SAXS measurement for PEO-PSt-cellulose and PSt-cellulose were carried out in DMF/LiBr to determine the cross-sectional radius of gyration ($S_{c,SAXS}$) via the cross-sectional Guinier plots. Cross-sectional microphase-separation structure was determined by comparing the dependency of $S_{c,\,SAXS}$ for PEO-PSt-cellulose and PSt-cellulose on molecular weight of PSt per AGU and the cross-sectional model. Then, SEC-MALS measurement for PEO-PSt-cellulose was carried out to obtain the dependency of the mean square radius of gyration $\langle S^2 \rangle$ on the degree of polymerization in order to confirm the conformation in solution. These results show that PEO-PSt-cellulose formed the cylindrical structure with intramolecular phase separation along their main chain.

4-2. Experimental Section

4-2-1. Samples.

The cellulosic Janus (PEO-PSt-cellulose **2**, Figure 4-2) and homo bottlebrushes (PSt-cellulose **1** and PEO-cellulose **9,** Figure 4-2) were used. DMF with LiBr (DMF/LiBr) at the concentration of 10 mM was used as the solvent throughout this study. Their molecular characteristics are listed in Table 4-1.

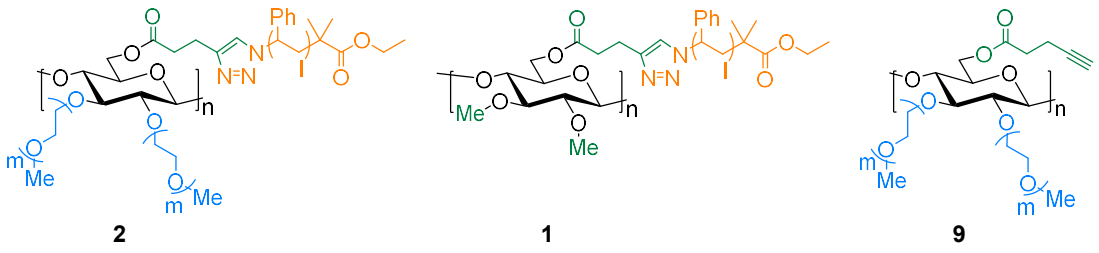

Figure 4-2. Chemical structure of PEO-PSt-cellulose **2**, PSt-cellulose **1** and PEO-cellulose **9.**

Table 4-1. Characteristics of cellulosic bottlebrushes **2a–c**, **1a–c** and **9**.

		sample	DS_{PEO}	DS_{PSt}	$M_{n,PSt}$ (g/mol)	M_0 (g/mol)	$w_{backbone}$[a]	w_{PEO}[a]	w_{PSt}[a]	dn/dc[b] (mL/g)	M_w[c] (g/mol)	$DP_{w,main}$[c]	M_w/M_n[c]	$S_{c,SAXS}$[2] (nm^2)
Janus	PEO-PSt-cellulose	**2a**	1.6	1.0	6.4×10^3	8.1×10^3	0.03	0.14	0.83	0.139	9.7×10^5	1.2×10^2	2.3	12
		2b	1.6	1.0	3.3×10^3	4.7×10^3	0.05	0.24	0.71	0.126	6.1×10^5	1.3×10^2	2.4	5.4
		2c	1.6	1.1	2.2×10^3	3.8×10^3	0.06	0.31	0.63	0.117	4.8×10^5	1.3×10^2	2.4	3.6
Homo	PSt-cellulose	**1a**	—	1.1	6.4×10^3	7.4×10^3	0.04	—	0.96	0.154	8.1×10^5	1.1×10^2	1.6	13
		1b	—	1.1	3.3×10^3	3.8×10^3	0.07	—	0.93	0.150	4.6×10^5	1.2×10^2	1.7	6.4
		1c	—	1.2	2.2×10^3	2.9×10^3	0.10	—	0.90	0.148	3.2×10^5	1.1×10^2	1.7	4.3
	PEO-cellulose	**9**	1.6	—	—	1.4×10^3	—	—	—	—	6.2×10^4[d]	4.4×10[d]	1.5[d]	1.8

[a]Weight fraction of the main chain and PSt chains. [b]Refractive index increment calculated from Equation 2-1 and 2-2. [c]Determined by SEC-MALS in DMF/LiBr. [d]Dtermined by SEC with PMMA standard.

4-2-2. Instrumentation and Measurements.

SAXS measurements were carried out at room temperature using BL40B2 at SPring-8 (Hyogo, Japan). Each SAXS profile was obtained using an imaging plate (RIGAKU R-AXIS VII) with a frame size of 3000 × 3000 pixels and a pixel size of 100 × 100 μm^2. The X-ray wavelength was 1.000 Å. The camera length was calibrated to be 1654 mm using the diffraction peaks of silver behenate. The excess scattering intensity $I(q)$ was obtained as the difference of scattering intensity between the solution and the pure solvent. Each solution of bottlebrushes at a concentration of 0.5 w/v% in DMF/LiBr was introduced into a flat cell (width, 3 mm) equipped with a pair of thin quartz glass windows (thickness, 20 μm).

SEC-MALS analysis was carried out using a DAWN HELEOS instrument (Wyatt Technology Corp., Santa Barbara, CA, USA, λ = 658 nm) at room temperature (for MALS) combined with Shodex GPC-101 system (for SEC), which was equipped with a KF-G (Shodex) guard column, two KF-806L (Shodex) columns, and an RI-71S differential refractometer (Shodex). DMF with LiBr (10 mM) was used as the eluent. To determine the weight-average molecular weight M_w, the mean-square radius of gyration $\langle S^2 \rangle$, and polydispersity index M_w/M_n with MALS, the Berry plot was used. The refractive index increment (dn/dc) of **1a–c** and **2a–c** was calculated using equation 2-2 in chapter 2.

4-2. Results and Discussion

4-2-1. Cross-Sectional Structure of Bottlebrushes

4-2-1-1. Comparison of the Cross-Sectional Radius of Gyration Values between Janus bottlebrush PEO-PSt-cellulose and Homo Bottlebrush PSt-cellulose and PEO-cellulose

To determine the cross-sectional radius of gyration (S_c) values for bottlebrushes, SAXS measurements for PEO-PSt-cellulose (**2a–c**), PSt-cellulose (**1a–c**) and PEO-cellulose (**9**) in DMF/LiBr were carried out. Figure 4-3 shows the cross-sectional Guinier plots of $\ln[qI(q)]$ versus q^2 for SAXS profile, where $\boldsymbol{q}$ and $I(q)$ are the scattering vector and scattering intensity, respectively. q is defined by following equation:

$$q = \frac{4\pi \sin\theta}{\lambda} \tag{4-1}$$

where 2θ and λ are the scattering angle and wavelength, respectively. Assuming that the bottlebrush takes a rod-like conformation, the S_c values determined by SAXS ($S_{c,SAXS}$) is described by the following equation in the range of $q^2\langle S^2\rangle \geq 1$ and $q^2 S_{c,SAXS}{}^2 \leq 1$: [16,17]

$$\ln[qI(q)] = A - \frac{1}{2} S_{c,SAXS}{}^2 q^2 \tag{4-2}$$

where A represents the constant factor.

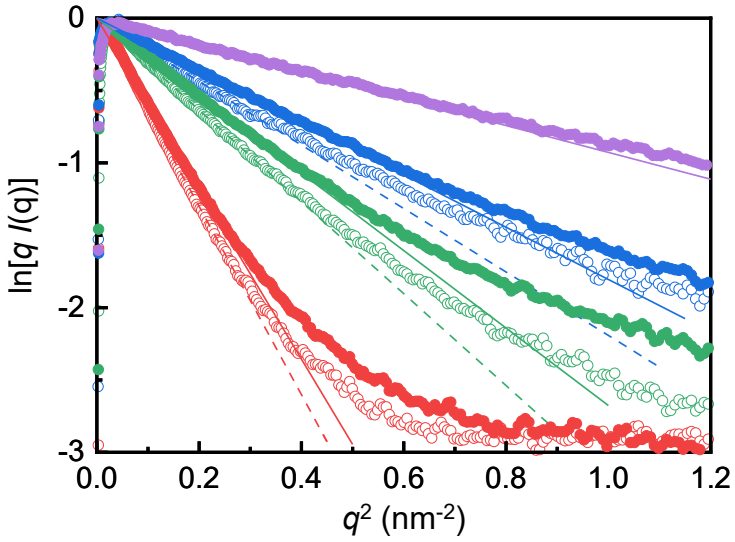

Figure 4-3. Cross-sectional Guinier plots for bottlebrushes; **2a, 2b** and **2c** (red, green and blue closed circles); **1a, 1b** and **1c** (red, green and blue open circles); **9** (purple closed open circle). The solid and broken lines represent the increment of cross-sectional Guinier approximation for **1, 2** and **9** respectively.

The $S_{c,SAXS}$ values are determined from the slope of the broken line in Figure 4-3. In chapter 3, it was revealed that the bottlebrush **1** was in "collapsed brush" state in DMF, and the density of side chains domain was constant. Thus, assuming that the bottlebrushes **2** have each constant electron density across the cylinder, the radius of the bottlebrushes (R_{ce}) were calculated from the following equation:

$$S_{c,SAXS}{}^2 = \frac{R_{ce}{}^2}{2} \tag{4-3}$$

Table 4-2 shows that the R_{ce} values calculated with equation 4-3. PEO-PSt-cellulose had smaller R_{ce} values than PSt-cellulose with same molecular weight of PSt side chains, which was discrepant to the fact that PEO-PSt-cellulose had larger molecular weight per AGU (M_0). This means that the R value did not reflect the actual thickness of bottlebrushes. The author considers that this is because the assumption that bottlebrushes had a constant electron density across the cylinder is

not adequate. Following discussion shows the bottlebrush having shell with inhomogeneous electron density across the cylinder.

Table 4-2. Cross-sectional Guinier approximation for **1a-c** and **2a-c** and **6** in DMF. The broken lines represent the Guinier approximation for cross-section of the corresponding samples.

	Janus			Homo			
	2a	**2b**	**2c**	**1a**	**1b**	**1c**	**9**
R_{ce} (nm)	4.9	3.3	2.7	5.1	3.6	2.9	1.9

4-2-1-2. Core-(Homo-Shell) Model with Homogeneous Shell

In this core-shell model (Figure 4-3), the main chain of bottlebrush, cellulose, forms the core and swollen PEO and PSt side chains do not undergo microphase separation to form homogeneous shell with constant electron density (core-(homo-shell) model). In order to adopt this model to PEO-PSt-cellulose, the density of the core occupied by cellulose ($d_{celllose}$) was determined by analyzing the dependency of $S_{c,SAXS}^2$ on the molecular weight of PSt side chain per AGU ($MW_{AGU,PSt}$) in PSt-cellulose **1a-c** with core-shell model. As a result, the experimental data are reproduced well by the theoretical curve in this model with fitting parameters ($d_{celllose}$ = 1.17 g/cm^3 and the density of swollen PSt ($d_{PSt,solvent}$) = 0.26 g/cm^3) (Figure 4-4). Then, the author calculated the radius of PEO-cellulose and PEO-PSt-cellulose on assumption that PEO-cellulose and PEO-PSt-cellulose have same $d_{celllose}$ value as that of PSt-cellulose. Table 4-3 shows the radius of core-(homo-shell) model (R_{chs}) and the density of swollen PEO ($d_{PEO,solvent}$) and $d_{PSt,solvent}$. It is expected that PEO-PSt-cellulose have smaller $d_{PSt,solvent}$ than PSt-cellulose because PEO side chains are coexistent with PSt side chains in the shell of PEO-PSt-cellulose. However, the calculated $d_{PSt,solvent}$ values for PEO-PSt-cellulose with equation 4-3 had larger values than PSt-cellulose. Consequently, the author concluded that this model was inappropriate to PEO-PSt-

cellulose and that PEO and PSt side chains underwent intramolecular phase separation.

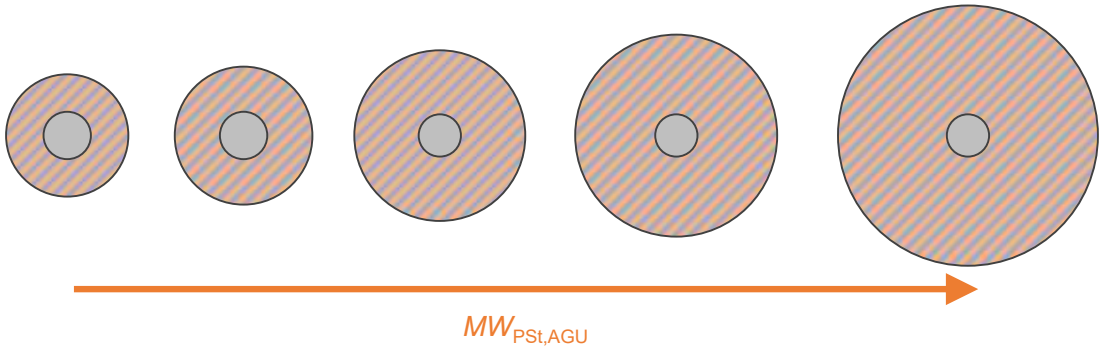

Figure 4-3. Schematic illustration of core-(homo-shell) model for a Janus bottlebrush.

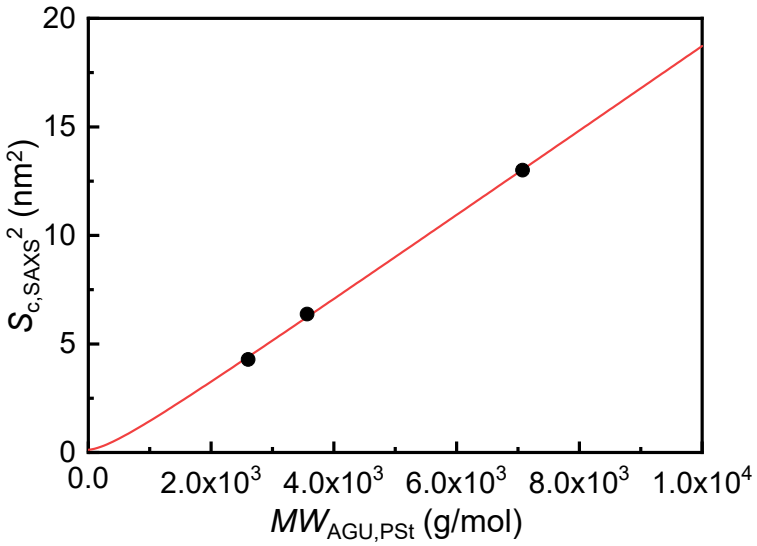

Figure 4-4. The relation between $S_{c,SAXS}^2$ and $MW_{AGU,PSt}$ for PSt-cellulose (**1a-c**). The red curves represent the theoretical curve of core-shell model ($d_{celllose}$ = 1.17 g/cm^3 and $d_{PSt,solven}$ = 0.26 g/cm^3).

Table 4-3. Results of analysis of PEO-cellulose and PEO-PSt-cellulose with core-(homo-shell) model.

	2a	**2b**	**2c**	**9**
$MW_{PEO,AGU}$ (g/mol)	1.1×10^3	1.1×10^3	1.1×10^3	1.1×10^3
$MW_{PSt,AGU}$ (g/mol)	6.7×10^3	4.7×10^3	2.4×10^3	—
R_{chs} (nm)	5.0	3.4	2.8	2.1
$d_{PEO,solvent}$ (g/cm^3)	0.048	0.10	0.15	0.29
$d_{PSt,solvent}$ (g/cm^3)[a]	0.28	0.30	0.32	—

[a] the $d_{PSt,solvent}$ for **2** is 0.26 g/cm^3.

4-2-1-3. Core-Shell Model with Heterogeneous Shell

The author considered following 4 models for cross-sectional structure of Janus bottlebrushes (Figure 4-5).

- Core-(core-shell) model I

  Core consisting of cellulose is wrapped by swollen PSt and PEO domains in this order

- Core-(core-shell) model II

  Core consisting of cellulose is wrapped by swollen PEO and PSt domains in this order

- Core-Janus model I

  Core consisting of cellulose is wrapped by Janus shell with swollen PEO and PSt domain. When the gap between the swollen PEO and PSt domain size is big, the Janus shell takes core-shell like form.

- Core-Janus model II

  Core consisting of cellulose is wrapped by Janus shell with swollen PEO and PSt domain. Even if gap between the swollen PEO and PSt domain size is big, the domains take fan shape.

In above 4 models, the structural model parameters in Figure 4-12 depend only the cross-sectional

area of main chain (cellulose derivative), PSt and PEO domains. The density of PSt and PEO domains are inversely proportional to their swelling ratio (the cross-sectional area). Assuming that the cross-sectional area of each domains in homo and Janus bottlebrush (**1a–c**, **9**, **2a–c**) is directly proportional to molecular weight per AGU (MW_0), the author determined the $d_{PEO,solvent}$ value.

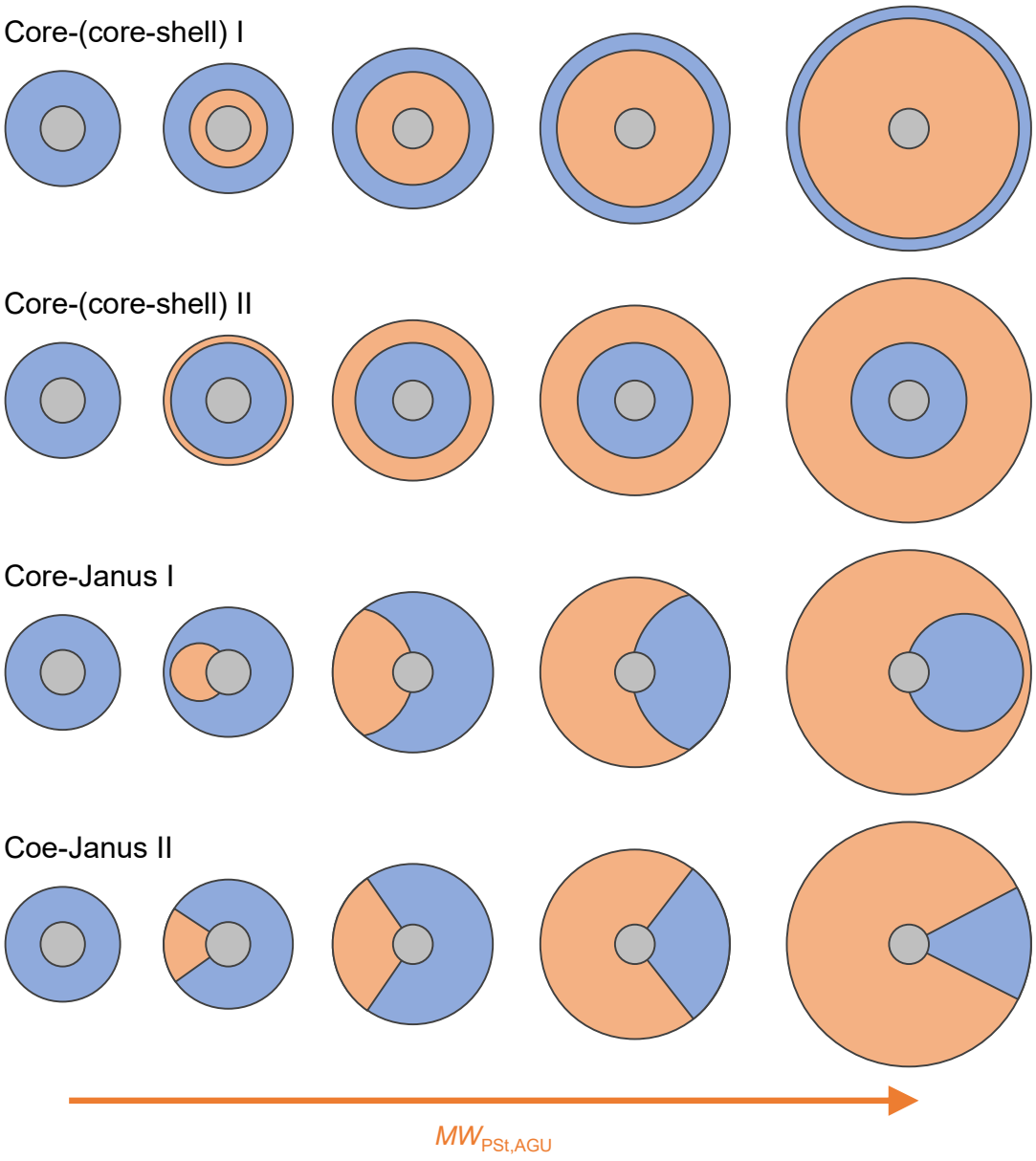

Figure 4-5. Cross-sectional structure of core-(core-shell) model I and II, and core-Janus I and II. Gray: cellulosic backbone; blue: PEO regions; orange: PS regions.

4-2-1-3-1. Core-Shell Model with Heterogeneous Shell

Figure 4-6 shows the theoretical curves for the dependency of $S_{c,SAXS}{}^2$ on $MW_{AGU,PSt}$ determined by the core-shell model with heterogeneous shell. The cross-sectional area of main chain and PSt domain are fixed to the values determined from core-shell model analysis for PSt-cellulose in section 4-2-1-2 ($d_{celllose}$ = 1.17 g/cm^3 and $d_{PSt,solvent}$ = 0.26 g/cm^3). The theoretical curves of core-(core-shell) model I and core-Janus model I and II did not reproduce the data over the $MW_{AGU,PSt}$ range of measured in this study. As for core-Janus model II, the $d_{PEO,solvent}$ value exceeded the density of PEO in bulk as the theoretical maximum. Similarly, considering that the PEO has higher affinity to DMF than PSt (χ = 0.89, 1.5 for PEO and PSt, respectively),[18] core-(core-shell) model II showed somewhat too high $d_{PEO,solvent}$.

Hence, the author predict that the LiBr were accumulated in the PEO domain and oxygen atom coordinated to Lithium ion, which enhance the difference in electron density between PEO domain containing LiBr and the others, such as PSt domain and solvent.

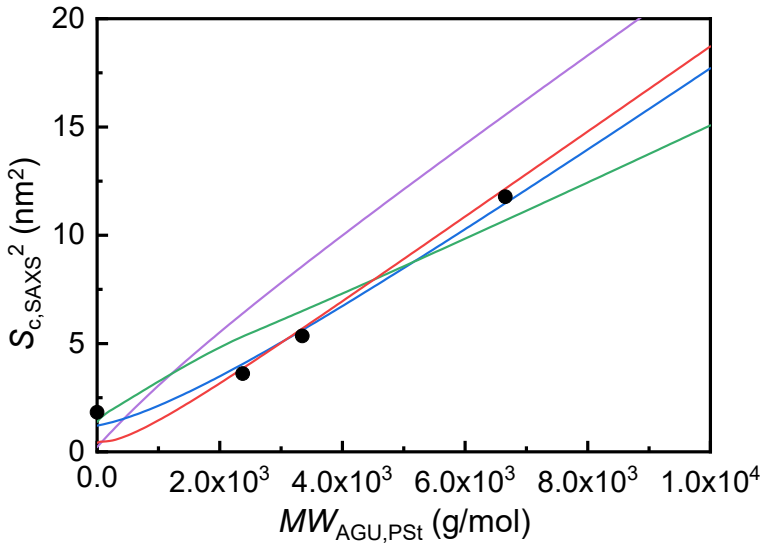

Figure 4-6. The relation between $S_{c,SAXS}^2$ and $MW_{AGU,PSt}$ for PEO-cellulose (**9**) and PEO-PSt-cellulose (**2a-c**). The purple, bule, green and red curves represent the theoretical curve for core-(core-shell) model I, core-(core-shell) model II, core-Janus I and core-Janus II model, respectively.

Table 4-4. Model parameters for the theoretical curve in figure 4-6.

model	Core-(core-shell) I	Core-(core-shell) II	Core-Janus I	Core-Janus II
reduced χ^2	35	0.75	5.7	2.3
$d_{PEO,solvent}$ (g/cm^3)	> 100	0.48	0.38	2.3

4-2-1-3-2. PEO Domain with Electron Density Increased by LiBr Coordination

The model I – IV were modified with parameter, the maximum ratio LiBr coordinating to oxygen (co-LiBr) against ethylene oxide unit (EO) in PEO graft chain $([co\text{-}LiBr]/[EO])_{max}$. It is note that the author assume that all LiBr in the SAXS sample could be concentrated in PEO domain, if the SAXS sample does not have enough LiBr to coordinate to oxygen atom of PEO side chains to reach $([co\text{-}LiBr]/[EO])_{max}$, in order to simplify the calculation.

4-2-1-3-2-1. Core-(homo-shell) Model with Accumulated LiBr

Figure 4-7 shows the relationship between $([\text{co-LiBr}]/[\text{EO}])_{max}$ and area of shell under the condition that the calculated $S_{c,SAXS}^2$ values from [co-LiBr]/[EO] and the area of shell match to experimental $S_{c,SAXS}^2$ value listed in Table 4-1. In all sample, the cross-sectional area of shell decrease with increasing $([\text{co-LiBr}]/[\text{EO}])_{max}$. This means that the $d_{PSt,solvent}$ value will increase as LiBr coordinate to oxygen atom in PEO. Thus, the author rejected this model because the $d_{PSt,solvent}$ values in PEO-PSt-cellulose become more bigger to enhance $d_{PSt,solvent}$ values in PEO-PSt-cellulose if LiBr accumulation is taken into account.

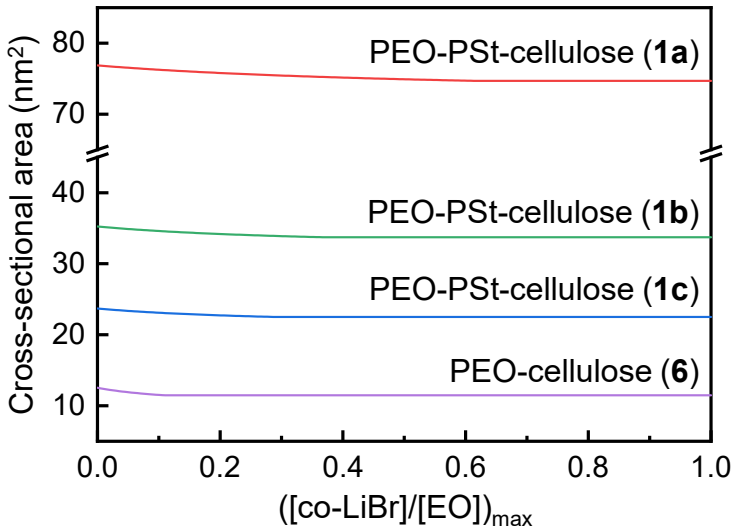

Figure 4-7. The dependency of cross-sectional area on $([\text{co-LiBr}]/[\text{EO}])_{max}$ for Core-(homo-shell) Model.

4-2-1-3-2-2. Core-(core-shell) Model and Core-Shell Model with Inhomogeneous and Coordination with LiBr

The experimental data of $S_{c,SAXS}^2$ for PEO-cellulose and PEO-PSt-cellulose were analyzed with core-(core-shell) model I, II and core-Janus model I, II modified with parameter $([co\text{-}LiBr]/[EO])_{max}$. As a result of fitting with core-(core-shell) model I and core-Janus model I, the model parameter $([co\text{-}LiBr]/[EO])_{max}$ became zero to generate the same fitting curve as those model without coordination of LiBr. On the contrary, in core-(core-shell) model II and core-Janus model II, $([co\text{-}LiBr]/[EO])_{max}$ converged to non-zero finite values (0.029 and 0.29, respectively) to reproduced well the experimental values (Figure 4-8). The theoretical curve for core-Janus model II modified with accumulated LiBr showed the smallest reduced χ^2 parameter, which is an index for goodness of fit testing, indicating that this model was most probable among the models discussed above. Thus, the author concluded that in PEO-PSt-cellulose **2a-c**, the hetero side chains underwent microphase separation to form fan-shaped shell. Though the PEO is predicted to have higher affinity for solvent than PSt since the difference in χ parameter between PEO and DMF (0.89) is smaller than that between PSt and DMF (1.5), the $d_{PEO,solvent}$ value was smaller than the $d_{PSt,solvent}$ value. This may be because the Li ion coordinate to multi oxygen atom in PEO chain to act cross-linking points in densely grafted PEO side chain. In chapter 3, SAXS measurement revealed that PSt-cellulse **1a-c** form collapsed bottlebrush in DMF/LiBr. As for PEO-PSt-cellulose, the PEO side chain did not swell than PSt side chain in DMF/LiBr, which means that PEO-PSt-cellulose form collapsed bottlebrush as with PSt-cellulse. The area ratio of PSt domain in cross section is calculated by following equation, and listed in Table 4-6;

$$f_{s,PSt} = \frac{\frac{w_{PSt}}{d_{PSt,solvent}}}{\frac{w_{PEO}}{d_{PEO,solvent}} + \frac{w_{PSt}}{d_{PSt,solvent}}} \tag{4-4}$$

where, w_{PEO} and w_{PSt} represent the weight fraction of PEO and PSt, respectively. In all PEO-PSt-cellulose, PSt domain is much larger than PEO domain, which means the surface of Janu bottlebrush is covered mainly by PSt domain. Figure 4-9 shows the [co-LiBr]/[EO] value and the

[free-LiBr] in the situation corresponding to the theoretical curve in Figure 4-8. The red solid curves in Figure 4-9 indicates that the oxygen atom in PEO side chains sufficiently coordinated to LiBr to reach the maximum ratio $([\text{co-LiBr}]/[\text{EO}])_{max}$ though PEO-cellulose did not coordinate to enough LiBr under this experimental condition ([LiBr] = 10mM).

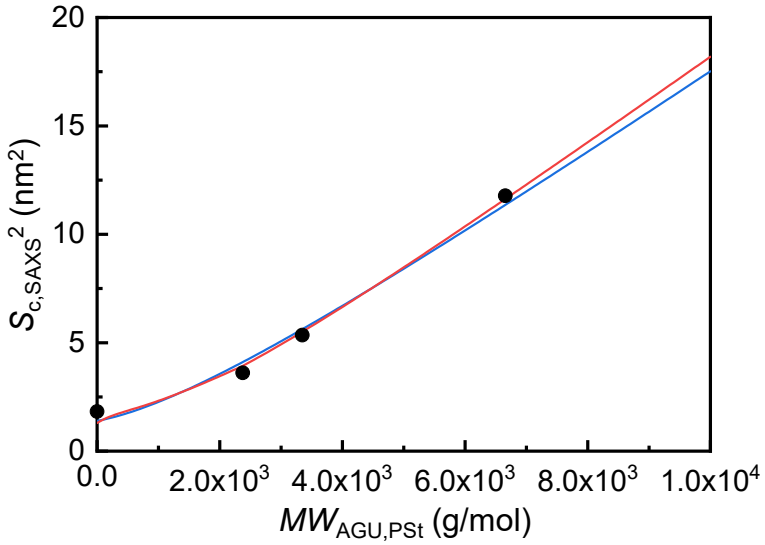

Figure 4-8. The relation between $S_{c,SAXS}^2$ and $MW_{AGU,PSt}$ for PEO-cellulose (**9**) and PEO-PSt-cellulose (**2a-c**). The bule and red curves represent the theoretical curve for core-(core-shell) model II and core-Janus II model with accumulated LiBr, respectively.

Table 4-5. Model parameters for the theoretical curve in figure 4-8.

model	Core-(core-shell) II	Core-Janus II
reduced χ^2	0.69	0.43
d_{PEO} (g/cm^3)	0.41	0.48
$([\text{co-LiBr}]/[\text{EO}])_{max}$	0.029	0.29

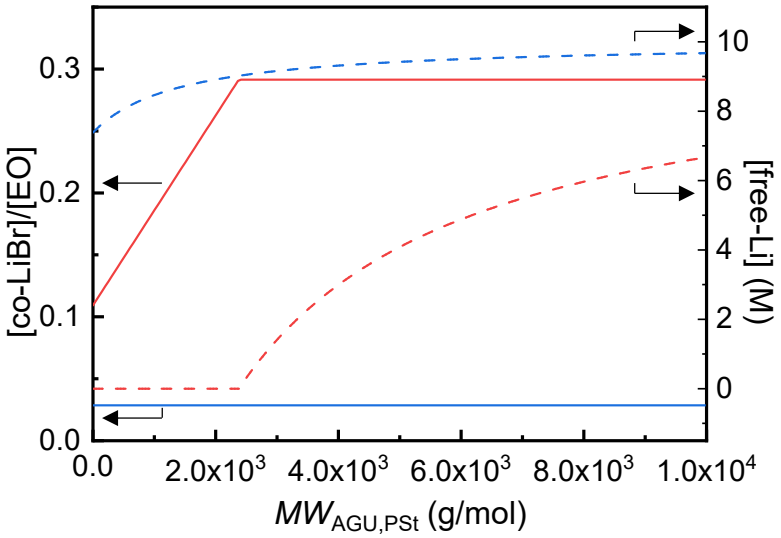

Figure 4-9. The dependency of [co-LiBr]/[EO] and [free-LiBr] on $MW_{AGU,PSt}$ calculated from model parameters listed in table 4-5; the bule curve for core-(core-shell) model II and the red curve for core-Janus II model with concentrated LiBr.

4-2-2. SEC-MALS measurement

The previous section, the author analyzed the cross-sectional structure on the assumption that the bottlebrushes took cylindrical conformation. Therefore, in the same way as chapter 3, SEC-MALS measurement and analysis with Kratky-Porod wormlike (KP) chain model were carried out with cellulosic Janus bottlebrush (PEO-PSt-cellulose) (**2a-c**) in order to confirm the validity of the assumption.

Figure 3-10 shows the SEC profiles as well as the weight average molecular weight (M_w) and radius of gyration ($\langle S^2 \rangle$) determined by MALS. Then, the relationship between $\langle S^2 \rangle$ and M_w was converted to the relationship between the mean square radius of gyration of main chain ($\langle S^2 \rangle_M$) and the degree of polymerization of the main chain ($DP_{w,main}$) in order to analyze with KP chain model;[19]

$$\langle S^2 \rangle_{\mathrm{M}} = \frac{1}{\lambda^2}\left\{\frac{\lambda L}{6} - \frac{1}{4} + \frac{1}{4\lambda L} - \frac{1}{8\lambda^2 L^2}[1 - exp(-2\lambda L)]\right\} \tag{4-5}$$

where λ^{-1} and L represent stiffness parameter and contour length of the main chain of bottlebrush. The $\langle S^2 \rangle_{\mathrm{M}}$ value is calculated from following equation;[20]

$$\langle S^2 \rangle_{\mathrm{M}} = \langle S^2 \rangle - {S_{\mathrm{c,MALS}}}^2 \tag{4-6}$$

where $S_{\mathrm{c,MALS}}$ is the cross-sectional radius of gyration for MALS and calculated by following equation with cross-sectional radius of bottlebrush in core-Janus model II (R_{cjII});

$${S_{\mathrm{c,MALS}}}^2 = \frac{{R_{\mathrm{cjII}}}^2}{2} \tag{4-7}$$

with

$${R_{\mathrm{cjII}}}^2 = \left(\frac{w_{\mathrm{backbone}}}{d_{\mathrm{cellulose}}} + \frac{w_{\mathrm{PEO}}}{d_{\mathrm{PEO,solvent}}} + \frac{w_{\mathrm{PSt}}}{d_{\mathrm{PSt,solvent}}}\right)\frac{M_0}{\pi L_{\mathrm{AGU}} N_{\mathrm{A}}} \tag{4-8}$$

where w_{backbone}, M_0, L_{AUG} and N_{A} represent weight fraction of backbone, the molecular weight and contour length of main chain per AGU (L_{AUG} = 0.52 nm), and Avogadro constant, respectively. Since the apparent contour length is elongated by side chains near both end of the main chain, the contour length of main chain L is estimated by;

$$L = \frac{M_{\mathrm{w}}}{M_{\mathrm{L}}} + 2R_{\mathrm{cJII}} \tag{4-9}$$

where M_{L} is molecular weight per unit contour length of main chain. The M_{L} value was calculated on the assumption that the contour length of main chain per repeating unit is equal to that of cellulose crystal;

$$\left(\frac{M_0}{M_{\mathrm{L}}}\right)_1 = L_{\mathrm{AGU}} \tag{4-10}$$

where M_0 represents the molecular weight per repeating unit. Figure 4-11 shows $DP_{\mathrm{w,main}}$ dependence of $\langle S^2 \rangle_{\mathrm{M}}$ for (a) **2a**, (b) **2b**, and (c) **2c**.

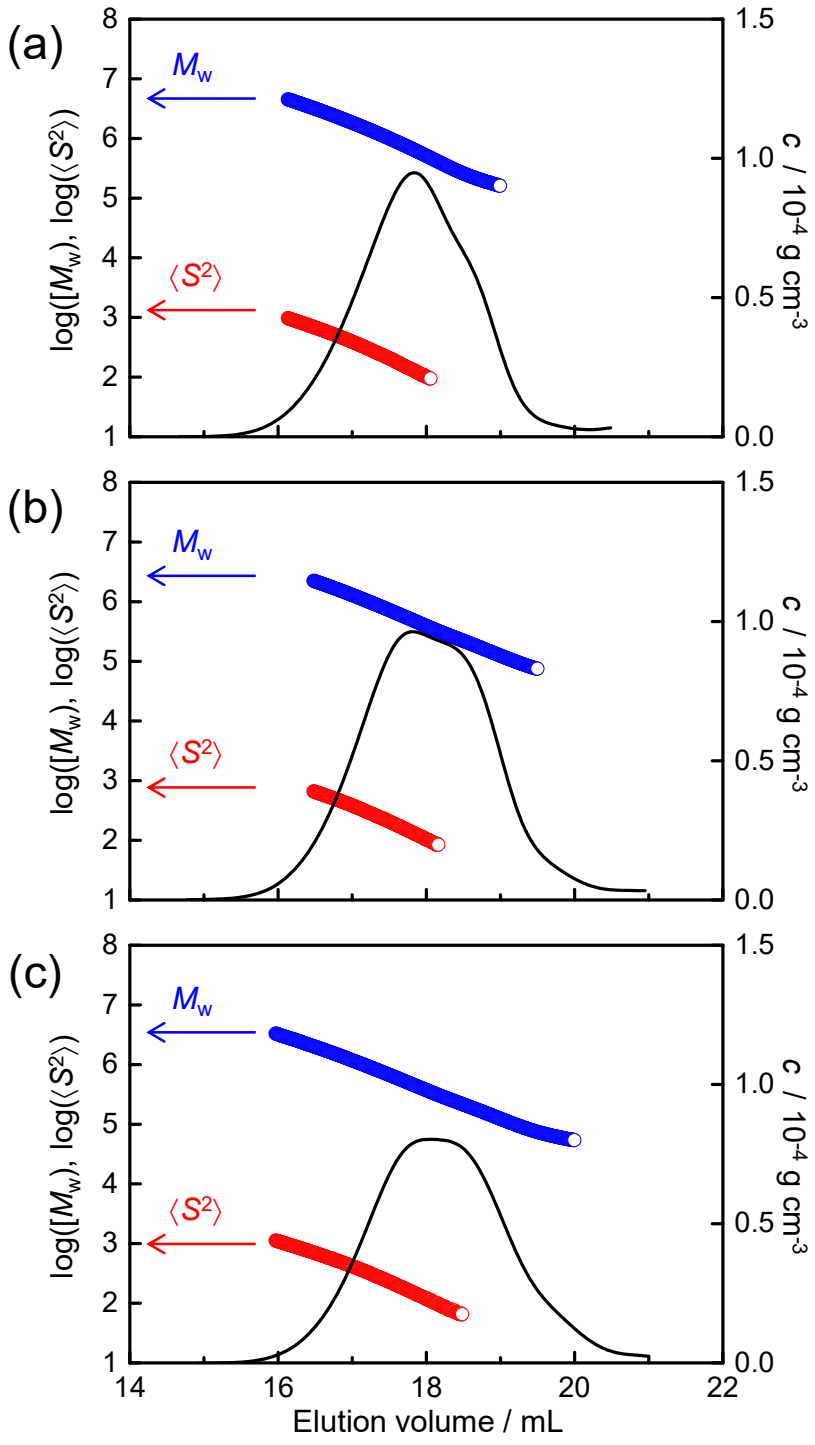

Figure 4-10. Elution-volume dependence of the weight-average molecular weight M_w (blue circles), the mean-square radius of gyration $\langle S^2 \rangle$ (red circles), and the polymer mass concentration c (solid line) for (a) **2a**, (b) **2b**, and (c) **2c**.

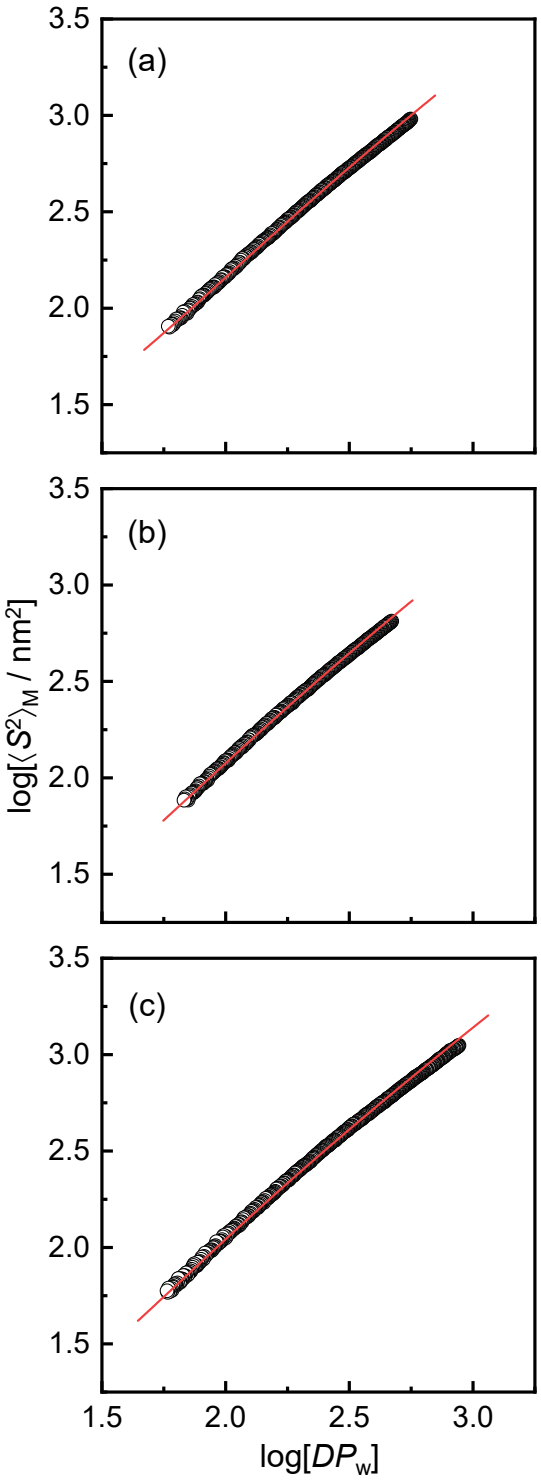

Figure 4-11 DP_w dependence of $\langle S^2 \rangle_M$ for (a) **2a**, (b) **2b**, and (c) **22c** in DMF/LiBr (black circles). The red curves represent the theoretical values calculated for the perturbed KP chain model (parameters in Table 4-6).

The theoretical curves for KP chain model well reproduced the experimental data of **2a-c** with stiffness parameter λ^{-1} (Figure 4-11). Thus, the author concluded that the main-chain conformation of cellulosic Janus bottlebrush is reconstructed with KP chain model. The values of λ^{-1} for PEO-PSt-cellulose **2a**, **2b** and, **2c** were larger than PSt-cellulose **1a**, **1b** and, **1c**, respectively (Table 4-6). Obviously, this is because PEO-PSt-cellulose have more side chains than PSt-cellulose. Additionally, one of other reason may be attributed to the restriction of the rotation of the main chain due to the effect for decreasing the interface between microphase-separated PEO and PSt domains along with the main chain. Anyway, the author had confirmed the validity of the assumption for cross-sectional Guinier approximation since PEO-PSt-cellulose did not form intramolecular aggregate.

Table 4-6. Results of SAXS and SEC-MALS measurement analyzed with core-Janus model **1**.

	Janus			Homo			
	2a	**2b**	**2c**	**1a**	**1b**	**1c**	**9**
$f_{s,PSt}$	0.92	0.84	0.79	—	—	—	—
R_{cjII} (nm)	5.4	4.0	3.5	5.3	3.8	3.3	1.6
$S_{c,MALS}{}^2$ (nm^2)	14	7.9	6.0	—	—	—	—
λ^{-1} (nm)	22	18	17	17 [a]	12 [a]	12 [a]	—

[a] the value determined in chapter 3 (Table 3-2).

4-3. Conclusion

In this chapter, the author analyzed the cross-sectional structure of mixed and homo bottlebrushes with SAXS and SEC-MALA measurement. The cross-sectional gyration $S_{c,SAXS}$ of bottlebrush is determined by cross-sectional Guinier approximation for data obtained by SAXS measurement. Comparing the dependency of $S_{c,SAXS}$ on the molecular weight of side chains in Janus bottlebrush (**2a-c**) and homo bottlebrush (**1a-c** and **9**), the author examined the validity of

some cross-sectional structure model of microphase separation. Additionally, the author carried out SEC-MALS measurement in order to confirm the validity of cross-sectional Guinier approximation by evaluating the stiffness parameter λ^{-1} in KP chain model. As a result, it is experimentally revealed that Janus bottlebrush underwent intramolecular phase separation and formed Janus-like structure with collapsed bottle structure in solution. It is revealed that the main chain of Janus bottlebrush (PEO-PSt-cellulose, **2a-c**) was stiffer than that of homo bottlebrush (PSt-cellulose, **1a-c**) and that the approximation was valid. The stiffened main chain was attribute to the density of side chains.

4-4. Acknowledgment

synchrotron SAXS experiments were performed at BL40B2 (Proposal Nos. 2016B1208 and 2017B1727) in SPring-8 with the approval of the Japan Synchrotron Radiation Research Institute (JASRI). The authors thank Dr. Noboru Ohta (JASRI/SPring-8) for assistance in the experiments on the BL40B2 beamline.

4-5. Appendix

4-5-1. Model Parameters

Table 4-7. Definition of parameter symbols.

symbol	parameter
$\Delta\rho_{e,x}$	electron density in solution
$\rho_{e,x}$	electron density in buck
ρ_x	density in bulk
S_x	cross-sectional area, which is calculated from following equation: $S_x = MW_{AGU,x}S_{MW,x}$
$S_{MW,x}$	cross-sectional area per molecular in AGU
$MW_{AGU,x}$	molecular weight per AGU
$MW_{unit,x}$	molecular weight per repeating unit or per molecule
L_{AGU}	contour length of main chain per AGU (0.52 nm)
n_x	the number electron per repeating unit or per molecule
N_A	Avogadro constant
[EO]	density of ethylene oxide repeating unit, which is calculated from following equation with concentration of bottlebrush, $conc_{bottlebrush}$ (1.0×10^{-2} g/cm^3): $[\mathrm{EO}] = \frac{conc_{\mathrm{bottlebrush}}}{MW_{\mathrm{unit,PEO}}}\frac{MW_{\mathrm{AGU,PEO}}}{MW_{\mathrm{AGU,bottlebrush}}}$
[LiBr]	density of total LiBr ([LiBr] = [co-LiBr] + [free-LiBr] = 10 mM)
[free-LiBr]	density of LiBr which is not concentrated to PEO domain
[co-LiBr]	density of LiBr which is concentrated to PEO domain $[\mathrm{co-LiBr}] = \begin{cases} [\mathrm{LiBr}], & \frac{[\mathrm{LiBr}]}{[\mathrm{EO}]} < \left(\frac{[\mathrm{co-LiBr}]}{[\mathrm{EO}]}\right)_{max} \\ [\mathrm{EO}]\left(\frac{[\mathrm{co-LiBr}]}{[\mathrm{EO}]}\right)_{max}, & \frac{[\mathrm{LiBr}]}{[\mathrm{EO}]} > \left(\frac{[\mathrm{co-LiBr}]}{[\mathrm{EO}]}\right)_{max} \end{cases}$
$\left(\frac{[\mathrm{co-LiBr}]}{[\mathrm{EO}]}\right)_{max}$	the maximum ratio LiBr coordinating to oxygen (co-LiBr) to ethylene oxide unit (EO) in PEO domain.

Table 4-8. Parameters value for analysis of SAXS data.

x	PEO	PSt	main chain	DMF	LiBr
n_x	24	56	180 for **1** 146 for **2** and **9**	40	38
$MW_{unit,x}$ (g/mol)	44.05	104.14	—	73.10	86.85
$MW_{AGU,x}$ (g/mol)	—	—	282 for **1** 276 for **2** and **9**	—	—
ρ_x (g/cm^3)	1.13	1.05	—	0.944	3.46

Table 4-9. Equations to calculate parameters, $MW_{\mathrm{unit,x}}$, $MW_{\mathrm{AGU,x}}$, ρ_{x}, $\rho_{\mathrm{e,x}}$ and $\Delta\rho_{\mathrm{e,x}}$.

x	PEO	PSt	cellulose	solvent
$MW_{\mathrm{unit,x}}$	$MW_{\mathrm{AGU,PEO}} + \frac{[\mathrm{co-LiBr}]}{[\mathrm{EO}]} MW_{\mathrm{LiBr}}$	$MW_{\mathrm{unit,PSt}}$	—	—
$MW_{\mathrm{AGU,x}}$	$MW_{\mathrm{PEO}} DS_{\mathrm{PEO}}$	$M_{\mathrm{n,PSt}} DS_{\mathrm{PSt}}$	$M_0 - \left(MW_{\mathrm{PEO}} DS_{\mathrm{PEO}} + M_{\mathrm{n,PSt}} DS_{\mathrm{PSt}}\right)$	—
ρ_{x}	$\frac{MW_{\mathrm{unit,PEO}} + \frac{[\mathrm{co-LiBr}]}{[\mathrm{EO}]} MW_{\mathrm{LiBr}}}{\frac{MW_{\mathrm{unit,PEO}}}{\rho_{\mathrm{PEO}}} + \frac{[\mathrm{co-LiBr}]}{[\mathrm{EO}]} \frac{MW_{\mathrm{LiBr}}}{\rho_{\mathrm{LiBr}}}}$	ρ_{PSt}	—	—
$\rho_{\mathrm{e,x}}$	$\frac{n_{\mathrm{PEO}} + \frac{[\mathrm{co-LiBr}]}{[\mathrm{EO}]} n_{\mathrm{LiBr}}}{\frac{MW_{\mathrm{unit,PEO}}}{\rho_{\mathrm{PEO}}} + \frac{[\mathrm{co-LiBr}]}{[\mathrm{EO}]} \frac{MW_{\mathrm{LiBr}}}{\rho_{\mathrm{LiBr}}}} N_{\mathrm{A}}$	$\frac{N_{\mathrm{A}} n_{\mathrm{PSt}} \rho_{\mathrm{PSt}}}{MW_{\mathrm{unit,PSt}}}$	—	$\frac{\frac{\rho_{\mathrm{solv}} n_{\mathrm{solvent}}}{MW_{\mathrm{solvent}}} + [\mathrm{free-LiBr}] n_{\mathrm{LiBr}}}{1 + [\mathrm{free-LiBr}] \times \frac{MW_{\mathrm{LiBr}}}{\rho_{\mathrm{LiBr}}}} N_A$
$\Delta\rho_{\mathrm{e,x}}$	$\frac{(\rho_{\mathrm{e,PEO}} - \rho_{\mathrm{e,solvent}}) MW_{\mathrm{AGU,PEO}}}{N_{\mathrm{A}} S_{\mathrm{PEO}} L_{\mathrm{AGU}} \rho_{\mathrm{PEO}}}$	$\frac{(\rho_{\mathrm{e,PSt}} - \rho_{\mathrm{e,solvent}}) MW_{\mathrm{AGU,PSt}}}{N_{\mathrm{A}} S_{\mathrm{PSt}} L_{\mathrm{AGU}} \rho_{\mathrm{PSt}}}$	$\frac{n_{\mathrm{e,cellulose}}}{S_{\mathrm{cellulose}} L_{\mathrm{AGU}}} - \rho_{\mathrm{e,solve}}$	—

4-5-2. Scattering Intensity for Randomly Oriented Long Cylinder

The scattering intensity $I(q)$ of randomly oriented particle in spherical coordinate is given by

$$I(q) = \frac{1}{4\pi}\int_{-\pi}^{\pi} d\varphi \int_{0}^{\pi} d\theta \sin\theta \, F(q,\theta,\varphi)F^{*}(q,\theta,\varphi) \tag{4-11}$$

here, $F(q,\theta,\varphi)$ and is form factor and q is the absolute value of scattering vector $\boldsymbol{q}$ which is described by spherical coordinate ($\boldsymbol{q} = q(\sin\theta\cos\varphi, \sin\theta\sin\varphi, \cos\theta)$).

If the form factor for the cylinder with length L extremely larger than the diameter (Figure 4-12) is given by

$$F(q,\theta,\varphi) = \frac{L\sin\left(q\cos\theta\,(L/2)\right)}{q\cos\theta\,(L/2)} F_{\mathrm{c}}(q,\sin\theta\,,\varphi) \tag{4-12}$$

the scattering intensity is simplified as following equation:

$$\begin{aligned}
I(q) &= \frac{1}{4\pi}\int_{-\pi}^{\pi} d\varphi \int_{0}^{\pi} d\theta \sin\theta \, F(q,\theta,\varphi)F^{*}(q,\theta,\varphi) \\
&= \frac{1}{4\pi}\int_{-\pi}^{\pi} d\varphi \sin\theta \left(\frac{L\sin\left(q\cos\theta\,(L/2)\right)}{q\cos\theta\,(L/2)}\right)^{2} \int_{0}^{2\pi} d\varphi \, F_{\mathrm{c}}(q,\theta,\varphi){F_{\mathrm{c}}}^{*}(q,\theta,\varphi) \\
&= \frac{1}{4\pi}\int_{-\pi}^{\pi} d\varphi \sin\theta \left(\frac{L\sin\left(q\cos\theta\,(L/2)\right)}{q\cos\theta\,(L/2)}\right)^{2} \times \int_{0}^{2\pi} d\varphi \, F_{\mathrm{c}}\left(q,\frac{\pi}{2},\varphi\right){F_{\mathrm{c}}}^{*}\left(q,\frac{\pi}{2},\varphi\right) \\
&= \frac{1}{4\pi}\frac{2L\pi}{q}\int_{-\pi}^{\pi} d\varphi \, F_{\mathrm{c}}\left(q,\frac{\pi}{2},\varphi\right){F_{\mathrm{c}}}^{*}\left(q,\frac{\pi}{2},\varphi\right) = \frac{L}{2q}\int_{-\pi}^{\pi} d\varphi \, F_{\mathrm{c}}\left(q,\frac{\pi}{2},\varphi\right){F_{\mathrm{c}}}^{*}\left(q,\frac{\pi}{2},\varphi\right)
\end{aligned} \tag{4-13}$$

Where, F_{c} is cross-sectional form factor.

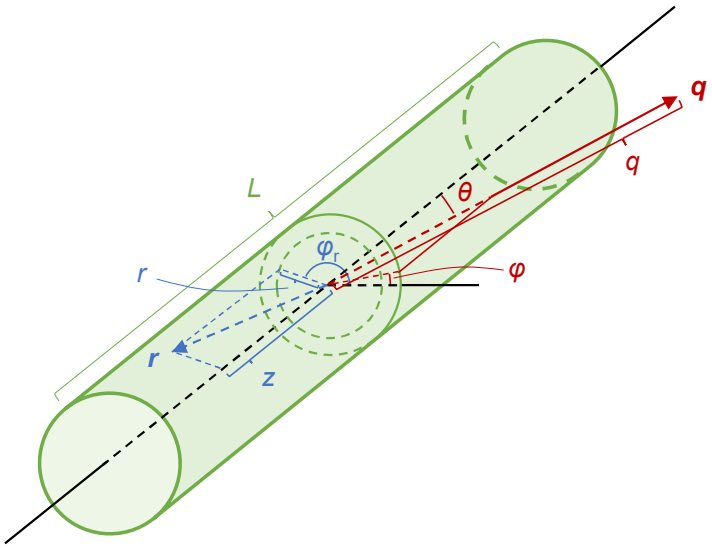

Figure 4-12. Schematic illustration of cylinder in spherical coordinate.

4-5-2. Cross-Sectional Form Factor for Bottlebrushes

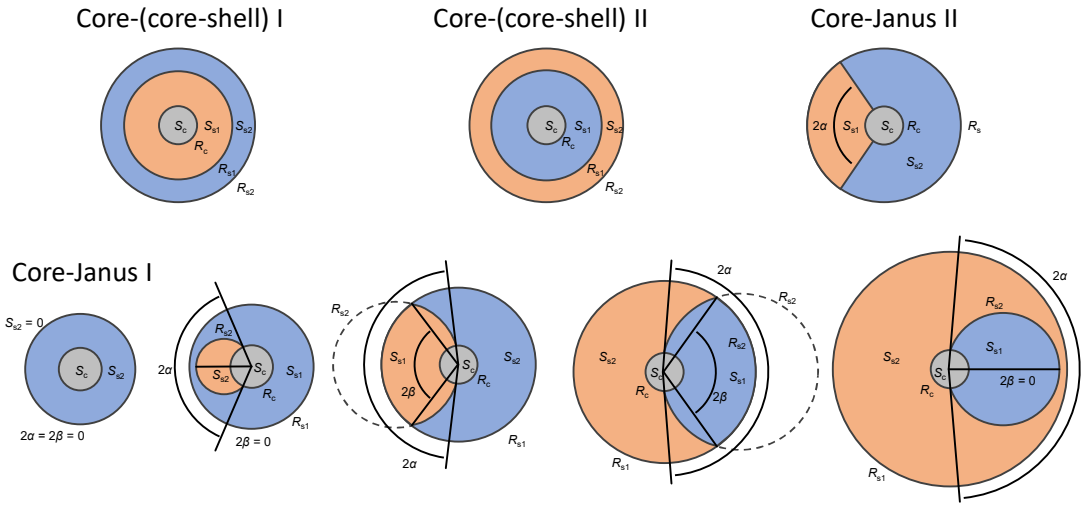

Figure 4-13. Schematic illustration of model parameter for cross-sectional structure of bottlebrush with intramolecular microphase separation. Grey, bule and orange area represent core (cellulose) and swollen PEO and PSt domains, respectively.

4-5-2-1. Core-Shell Model

The F_c for cylinder with core-shell structure (core-(homo-shell) model in Figure 4-3 and core-(core-shell) model I and II in Figure 4-5) is written by

$$F_c(q,\theta,\varphi) = 2\pi\left(\Delta\rho_{e,s2}{R_{s2}}^2\frac{J_1[qR_{s2}\sin\theta]}{qR_{s2}\sin\theta} + \left(\Delta\rho_{e,s1}-\Delta\rho_{e,s2}\right){R_{s1}}^2\frac{J_1[qR_{s1}\sin\theta]}{qR_{s1}\sin\theta} + \left(\Delta\rho_{e,c}-\Delta\rho_{e,s1}\right){R_1}^2\frac{J_1[qR_c\sin\theta]}{qR_c\sin\theta}\right) \quad (4\text{-}14)$$

where, $\Delta\rho_{e,c}$, $\Delta\rho_{e.s1}$ and $\Delta\rho_{e,s2}$, and R_c, R_{s1} and R_{s2} are electron density and radius for core, inner shell and outer shell, respectively (Figure 4-13). When $qR_{s2} < 1$, $I(q)$ is simplified as following equation:

$$\begin{aligned}
I(q) &= \frac{1}{4\pi}\int_{-\pi}^{\pi} d\varphi\, F_c\left(q,\frac{\pi}{2},\varphi\right)F_c^*\left(q,\frac{\pi}{2},\varphi\right)\\
&= \int_{-\pi}^{\pi} d\varphi\left[2\pi\left(\Delta\rho_{e,s2}{R_{s2}}^2\frac{J_1[qR_{s2}]}{qR_{s2}} + \left(\Delta\rho_{e,s1}-\Delta\rho_{e,s2}\right){R_{s1}}^2\frac{J_1[qR_{s1}]}{qR_{s1}} + \left(\Delta\rho_{e,c}-\Delta\rho_{e,s1}\right){R_c}^2\frac{J_1[qR_c]}{qR_c}\right)\right]^2\\
&= 2\pi^2\left[\frac{1}{4}\left(\Delta\rho_{e,s2}{R_{s2}}^2 + \left(\Delta\rho_{e,s1}-\Delta\rho_{e,s2}\right){R_{s1}}^2 + \left(\Delta\rho_{e,c}-\Delta\rho_{e,s1}\right){R_c}^2\right)^2\right.\\
&\quad -\frac{1}{16}\left(\Delta\rho_{e,s2}{R_{s2}}^2 + \left(\Delta\rho_{e,s1}-\Delta\rho_{e,s2}\right){R_{s1}}^2 + \left(\Delta\rho_{e,c}-\Delta\rho_{e,s1}\right){R_c}^2\right)\left(\Delta\rho_{e,s2}{R_{s2}}^4\right.\\
&\quad \left.\left.+\left(\Delta\rho_{e,s1}-\Delta\rho_{e,s2}\right){R_{s1}}^4 + \left(\Delta\rho_{e,c}-\Delta\rho_{e,s1}\right){R_c}^4\right)q^2\right] + \cdots\\
&= \frac{1}{2}\pi^2\left(\Delta\rho_{e,s2}{R_{s2}}^2 + \left(\Delta\rho_{e,s1}-\Delta\rho_{e,s2}\right){R_{s1}}^2 + \left(\Delta\rho_{e,c}-\Delta\rho_{e,s1}\right){R_c}^2\right)^2\\
&\quad \times\exp\left(-\frac{1}{4}\frac{\Delta\rho_{e,s2}{R_{s2}}^4 + \left(\Delta\rho_{e,s1}-\Delta\rho_{e,s2}\right){R_{s1}}^4 + \left(\Delta\rho_{e,c}-\Delta\rho_{e,s1}\right){R_c}^4}{\Delta\rho_{e,s2}{R_{s2}}^2 + \left(\Delta\rho_{e,s1}-\Delta\rho_{e,s2}\right){R_{s1}}^2 + \left(\Delta\rho_{e,c}-\Delta\rho_{e,s1}\right){R_c}^2}q^2\right)
\end{aligned} \quad (4\text{-}15)$$

Therefore,

$$\ln[I(q)q] = C - \frac{1}{4}\frac{\Delta\rho_{e,s2}{R_{s2}}^4 + \left(\Delta\rho_{e,s1}-\Delta\rho_{e,s2}\right){R_{s1}}^4 + \left(\Delta\rho_{e,c}-\Delta\rho_{e,s1}\right){R_c}^4}{\Delta\rho_{e,s2}{R_{s2}}^2 + \left(\Delta\rho_{e,s1}-\Delta\rho_{e,s2}\right){R_{s1}}^2 + \left(\Delta\rho_{e,c}-\Delta\rho_{e,s1}\right){R_c}^2}q^2 \quad (4\text{-}16)$$

where, C represent constant.

Table 4-10. Model parameters for core-shell model

	core-(homo-shell)		core-(core-shell) I		core-(core-shell) II	
concentrated LiBr in PEO domain	absent	present	absent	present	absent	present
$([\text{co-LiBr}]/[\text{EO}])_{max}$	0	Variable	0	Variable	0	Variable
$\Delta\rho_{e,c}$	$\Delta\rho_{e,cellulose}$		$\Delta\rho_{e,cellulose}$		$\Delta\rho_{e,cellulose}$	
$\Delta\rho_{e,s1}$	$\left(\frac{(\rho_{e,PEO}-\rho_{e,solvent})MW_{AGU,PEO}}{\rho_{PEO}} + \frac{(\rho_{e,PSt}-\rho_{e,solvent})MW_{AGU,PSt}}{\rho_{PSt}}\right) \div N_A SL_{AGU}$		$\Delta\rho_{e,PSt}$		$\Delta\rho_{e,PEO}$	
$\Delta\rho_{e,s2}$	0		$\Delta\rho_{e,PEO}$		$\Delta\rho_{e,PSt}$	
R_c	$((S_{cellulose}/\pi)^{1/2}$		$((S_{cellulose})/\pi)^{1/2}$		$((S_{cellulose})/\pi)^{1/2}$	
R_{s1}	$((S_{cellulose}+S)/\pi)^{1/2}$		$((S_{cellulose}+S_{PSt})/\pi)^{1/2}$		$((S_{cellulose}+S_{PEO})/\pi)^{1/2}$	
R_{s2}	0		$((S_{cellulose}+S_{PSt}+S_{PEO})/\pi)^{1/2}$		$((S_{cellulose}+S_{PEO}+S_{PSt})/\pi)^{1/2}$	

4-5-2-2. Core-Janus Model I

The F_c for cylinder with core-Janus model I in Figure 4-3 is written by

$$
\begin{aligned}
F_{\mathrm{c}}(q,\theta,\varphi) = {} & 2\pi\Delta\rho_{\mathrm{e,s1}}\frac{L\sin\left(q\cos\theta\,(L/2)\right)}{q\cos\theta\,(L/2)}\frac{{R_{\mathrm{s1}}}^2 J_1(qR_{\mathrm{s1}}\sin\theta)}{qR_{\mathrm{s1}}\sin\theta} \\
& + \frac{L\sin\left(q\cos\theta\,(L/2)\right)}{q\cos\theta\,(L/2)}\Bigg\{\left(\Delta\rho_{\mathrm{e,s2}}\right. \\
& \left. - \Delta\rho_{\mathrm{e,s1}}\right)\Bigg[\int_{-\pi/2}^{\pi/2} d\varphi_{\mathrm{r}}\frac{1}{A^2}\left(e^{iA2R_{\mathrm{s2}}\cos\varphi_{\mathrm{r}}}[1-iA2R_{\mathrm{s2}}\cos\varphi_{\mathrm{r}}]-1\right) \\
& - \int_{-\beta}^{\beta} d\varphi_{\mathrm{r}}\frac{1}{A^2}\left(e^{iA2R_{2}\cos\varphi_{\mathrm{r}}}[1-iA2R_{\mathrm{s2}}\cos\varphi_{\mathrm{r}}]\right. \\
& \left. - e^{iAR_{\mathrm{s1}}}[1-iAR_{\mathrm{s1}}]\right)\Bigg]\Bigg\} \\
& + 2\pi\Delta\rho_{\mathrm{e,c-s1}}\frac{L\sin\left(q\cos\theta\,(L/2)\right)}{q\cos\theta\,(L/2)}\frac{{R_c}^2 J_1(qR_{\mathrm{c}}\sin\theta)}{qR_{\mathrm{c}}\sin\theta} \\
& + \frac{L\sin\left(q\cos\theta\,(L/2)\right)}{q\cos\theta\,(L/2)}\Bigg\{\left(\Delta\rho_{\mathrm{e,c-s2}}\right. \\
& \left. - \Delta\rho_{\mathrm{e,c-s1}}\right)\Bigg[\int_{-\pi/2}^{\pi/2} d\varphi_{\mathrm{r}}\frac{1}{A^2}\left(e^{iA2R_{\mathrm{s2}}\cos\varphi_{\mathrm{r}}}[1-iA2R_{\mathrm{s2}}\cos\varphi_{\mathrm{r}}]-1\right) \\
& - \int_{-\alpha}^{\alpha} d\varphi_{\mathrm{r}}\frac{1}{A^2}\left(e^{iA2R_{\mathrm{s2}}\cos\varphi_{\mathrm{r}}}[1-iA2R_{\mathrm{s2}}\cos\varphi_{\mathrm{r}}]\right. \\
& \left. - e^{iAR_{\mathrm{c}}}[1-iAR_{\mathrm{c}}]\right)\Bigg]\Bigg\}
\end{aligned}
\tag{4-17}
$$

with

$$A = q\sin\theta\cos(\varphi_{\mathrm{r}}-\varphi) \tag{4-18}$$

$$\Delta\rho_{\mathrm{e,c-s1}} = \Delta\rho_{\mathrm{e,c}} - \Delta\rho_{\mathrm{e,s1}} \tag{4-19}$$

$$\Delta\rho_{\mathrm{e,c-s2}} = \Delta\rho_{\mathrm{e,c}} - \Delta\rho_{\mathrm{e,s2}} \tag{4-20}$$

where, $\Delta\rho_{\mathrm{e,c}}$, $\Delta\rho_{\mathrm{e.s1}}$ and $\Delta\rho_{\mathrm{e,s2}}$ represent electron density for core, shell 1 and outer shell 2, respectively, and R_{c}, R_{s1} and R_{s2} represent radius for core and shell, respectively (Figure4-13). When $qR_{\mathrm{s}} < 1$, $I(q)$ is simplified as following equation:

$$
\begin{aligned}
I(q) = \frac{1}{4\pi}\int_{-\pi}^{\pi} d\varphi\, F_{\mathrm{c}}\left(q,\frac{\pi}{2},\varphi\right) F_{\mathrm{c}}{}^{*}\left(q,\frac{\pi}{2},\varphi\right) \\
&= \int_{-\pi}^{\pi} d\varphi \left| 2\pi\Delta\rho_{\mathrm{e,s1}} \frac{{R_1}^2 J_1(qR_{\mathrm{s1}}\sin\theta)}{qR_{\mathrm{s1}}\sin\theta} \right. \\
&+ \left\{ \left(\Delta\rho_{\mathrm{e,s2}} \right. \right. \\
&- \Delta\rho_{\mathrm{e,s1}}\Big) \left[\int_{-\pi/2}^{\pi/2} d\varphi_{\mathrm{r}} \frac{1}{q^2B^2} \left(e^{i2qBR_{\mathrm{s2}}\cos\varphi_{\mathrm{r}}} [1 - i2qBR_{\mathrm{s2}}\cos\varphi_{\mathrm{r}}] \right. \right. \\
&- 1\Big) \\
&- \int_{-\beta}^{\beta} d\varphi_{\mathrm{r}} \frac{1}{q^2B^2} \left(e^{i2qB\ \ R_{\mathrm{s2}}\cos\varphi_{\mathrm{r}}} [1 - i2qBR_{\mathrm{s2}}\cos\varphi_{\mathrm{r}}] \right. \\
&\left. \left. \left. - e^{iqBR_{\mathrm{s1}}} [1 - iqBR_{\mathrm{s1}}]\Big) \right] \right\} + 2\pi\Delta\rho_{\mathrm{e,c-s1}} \frac{{R_c}^2 J_1(qR_{\mathrm{c}}\sin\theta)}{qR_{\mathrm{c}}\sin\theta} \\
&+ \left\{ \left(\Delta\rho_{\mathrm{e,c-s2}} \right. \right. \\
&- \Delta\rho_{\mathrm{e,c-s1}}\Big) \left[\int_{-\pi/2}^{\pi/2} d\varphi_{\mathrm{r}} \frac{1}{q^2B^2} \left(e^{i2qBR_{\mathrm{s2}}\cos\varphi_{\mathrm{r}}} [1 - i2qBR_{\mathrm{s2}}\cos\varphi_{\mathrm{r}}] \right. \right. \\
&- 1\Big) \\
&- \int_{-\alpha}^{\alpha} d\varphi_{\mathrm{r}} \frac{1}{q^2B^2} \left(\int_{-\pi/2}^{\pi/2} d\varphi_{\mathrm{r}} \frac{1}{q^2B^2} \left(e^{i2qBR_{\mathrm{s2}}\cos\varphi_{\mathrm{r}}} [1 \right. \right. \right. \\
&\left. \left. \left. \left. - i2qBR_{\mathrm{s2}}\cos\varphi_{\mathrm{r}}] - 1\Big) \right) \right] \right\} \Bigg|^2
\end{aligned}
\tag{4-21}
$$

with

$$
B = \cos(\varphi_{\mathrm{r}} - \varphi) \tag{4-22}
$$

Therefore,

$$
\begin{aligned}
\ln[I(q)q] = C - \Bigg[& 2\Big({R_{s1}}^2\big(\pi\Delta\rho_{e,s1} + \big(\Delta\rho_{e,s2} - \Delta\rho_{e,s1}\big)\beta\big) \\
& + {R_c}^2\big(\pi\Delta\rho_{e,c-s1} - \big(\Delta\rho_{e,s2} - \Delta\rho_{e,s1}\big)\alpha\big) \\
& + {R_{s2}}^2\big(\Delta\rho_{e,2} - \Delta\rho_{e,1}\big)\big((2\alpha + \sin(2\alpha)) - (2\beta + \sin(2\beta))\big)\Big)^2 \\
& \times \frac{1}{4}\pi\Bigg({R_{s1}}^4\big(\pi\Delta\rho_{e,s1} + \big(\Delta\rho_{e,s2} - \Delta\rho_{e,s1}\big)\beta\big) \\
& + {R_c}^4\big(\pi\Delta\rho_{e,s1} - \big(\Delta\rho_{c,s2} - \Delta\rho_{e,s1}\big)\alpha\big) \\
& + \big(\Delta\rho_{c,s2} - \Delta\rho_{e,s1}\big){R_{s2}}^4\Bigg(\Big(6\alpha + 4\sin 2\alpha + \frac{1}{2}\sin 4\alpha\Big) \\
& - \Big(6\beta + 4\sin 2\beta + \frac{1}{2}\sin 4\beta\Big)\Bigg)\Bigg) \\
& - \pi\Big(\frac{\Delta\rho_{c,s2} - \Delta\rho_{e,s1}}{3}\Big)^2\Bigg({R_{s2}}^3\Big(6\alpha + 4\sin 2\alpha + \frac{1}{2}\sin 4\alpha\Big) \\
& - {R_{s2}}^3\Big(6\beta + 4\sin 2\beta + \frac{1}{2}\sin 4\beta\Big) - 2{R_1}^3(\sin\alpha - \sin\beta)\Bigg)^2\Bigg] \\
& \div \Big[2\pi\Big({R_{s1}}^2\big(\pi\Delta\rho_{e,s1} + \big(\Delta\rho_{c,s2} - \Delta\rho_{e,s1}\big)\beta\big) \\
& + {R_c}^2\big(\pi\Delta\rho_{e,c-s1} - \big(\Delta\rho_{c,s2} - \Delta\rho_{e,s1}\big)\alpha\big) \\
& + {R_{s2}}^2\big(\Delta\rho_{c,s2} - \Delta\rho_{e,s1}\big)\big((2\alpha + \sin(2\alpha)) - (2\beta + \sin(2\beta))\big)\Big)^2\Big] \\
& \times q^2
\end{aligned}
\tag{4-23}
$$

where, C represent constant.

when the area of circle R_{s2} is equal to a quarter of area of circle R_{S1}, α is expressed in the following equation:

$$\alpha = \cos^{-1}\left(\frac{R_c}{R_1}\right) \tag{4-24}$$

Thus, the overlapping area of circle R_{s2} and R_c (S_{Rs2Rc}) is calculated as:

$$S_{Rs2Rc} = {R_c}^2\alpha + \left(\left(\frac{R_{s1}}{2}\right)^2(\pi - 2\alpha) - \sin\alpha\frac{R_{s1}}{2}R_c\right) \tag{4-25}$$

Thus, S_{Rs2} is calculated from the following equation:

$$\begin{aligned} S_{Rs2} = S_{Rs2Rc} + S_{s2} &= {R_c}^2\alpha + \left(\left(\frac{R_{s1}}{2}\right)^2(\pi - 2\alpha) - \sin\alpha\frac{R_{s1}}{2}R_c\right) + S_{s2} \\ &= {R_c}^2\cos^{-1}\left(\frac{R_c}{R_{s1}}\right) \\ &+ \left(\left(\frac{R_{s1}}{2}\right)^2\left(\pi - 2\cos^{-1}\left(\frac{R_c}{R_{s1}}\right)\right) - \sin\left(\cos^{-1}\left(\frac{R_c}{R_{s1}}\right)\right)\frac{R_{s1}}{2}R_c\right) \\ &+ S_{s2} \end{aligned} \tag{4-26}$$

(i) When, S_{Rs2} is smaller than a quarter of S_{R1}, β is equal to 0 and the S_{Rs2Rc} is calculated form the following equation:

$$\begin{aligned} S_{Rs2Rc} &= {R_c}^2\alpha + ((R_{s2})^2(\pi - 2\alpha) - \sin\alpha\, R_{s2}R_c) \\ &= {R_c}^2\alpha + \left(\left(\frac{R_c}{2\cos\alpha}\right)^2(\pi - 2\alpha) - \sin\alpha\frac{R_c}{2\cos\alpha}R_c\right) \end{aligned} \tag{4-27}$$

Thus, S_{s2} is calculated as:

$$\begin{aligned} S_{s2} = \pi{R_{s2}}^2 - S_{Rs2Rc} &= \pi{R_{s2}}^2 - \left({R_c}^2\alpha + \left({R_{s2}}^2(\pi - 2\alpha) - \sin\alpha\, R_{s2}R_c\right)\right) \\ &= 2\alpha{R_{s2}}^2 - {R_c}^2\alpha + \sin\alpha\, R_{s2}R_c \\ &= 2\alpha\left(\frac{R_c}{2\cos\alpha}\right)^2 - {R_c}^2\alpha + \sin\alpha\left(\frac{R_c}{2\cos\alpha}\right)R_c \end{aligned} \tag{4-28}$$

where, $R_{s2} = \frac{R_c}{2\cos\alpha}$.

α is the value that satisfies the following relationship:

$$\begin{aligned} \frac{S_{s2}}{S_c} &= \frac{2\alpha\left(\frac{R_c}{2\cos\alpha}\right)^2 - {R_c}^2\alpha + \sin\alpha\left(\frac{R_c}{2\cos\alpha}\right)R_c}{\pi{R_c}^2} \\ &= \left(\frac{R_c}{R_{s1}}\right)^2\left(2\alpha\left(\frac{1}{2\cos\alpha}\right)^2 - \alpha + \sin\alpha\left(\frac{1}{2\cos\alpha}\right)\right)\Big/\pi \end{aligned} \tag{4-29}$$

(ik) When, S_{Rs2} is larger than a quarter of S_{R1}, the overlapping area of circle R_{s2} and circle R_{s1} (S_{Rs1Rs2}) and the overlapping area of circle R_{s2} and circle R_c (S_{Rs1Rc}) are represented as:

$$S_{\mathrm{Rs1Rs2}} = {R_{\mathrm{s1}}}^2\beta + ((R_{\mathrm{s2}})^2(\pi - 2\beta) - \sin\beta\, R_{\mathrm{s2}}R_{\mathrm{s1}}) \tag{4-30}$$

$$S_{\mathrm{Rs2Rc}} = {R_{\mathrm{c}}}^2\alpha + ((R_{\mathrm{s2}})^2(\pi - 2\alpha) - \sin\alpha\, R_{\mathrm{s2}}R_{\mathrm{c}}) \tag{4-31}$$

Thus, S_{s2} is calculated from following equation:

$$\begin{aligned} S_{\mathrm{s2}} &= S_{\mathrm{Rs1Rs2}} - S_{\mathrm{Rs1Rs2}} \\ &= \left({R_{\mathrm{s1}}}^2\beta + ((R_{\mathrm{s2}})^2(\pi - 2\beta) - \sin\beta\, R_{\mathrm{s2}}R_{\mathrm{s1}})\right) \\ &\quad - \left({R_{\mathrm{c}}}^2\alpha + ((R_{\mathrm{s2}})^2(\pi - 2\alpha) - \sin\alpha\, R_{\mathrm{s2}}R_{\mathrm{c}})\right) \\ &= 2\left(\frac{R_{\mathrm{s1}}}{2\cos\beta}\right)^2\left(\cos^{-1}\left(\frac{R_{\mathrm{c}}}{R_{\mathrm{s1}}}\cos\beta\right) - \beta\right) \\ &\quad + \frac{R_{\mathrm{s1}}}{2\cos\beta}\left(\sin\left(\cos^{-1}\left(\frac{R_c}{R_{\mathrm{s1}}}\cos\beta\right)\right)R_{\mathrm{c}} - \sin\beta\, R_{\mathrm{s1}}\right) + {R_{\mathrm{s1}}}^2\beta \\ &\quad - {R_{\mathrm{c}}}^2\cos^{-1}\left(\frac{R_{\mathrm{c}}}{R_1}\cos\beta\right) \end{aligned} \tag{4-32}$$

where, $\alpha = \cos^{-1}\left(\frac{R_{\mathrm{c}}}{R_{\mathrm{s1}}}\cos\beta\right)$、$R_2 = \frac{R_{\mathrm{s1}}}{2\cos\beta}$.

β is the value that satisfies the following relationship:

$$\begin{aligned} \frac{S_{\mathrm{S2}}}{S_{\mathrm{c}} + S_{\mathrm{s1}} + S_{\mathrm{s2}}} &= 2\left(\frac{1}{2\cos\beta}\right)^2\left(\cos^{-1}\left(\frac{R_{\mathrm{c}}}{R_{\mathrm{s1}}}\cos\beta\right) - \beta\right) \\ &\quad + \frac{1}{2\cos\beta}\left(\sin\left(\cos^{-1}\left(\frac{R_{\mathrm{c}}}{R_{\mathrm{s1}}}\cos\beta\right)\right)\frac{R_{\mathrm{c}}}{R_{\mathrm{s1}}} - \sin\beta\right) + \beta \\ &\quad - \left(\frac{R_{\mathrm{c}}}{R_{\mathrm{s1}}}\right)^2\cos^{-1}\left(\frac{R_{\mathrm{c}}}{R_{\mathrm{s1}}}\cos\beta\right) \end{aligned} \tag{4-33}$$

4-5-2-3. Core-Janus Model II

The F_c for cylinder with core-Janus II in Figure 4-3 is written by[21]

$$F_{\mathrm{c}}(q,\theta,\varphi) = 2\pi\Delta\rho_{\mathrm{e,c}}\frac{{R_c}^2 J_1(qR_c\sin\theta)}{qR_c\sin\theta} + \int_{-\pi}^{\pi} d\varphi_{\mathrm{r}}\,\Delta\rho_{\mathrm{e}}(\varphi_{\mathrm{r}})\frac{1}{A^2}\left(e^{iAR_s}[1-iAR_s] - e^{iAR_c}[1-iAR_c]\right) \tag{4-34}$$

with

$$\Delta\rho_{\mathrm{e}}(\varphi_{\mathrm{r}}) = \begin{cases}\Delta\rho_{\mathrm{e,s1}}, & -\alpha < \varphi_{\mathrm{r}} < \alpha \\ \Delta\rho_{\mathrm{e,s2}}, & else\end{cases} \tag{4-35}$$

$$\alpha = \frac{S_{\mathrm{s1}}}{S_{\mathrm{s1}} + S_{\mathrm{s2}}} \tag{4-36}$$

$$A = q\sin\theta\cos(\varphi_{\mathrm{r}} - \varphi) \tag{4-37}$$

where, $\Delta\rho_{\mathrm{e,c}}$, $\Delta\rho_{\mathrm{e.s1}}$ and $\Delta\rho_{\mathrm{e,s2}}$ represent electron density for core, shell 1 and outer shell 2, respectively, and R_{c}, R_{s1} and R_{s2} represent radius for core and shell, respectively (Figure4-13). When $qR_{\mathrm{s}} < 1$, $I(q)$ is simplified as following equation:

$$
\begin{aligned}
I(q) = \frac{1}{4\pi}\int_{-\pi}^{\pi} d\varphi\, F_{\mathrm{c}}\left(q,\frac{\pi}{2},\varphi\right) F_{\mathrm{c}}{}^{*}\left(q,\frac{\pi}{2},\varphi\right) \\
&= \frac{1}{4\pi}\int_{-\pi}^{\pi} d\varphi \left| 2\pi\Delta\rho_{\mathrm{e,c}} \frac{{R_c}^2 J_1(qR_c)}{qR_c} \right. \\
&+ \int_{-\pi}^{\pi} d\varphi_{\mathrm{r}}\, \Delta\rho_{\mathrm{e}}(\varphi_{\mathrm{r}}) \frac{1}{q^2B^2} \left(e^{iqBR_s}[1 - iqBR_s] \right. \\
&\left. \left. - e^{iqB\ {}_c}[1 - iqBR_c] \right) \right|^2 \\
&= \frac{1}{4\pi} \left\{ \left(\Delta\rho_{\mathrm{e,c}} {R_c}^2 + \Delta\rho_{\mathrm{e},\alpha}\left({R_s}^2 - {R_c}^2\right) \right)^2 \right. \\
&- \left(\frac{1}{4} \left(\Delta\rho_{\mathrm{e,c}} {R_c}^2 + \Delta\rho_{\mathrm{e},\alpha}\left({R_s}^2 - {R_c}^2\right) \right) \left(\Delta\rho_{\mathrm{e,c}} {R_c}^4 \right. \right. \\
&\left. + \Delta\rho_{\mathrm{e},\alpha}\left({R_s}^4 - {R_c}^4\right) \right) \\
&\left. \left. - 2\left(\frac{\sin\alpha}{3\pi}\right)^2 \left({R_s}^3 - {R_c}^3\right)^2 \left(\Delta\rho_{\mathrm{e},1} - \Delta\rho_{\mathrm{e},2}\right)^2 \right) \right\} \qquad (4\text{-}38) \\
&= \frac{1}{4\pi} \left\{ \left(\Delta\rho_{\mathrm{e,c}} {R_c}^2 + \Delta\rho_{\mathrm{e},\alpha}\left({R_s}^2 - {R_c}^2\right) \right)^2 \right. \\
&\times exp\left(- \frac{1}{\left(\Delta\rho_{\mathrm{e,c}} {R_c}^2 + \Delta\rho_{\mathrm{e},\alpha}\left({R_s}^2 - {R_c}^2\right) \right)^2} \right. \\
&\times \left(\frac{1}{4} \left(\Delta\rho_{\mathrm{e,c}} {R_c}^2 + \Delta\rho_{\mathrm{e},\alpha}\left({R_s}^2 - {R_c}^2\right) \right) \left(\Delta\rho_{\mathrm{e,c}} {R_c}^4 \right. \right. \\
&\left. + \Delta\rho_{\mathrm{e},\alpha}\left({R_s}^4 - {R_c}^4\right) \right) \\
&\left. \left. \left. - 2\left(\frac{\sin\alpha}{3\pi}\right)^2 \left({R_s}^3 - {R_c}^3\right)^2 \left(\Delta\rho_{\mathrm{e},1} - \Delta\rho_{\mathrm{e},2}\right)^2 \right) \right) \right\}
\end{aligned}
$$

with

$$B = \cos(\varphi_{\mathrm{r}} - \varphi) \qquad (4\text{-}39)$$

$$\pi\Delta\rho_{\mathrm{e},\alpha} = \pi\Delta\rho_{\mathrm{e},2} + \alpha\left(\Delta\rho_{\mathrm{e},1} - \Delta\rho_{\mathrm{e},2}\right) \qquad (4\text{-}40)$$

Therefore,

$$\ln[I(q)q] = C - \left\{ \frac{1}{\left(\Delta\rho_{\mathrm{e,c}} {R_c}^2 + \Delta\rho_{\mathrm{e},\alpha}\left({R_s}^2 - {R_c}^2\right)\right)^2} \times \left(\frac{1}{4}\left(\Delta\rho_{\mathrm{e,c}} {R_c}^2 + \Delta\rho_{\mathrm{e},\alpha}\left({R_s}^2 - {R_c}^2\right)\right)\left(\Delta\rho_{\mathrm{e,c}} {R_c}^4 + \Delta\rho_{\mathrm{e},\alpha}\left({R_s}^4 - {R_c}^4\right)\right) - 2\left(\frac{\sin\alpha}{3\pi}\right)^2 \left({R_s}^3 - {R_c}^3\right)^2 \left(\Delta\rho_{\mathrm{e},1} - \Delta\rho_{\mathrm{e},2}\right)^2 \right) \right\} \quad (4\text{-}41)$$

where, C represent constant.

Table 4-11. Model parameters for core-Jansu model.

	core-Janus I		core-Janus I	
concentrated LiBr in PEO domain	absent	present	absent	present
$([\text{co-LiBr}]/[\text{EO}])_{max}$	0	Variable	0	Variable
$\Delta\rho_{e,c}$	$\Delta\rho_{e,cellulose}$		$\Delta\rho_{e,cellulose}$	
$\Delta\rho_{e,s1}$	$\Delta\rho_{e,PSt}$ ($S_{PSt} \leq S_{PEO}$) $\Delta\rho_{e,PEO}$ ($S_{PEO} < S_{PSt}$)		$\Delta\rho_{e,PSt}$	
$\Delta\rho_{e,s2}$	$\Delta\rho_{e,PEO}$ ($S_{PSt} \leq S_{PEO}$) $\Delta\rho_{e,PSt}$ ($S_{PSt} < S_{PEO}$)		$\Delta\rho_{e,PEO}$	
R_c	$(S_{cellulose}/\pi)^{1/2}$		$(S_{cellulose}/\pi)^{1/2}$	
R_s	$((S_{cellulose} + S_{PSt} + S_{PEO})/\pi)^{1/2}$		$((S_{cellulose} + S_{PSt} + S_{PEO})/\pi)^{1/2}$	

4-6. References

1. Pelras, T.; Mahon, C. S.; Mullner, M. Synthesis and Applications of Compartmentalised Molecular Polymer Brushes. *Angew. Chem., Int. Ed.* **2018**, *57*, 6982-6994.
2. Chen, K.; Hu, X.; Zhu, N.; Guo, K. Design, Synthesis, and Self-Assembly of Janus Bottlebrush Polymers. *Macromol Rapid Commun* **2020**, 2000357.
3. Le, A. N.; Liang, R.; Zhong, M. Synthesis and Self-Assembly of Mixed-Graft Block Copolymers. *Chemistry* **2019**, *25*, 8177-8189.
4. Xie, G.; Krys, P.; Tilton, R. D.; Matyjaszewski, K. Heterografted Molecular Brushes as Stabilizers for Water-in-Oil Emulsions. *Macromolecules* **2017**, *50*, 2942-2950.
5. Li, Y.; Zou, J.; Das, B. P.; Tsianou, M.; Cheng, C. Well-Defined Amphiphilic Double-Brush Copolymers and Their Performance as Emulsion Surfactants. *Macromolecules* **2012**, *45*, 4623-4629.
6. Palacios-Hernandez, T.; Luo, H.; Garcia, E. A.; Pacheco, L. A.; Herrera-Alonso, M. Nanoparticles from Amphiphilic Heterografted Macromolecular Brushes with Short Backbones. *Macromolecules* **2018**, *51*, 2831-2837.
7. Chang, H. Y.; Lin, Y. L.; Sheng, Y. J.; Tsao, H. K. Multilayered Polymersome Formed by Amphiphilic Asymmetric Macromolecular Brushes. *Macromolecules* **2012**, *45*, 4778-4789.
8. Nam, J.; Kim, Y.; Kim, J. G.; Seo, M. Self-Assembly of Monolayer Vesicles via Backbone-Shiftable Synthesis of Janus Core–Shell Bottlebrush Polymer. *Macromolecules* **2019**, *52*, 9484-9494.
9. Guo, Z. H.; Le, A. N.; Feng, X.; Choo, Y.; Liu, B.; Wang, D.; Wan, Z.; Gu, Y.; Zhao, J.; Li, V.; Osuji, C. O.; Johnson, J. A.; Zhong, M. Janus Graft Block Copolymers: Design of a Polymer Architecture for Independently Tuned Nanostructures and Polymer Properties. *Angew. Chem., Int. Ed.* **2018**, *57*, 8493-8497.
10. Kawamoto, K.; Zhong, M.; Gadelrab, K. R.; Cheng, L. C.; Ross, C. A.; Alexander-Katz, A.; Johnson, J. A. Graft-through Synthesis and Assembly of Janus Bottlebrush Polymers from A-Branch-B Diblock Macromonomers. *J. Am. Chem. Soc.* **2016**, *138*, 11501-4.
11. Stepanyan, R.; Subbotin, A.; ten Brinke, G. Comb Copolymer Brush with Chemically Different Side Chains. *Macromolecules* **2002**, *35*, 5640-5648.
12. Hsu, H.-P.; Paul, W.; Binder, K. Intramolecular Phase Separation of Copolymer "Bottle Brushes": No Sharp Phase Transition but a Tunable Length Scale. *Europhys. Lett.* **2006**, *76*, 526-532.
13. Theodorakis, P. E.; Paul, W.; Binder, K. Analysis of the Cluster Formation in Two-Component Cylindrical Bottle-Brush Polymers under Poor Solvent Conditions: a Simulation Study. *Eur. Phys. J. E: Soft Matter Biol. Phys.* **2011**, *34*, 52.
14. de Jong, J.; ten Brinke, G. Conformational Aspects and Intramolecular Phase Separation of

Alternating Copolymacromonomers: A Computer Simulation Study. *Macromol. Theory Simul.* **2004**, *13*, 318-327.

15. Klemm, D.; Heublein, B.; Fink, H. P.; Bohn, A. Cellulose: Fascinating Biopolymer and Sustainable Raw Material. *Angew. Chem., Int. Ed. Engl.* **2005**, *44*, 3358-93.
16. Glatter, O.; Kratky, O. *Small Angle X-ray Scattering*. Academic Press: London, 1982.
17. Wataoka, I.; Kobayashi, K.; Kajiwara, K. Effect of the Carbohydrate Side-Chain on the Conformation of a Glycoconjugate Polystyrene in Aqueous Solution. *Carbohydr. Res.* **2005**, *340*, 989-995.
18. Grulke, E. A. Solubility Parameter Values. In *Polymer Handbook*, 4th ed.; Brandrup, J.; Immergut, E. H.; Grulke, E. A., Eds. Wiley: New York, 1999; pp VI-675 - VI-714.
19. Benoit, H.; Doty, P. Light Scattering from Non-Gaussian Chains. *J. Phys. Chem.* **1953**, *57*, 958-963.
20. Yamakawa, H.; Yoshizaki, T. *Helical Wormlike Chains in Polymer Solutions*. 2nd ed.; Springer, Berlin Heidelberg: Berlin, 2016.
21. Walther, A.; Drechsler, M.; Rosenfeldt, S.; Harnau, L.; Ballauff, M.; Abetz, V.; Muller, A. H. Self-Assembly of Janus Cylinders into Hierarchical Superstructures. *J. Am. Chem. Soc.* **2009**, *131*, 4720-4728.

Chapter 5

Thermal Property and Microphase Separation of Janus Cellulosic Bottlebrushes in Bulk

5-1. Introduction

Janus bottlebrushes, bearing two immiscible side chains attached to the polymeric backbone densely,[1-5] have emerged as a fascinating polymeric architecture from the viewpoints of precise polymer synthesis,[6-14] self-assembly,[14-26] and applications such as emulsion surfactants,[27,28] antifouling surface,[29] ion conductive membranes,[30] and so on. They possess the characteristics of conventional bottlebrushes such as cylindrical structure, backbone stiffness, low entanglement, and ultrahigh molecular weight. Thus, Janus bottlebrushes exhibit self-assembled morphologies and dynamics distinct from those of traditional linear block copolymers.[31-33] For example, sub-10 nm periodic patterns have successfully been prepared from Janus bottlebrushes in bulk, which overcomes the criteria of χN for the formation of microphase separation with short graft chain lengths (small N), where χ and N are the Flory-Huggins interaction parameter and the degree of polymerization.[34,35]

One of the most striking characteristics is that, in the microphase separation of Janus bottlebrushes, the polymeric backbone exists at the interface between the two blocks. Thus, the nature of the backbone would affect the formation of the morphologies and functionalities. Cellulose is a polysaccharide consisting of β-1,4-glycosidic linked D-glucose units with perfect stereoregularity. Cellulose is regarded as a semiflexible (semirigid) linear polymer, adopting helical conformation, which are exemplified by cholesteric liquid crystalline formation and chiral separation.[4, 30, 36] Janus cellulosic bottlebrushes, graft copolymers with two different side chains

in every anhydroglucose unit (AGU) regioselectively, could therefore phase separate to form the microdomain structures as similar to methacrylate-[33] and norbornene-based[31,34-35] Janus bottlebrushes, though not explored yet. The author further expects novel morphologies and functionalities from the cellulosic Janus bottlebrushes because cellulose resides at the phase separation interface.

In this chapter, the author demonstrated the formation of solid-state microphase separation of Janus cellulosic bottlebrush with polystyrene (PSt) and poly(ε-caprolactone) (PCL) chains at C-6 and C-2,3 positions of AGU, respectively (3, Figure 5-1). The bulk samples were characterized by small-angle X-ray scattering (SAXS) and transmission electron microscope (TEM), revealing the formation of the lamellar morphologies. This is the first study to exemplify the microphase separation of Janus cellulosic bottlebrushes in bulk.

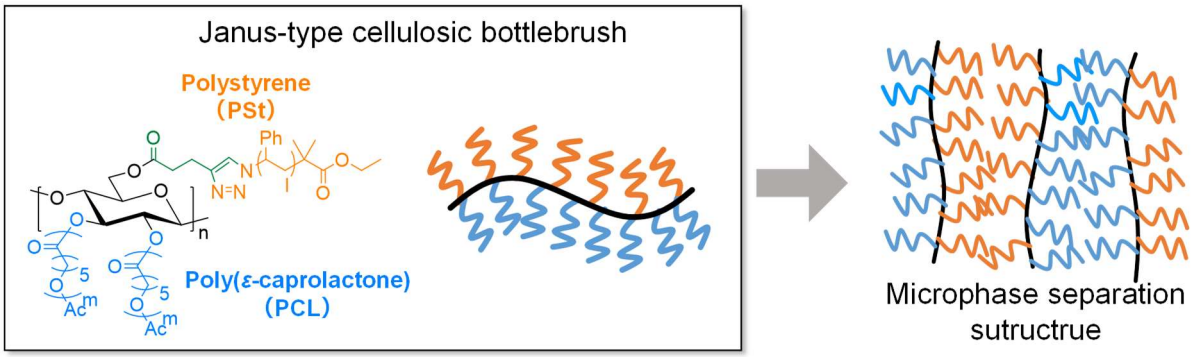

Figure 5-1. Schematic of this study based on the regioselectively-grafted Janus cellulosic bottlebrushes (**3**)

5-2. Experimental Section

5-2-1. Samples

The studied Janus cellulosic bottlebrushes with a PCL and PSt side chain (of different molecular weights) in every AGU were synthesized and characterized in Chapter 2. Their molecular characteristics are shown in Table 5-1.

Table 5-1. Molecular characteristics of Janus cellulosic bottlebrush **3a-c**.

Sample	Grafted PCL				Grafted PS-N_3				Bottlebrush	
	M_n[a] (10^5 g mol^{-1})	PDI[a]	*DP*[b]	*DS*[b]	M_n[a] (10^3 g mol^{-1})	PDI[a]	*DP*	*DS*	$f_{PS} : f_{PCL}$[c]	χ_C[d] (%)
3a					4.0	1.1	38	0.84	0.20 : 0.80	44
3b	7.3	1.5	100	1.5	9.2	1.1	90	0.75	0.44 : 0.56	44
3c					16.0	1.1	158	0.64	0.54 : 0.46	37

[a]Determined by GPC in THF using PSt standards. [b]Determined by ^{1}H-NMR. [c]Volume fraction ratio of PS and PCL, determined by ^{1}H-NMR. [d]Percentage of crystallinity of PCL.

5-2-2. Instrumentation and Measurements

Thermogravimetric analysis (TGA) was performed on a SDT Q600 (TA Instruments Japan) under a continuous flow of nitrogen gas from 25 to 500 °C at a heating rate of 10 °C min^{-1}. Differential scanning calorimetry (DSC) measurements were carried out on a Discover DSC 2500 (TA Instruments Japan) from -80 to 200 °C at a heating/cooling rate of 10 °C min^{-1} under nitrogen atmosphere. Small-angle X-ray scattering (SAXS) measurement was performed on Rigaku NANO-Viewer equipped with a detector PILATUS 100K (Rigaku Co., Tokyo, Japan) having 487 × 195 pixels of a 172 μm pixel size. The X-ray wavelength (λ) was 0.154 nm. The sample-to-detector distance was 1320 mm. The scattered intensities are expressed as a function of the scattering vector $q = 4\pi \sin\theta/\lambda$, where 2θ is the scattering angle. The q value was calibrated using silver behenate. The excess scattering intensity $I(q)$ was obtained as the difference of

scattering intensity between the sample and air. TEM images were acquired using a JEM-2100 (JEOL, Japan) microscope (accelerating voltage, 200 kV) equipped with a CCD camera. Ultrathin sections were prepared using a Leica Ultracut R ultramicrotome with a diamond knife at rt. Prior to the ultramicrotomy, the block samples were stained with ruthenium tetroxide (RuO_4). Sections of about 100 nm thickness of the block samples were collected on a carbon-coated Cu grid.

5-3. Results and Discussion

Figure 5-2 shows the thermal properties of **3a-c** measured by TGA and DSC under nitrogen atmosphere. The decomposition of the bottlebrushes **3a-c** started at a temperature over 310 °C, which is reasonable since the decomposition of the neat PCL and PS started over 330 °C. The DSC curves of **3a-c** exhibited the melting and the glass-transition peaks for PCL and PS grafts at 53 and 97 °C, respectively. The peak positions were unchanged among **3a-c**, whereas the peak area for the PCL melting depended well on the volume fraction of PCL (Table 5-1). According to these results, the thermal annealing temperature was set 120 °C under vacuum for the formation of microphase separation. From the area of the melting peak (ΔH_m) for PCL, the percentage of crystallinity (χ_C) for PCL was determined according to the equation $\chi_C = (100 \cdot \Delta H_m) / \Delta H^0_m \cdot w)$, where $\Delta H^0_m = 135.44$ J g^{-1} is the heat of fusion of fully crystalline PCL[37] and w is the weight fraction of PCL in the bottlebrushes. The χ_C values were 30-50 % for **3a-c**, suggesting that the crystallinity was influenced by the PS blocks in this study, comparative to the behavior of PCL-*block*-PS where the PCL crystallization significantly depends on the volume fraction.[38]

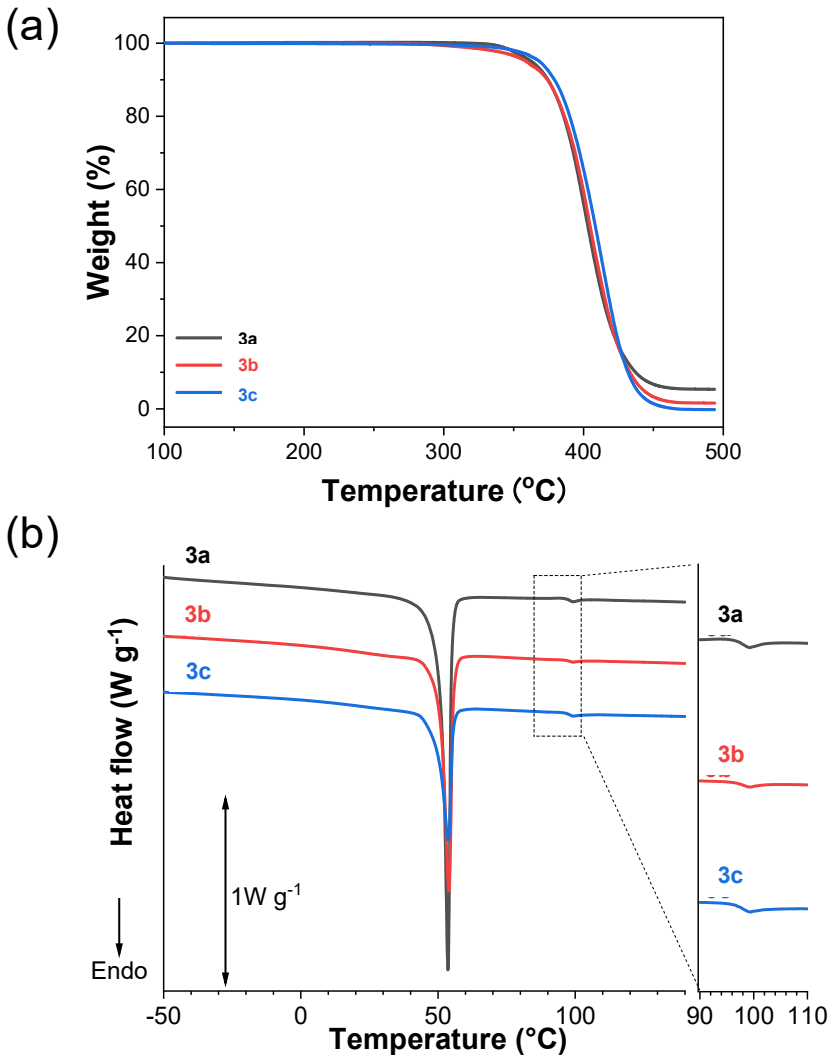

Figure 5-2. (a) TGA (10 °C min^{-1}) and (b) DSC (2nd heating; 10 °C min^{-1})

The solution of **3a – c** in toluene (10 wt%) was casted on a poly(tetrafluoroethylene) dish. The as-prepared film was annealed at 120 °C under vacuum for 24 h and then cooled gradually to rt under vacuum. Figure 5-3 presents SAXS patterns for **3a-c** bulk films. The scattering peaks for **3b** and **3c**, corresponding to a ratio of 1:2, suggest the lamellar morphology, thought the scattering patters were scarce because of the small difference in electron density

between PCL and PSt.[38] From the principal scattering vector q^*, the lamellar thickness was calculated using $d = 2\pi/ q^*$ to be 30 and 34 nm for **3b** and **3c**, respectively. Though the broad scattering for **3a** suggests irregular morphology, the domain size was deduced to be 19 nm from the broad peak top position. Thus, the characteristic size (d) depended on the length of PS grafts, **3a** < **3b** < **3c**. It was confirmed that the SAXS patterns were almost unchanged as the annealing condition varied (higher annealing temperature or longer time) (Figure 5-4).

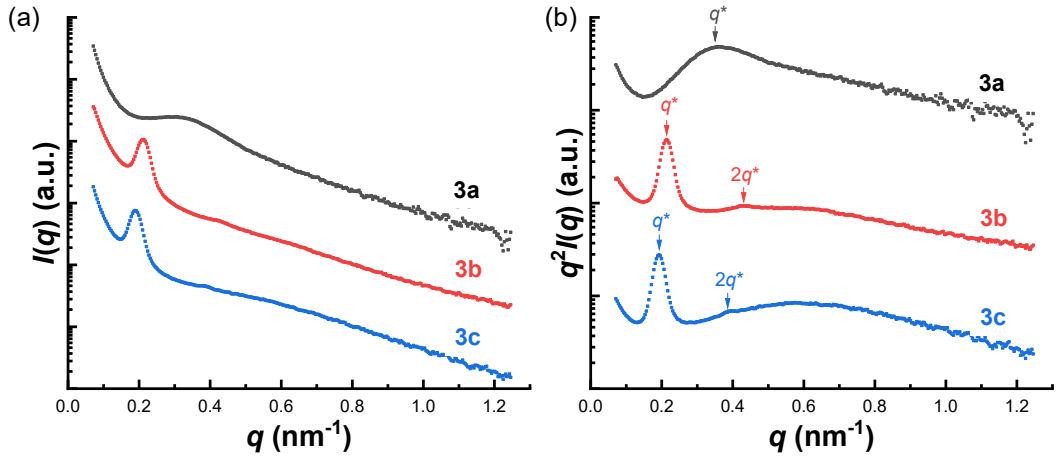

Figure 5-3. SAXS curves for **3a-c** bulk films. Downward arrows in Figure b indicate the positions of the estimated lattice structure factor peaks.

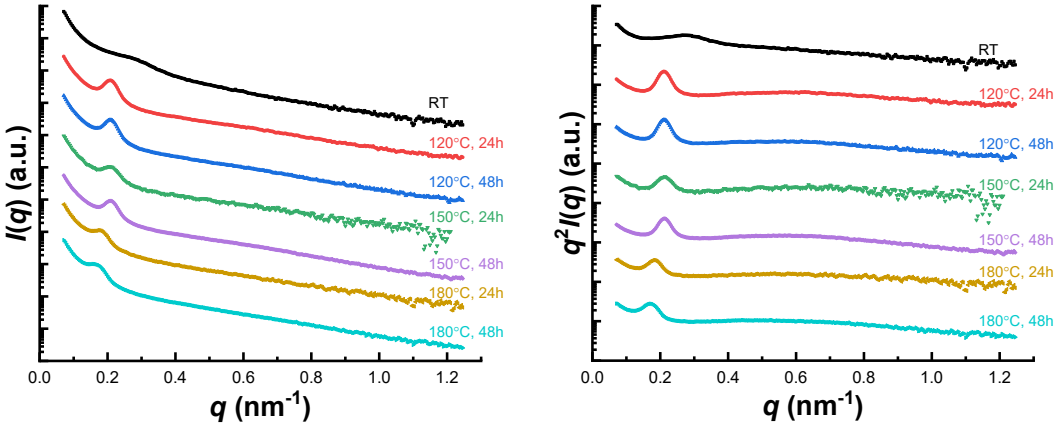

Figure 5-4. SAXS curves for **3b** bulk films annealed at various conditions as indicated.

The morphology of the Janus bottlebrushes was further examined by TEM in order to observe the lamellar structure. Figure 5-6 shows the TEM images for **3b** and **3c** bulk films annealed at 120 °C for 24h. Before observation, the samples were stained with RuO_4. There were lamellar structures with three distinguishable regions as dark, gray, and white. Since RuO_4 reacts preferentially with double bounds and diffuses into amorphous regions, both of the aromatic PS and the amorphous PCL regions became stained, whereas the crystalline regions of PCL were white. The crystallinity of PCL in the bulk films, determined by DSC, was around 55 % for **3b** and **3c** (Figure 5-5). Based on the microdomain sizes from SAXS, the black and gray regions were assigned to be the amorphous PCL and PS regions (Figure 5-6d). Though the observed microdomain structure and orientation were not so homogeneous, the interdistance of **3b** and **3c** were estimated to be about 26 and 29 nm, respectively, from the TEM images, which were slightly smaller than those (30 and 34 nm for **3b** and **3c**) determined by SAXS. The width of the

amorphous and crystal PCL and the PS regions were about 5, 6, and 10 nm for **3b**, and 5, 6, and 13 nm for **3c**, respectively. The width of the amorphous and crystal PCL regions was the same between **3b** and **3c**, apparently because of the same length of the PCL grafts. It is assumed that the cellulose backbone resides between the amorphous PS and PCL regions, since the PCL chains close to the cellulose backbone are restricted and thus cannot crystallize. On the contrary, the PCL chains apart from the cellulose backbone can move freely and thus fold intra- and intermolecularly to crystallize.

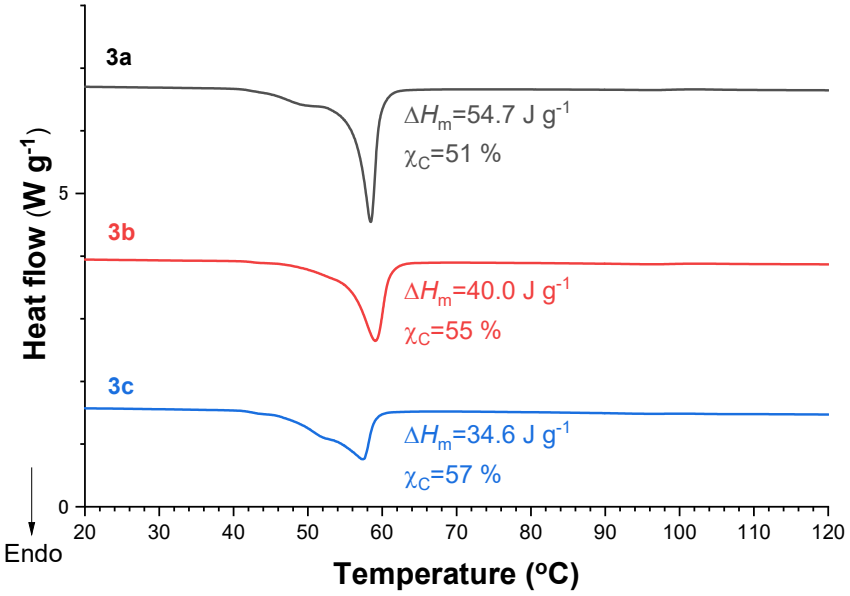

Figure 5-5. DSC thermograms (heating) for the bulk films of **3a-c**

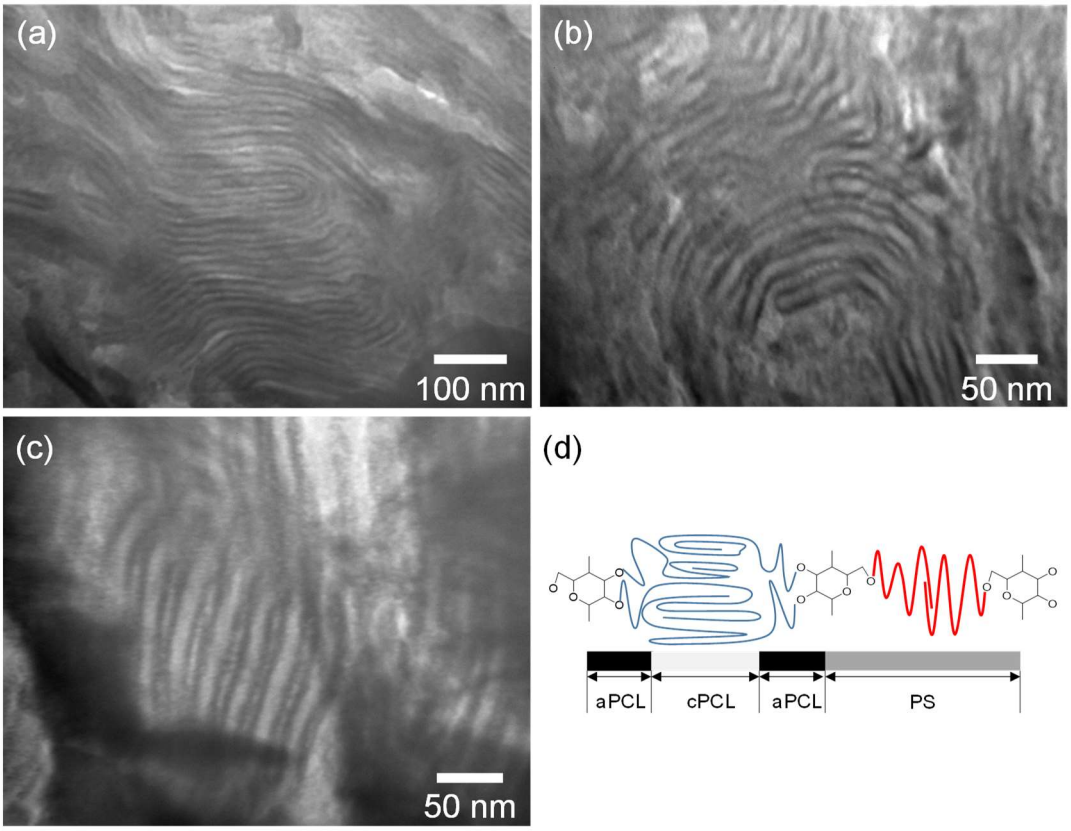

Figure 5-6. TEM images of (a, b) **3b** and (c) **3c** bulk films annealed at 120 °C for 24h. (e) Schematic illustration of the packing of the Janus bottlebrush with the stained regions. cPCL: crystalline PCL; aPCL: amorphous PCL.

Higher annealing temperature and further annealing time improved the homogeneity of the microdomain structure. Figure 5-7 shows the TEM images of samples **3b** and **3c** annealed at 150 °C for 7 days, exhibiting lamellar fingerprints clearly. The grain sizes were larger over 500 nm, in which several strands of the microdomains were oriented windingly. These results exemplified that cellulose as the polymeric backbone for Janus bottlebrushes can exhibit microscale morphologies without interfering the microphase separation. The author expects that cellulosic Janus bottlebrushes will potentially develop new morphologies and functionalities owing to the cellulose inherent rigidity and helicity.

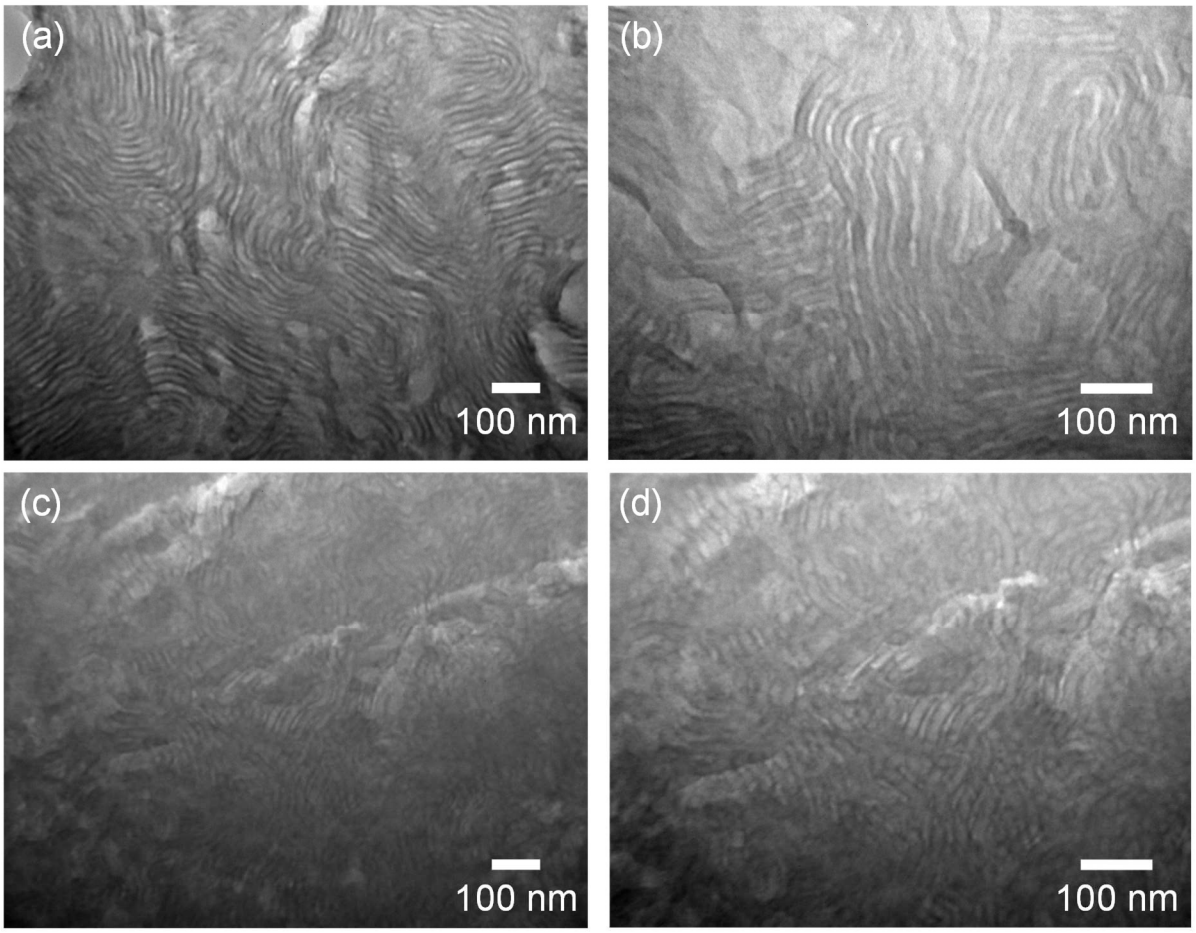

Figure 5-7. TEM images of (a, b) **3b** and (c, d) **3c** bulk films annealed at 150 °C for 7 days.

5-4. Conclusion

The annealed bulk samples of the Janus bottlebrushes exhibited lamellar morphology when the PS/PCL volume ration of around 50/50, characterized by SAXS and TEM. The lamellar structure composed of three layers: the amorphous PCL, crystal PCL, and amorphous PS layers. The cellulose backbone was thought to exist at the interface between the amorphous PCL and PS layers. Janus cellulosic bottlebrushes will open a new direction for the self-assembly of Janus bottlebrushes with new morphologies and functionalities owing to the cellulose inherent rigidity and helicity.

5-5. Acknowledgment

SAXS measurement was supported by the Joint Usage/Research Center (JURC) at the Institute for Chemical Research, Kyoto University, Japan.

5-6. References

1. Rzayev, J. Molecular Bottlebrushes: New Opportunities in Nanomaterials Fabrication. *ACS Macro Lett.* **2012**, *1*, 1146-1149.
2. Verduzco, R.; Li, X.; Pesek, S. L.; Stein, G. E. Structure, Function, Self-Assembly, and Applications of Bottlebrush Copolymers. *Chem. Soc. Rev.* **2015**, *44*, 2405-2420.
3. Pelras, T.; Mahon, C. S.; Mullner, M. Synthesis and Applications of Compartmentalised Molecular Polymer Brushes. *Angew. Chem., Int. Ed.* **2018**, *57*, 6982-6994.
4. Okamoto, Y. Chiral Polymers for Resolution of Enantiomers. *J. Polym. Sci., Part A: Polym. Chem.* **2009**, *47*, 1731-1739.
5. Chen, K.; Hu, X.; Zhu, N.; Guo, K. Design, Synthesis, and Self-Assembly of Janus Bottlebrush Polymers. *Macromol. Rapid Commun.* **2020**, *41*, 2000357.
6. Neugebauer, D.; Zhang, Y.; Pakula, T.; Matyjaszewski, K. Heterografted PEO-PnBA Brush Copolymers. *Polymer* **2003**, *44*, 6863-6871.
7. Gu, L.; Shen, Z.; Zhang, S.; Lu, G.; Zhang, X.; Huang, X. Novel Amphiphilic Centipede-Like Copolymer Bearing Polyacrylate Backbone and Poly(ethylene glycol) and Polystyrene Side Chains. *Macromolecules* **2007**, *40*, 4486-4493.
8. Li, Y.; Themistou, E.; Zou, J.; Das, B. P.; Tsianou, M.; Cheng, C. Facile Synthesis and Visualization of Janus Double-Brush Copolymers. *ACS Macro Lett.* **2011**, *1*, 52-56.
9. Bolton, J.; Rzayev, J. Tandem RAFT-ATRP Synthesis of Polystyrene–Poly(Methyl Methacrylate) Bottlebrush Block Copolymers and Their Self-Assembly into Cylindrical Nanostructures. *ACS Macro Lett.* **2011**, *1*, 15-18.
10. Li, H.; Miao, H.; Gao, Y.; Li, H.; Chen, D. Efficient Synthesis of Narrowly Dispersed Amphiphilic Double-Brush Copolymers through the Polymerization Reaction of Macromonomer Micelle Wmulsifiers at the Oil–Water Interface. *Polym. Chem.* **2016**, *7*, 4476-4485.
11. Xu, B.; Feng, C.; Huang, X. A Versatile Platform for Precise Synthesis of Asymmetric Molecular Brush in One Shot. *Nat. Commun.* **2017**, *8*, 333.

12. Nguyen, H. V.; Gallagher, N. M.; Vohidov, F.; Jiang, Y.; Kawamoto, K.; Zhang, H.; Park, J. V.; Huang, Z.; Ottaviani, M. F.; Rajca, A.; Johnson, J. A. Scalable Synthesis of Multivalent Macromonomers for ROMP. *ACS Macro Lett.* **2018**, *7*, 472-476.
13. Xu, B.; Qian, H.; Lin, S. Self-Assembly and Photoinduced Spindle-Toroid Morphology Transition of Macromolecular Double-Brushes with Azobenzene Pendants. *ACS Macro Lett.* **2020**, *9*, 404-409.
14. Burts, A. O.; Gao, A. X.; Johnson, J. A. Brush-First Synthesis of Core-Photodegradable Miktoarm Star Polymers via ROMP: Towards Photoresponsive Self-Assemblies. *Macromol. Rapid Commun.* **2014**, *35*, 168-173.
15. Stephan, T.; Muth, S.; Schmidt, M. Shape Changes of Statistical Copolymacromonomers: From Wormlike Cylinders to Horseshoe- and Meanderlike Structures. *Macromolecules* **2002**, *35*, 9857-9860.
16. Stepanyan, R.; Subbotin, A.; ten Brinke, G. Comb Copolymer Brush with Chemically Different Side Chains. *Macromolecules* **2002**, *35*, 5640-5648.
17. de Jong, J.; ten Brinke, G. Conformational Aspects and Intramolecular Phase Separation of Alternating Copolymacromonomers: A Computer Simulation Study. *Macromol. Theory Simul.* **2004**, *13*, 318-327.
18. Ishizu, K. Formation of Rodlike Nanocylinders by Binding of Prototype Copolymer Brushes with Polyelectrolytes. *Polym. Degrad. Stab.* **2005**, *90*, 386-389.
19. Ishizu, K.; Yamada, H. Architecture of Prototype Copolymer Brushes by Grafting-from ATRP Approach from Functionalized Alternating Comb-Shaped Copolymers. *Macromolecules* **2007**, *40*, 3056-3061.
20. Lian, X.; Wu, D.; Song, X.; Zhao, H. Synthesis and Self-Assembly of Amphiphilic Asymmetric Macromolecular Brushes. *Macromolecules* **2010**, *43*, 7434-7445.
21. Theodorakis, P. E.; Paul, W.; Binder, K. Interplay Between Chain Collapse and Microphase Separation in Bottle-Brush Polymers with Two Types of Side Chains. *Macromolecules* **2010**, *43*, 5137-5148.
22. Chang, H.-Y.; Lin, Y.-L.; Sheng, Y.-J.; Tsao, H.-K. Multilayered Polymersome Formed by Amphiphilic Asymmetric Macromolecular Brushes. *Macromolecules* **2012**, *45*, 4778-4789.
23. Luo, H.; Santos, J. L.; Herrera-Alonso, M. Toroidal Structures from Brush Amphiphiles. *Chem. Commun.* **2014**, *50*, 536-538.
24. Luo, H.; Szymusiak, M.; Garcia, E. A.; Lock, L. L.; Cui, H.; Liu, Y.; Herrera-Alonso, M. Solute-Triggered Morphological Transitions of an Amphiphilic Heterografted Brush Copolymer as a Single-Molecule Drug Carrier. *Macromolecules* **2017**, *50*, 2201-2206.

25. Palacios-Hernandez, T.; Luo, H.; Garcia, E. A.; Pacheco, L. A.; Herrera-Alonso, M. Nanoparticles from Amphiphilic Heterografted Macromolecular Brushes with Short Backbones. *Macromolecules* **2018**, *51*, 2831-2837.
26. Nam, J.; Kim, Y.; Kim, J. G.; Seo, M. Self-Assembly of Monolayer Vesicles via Backbone-Shiftable Synthesis of Janus Core–Shell Bottlebrush Polymer. *Macromolecules* **2019**, *52*, 9484-9494.
27. Li, Y.; Zou, J.; Das, B. P.; Tsianou, M.; Cheng, C. Well-Defined Amphiphilic Double-Brush Copolymers and Their Performance as Emulsion Surfactants. *Macromolecules* **2012**, *45*, 4623-4629.
28. Xie, G.; Krys, P.; Tilton, R. D.; Matyjaszewski, K. Heterografted Molecular Brushes as Stabilizers for Water-in-Oil Emulsions. *Macromolecules* **2017**, *50*, 2942-2950.
29. Xu, B.; Liu, Y.; Sun, X.; Hu, J.; Shi, P.; Huang, X. Semifluorinated Synergistic Nonfouling/Fouling-Release Surface. *ACS Appl. Mater. Interfaces* **2017**, *9*, 16517-16523.
30. Klemm, D.; Heublein, B.; Fink, H. P.; Bohn, A. Cellulose: Fascinating Biopolymer and Sustainable Raw Material. *Angew. Chem., Int. Ed. Engl.* **2005**, *44*, 3358-3393.
31. Kawamoto, K.; Zhong, M.; Gadelrab, K. R.; Cheng, L. C.; Ross, C. A.; Alexander-Katz, A.; Johnson, J. A. Graft-through Synthesis and Assembly of Janus Bottlebrush Polymers from A-Branch-B Diblock Macromonomers. *J. Am. Chem. Soc.* **2016**, *138*, 11501-11504.
32. Lanson, D.; Ariura, F.; Schappacher, M.; Borsali, R.; Deffieux, A. Comb Copolymers with Polystyrene and Polyisoprene Branches: Effect of Block Topology on Film Morphology. *Macromolecules* **2009**, *42*, 3942-3950.
33. Hou, C.; Hu, J.; Liu, G.; Wang, J.; Liu, F.; Hu, H.; Zhang, G.; Zou, H.; Tu, Y.; Liao, B. Synthesis and Bulk Self-Assembly of Well-Defined Binary Graft Copolymers. *Macromolecules* **2013**, *46*, 4053-4063.
34. Guo, Z. H.; Le, A. N.; Feng, X.; Choo, Y.; Liu, B.; Wang, D.; Wan, Z.; Gu, Y.; Zhao, J.; Li, V.; Osuji, C. O.; Johnson, J. A.; Zhong, M. Janus Graft Block Copolymers: Design of a Polymer Architecture for Independently Tuned Nanostructures and Polymer Properties. *Angew. Chem., Int. Ed.* **2018**, *57*, 8493-8497.
35. Cheng, L. C.; Gadelrab, K. R.; Kawamoto, K.; Yager, K. G.; Johnson, J. A.; Alexander-Katz, A.; Ross, C. A. Templated Self-Assembly of a PS- Branch-PDMS Bottlebrush Copolymer. *Nano Lett.* **2018**, *18*, 4360-4369.
36. Gray, D. G. Chemical Characteristics of Cellulosic Liquid Crystals. *Faraday Discuss. Chem. Soc.* **1985**, *79*, 257-264.
37. Crescenzi, V.; Manzini, G.; Calzolari, G.; Borri, C. Thermodynamics of Fusion of Poly-β-Propiolactone and Poly-ϵ-Caprolactone. Comparative Analysis of the Melting of Aliphatic Polylactone and Polyester Chains. *Eur. Polym. J.* **1972**, *8*, 449-463.

38. Nojima, S.; Ohguma, Y.; Kadena, K.-i.; Ishizone, T.; Iwasaki, Y.; Yamaguchi, K. Crystal Orientation of Poly(ε-caprolactone) Homopolymers Confined in Cylindrical Nanodomains. *Macromolecules* **2010**, *43*, 3916-3923.

Chapter 6

Near-Zero Azimuthal LC-Anchoring Correlated with Viscoelasticity on Bottlebrush-Coated Surface

6-1. Introduction

The alignment of liquid crystal (LC) can be intrinsically changed by external field such as electric and magnetic fields. This is the case in bulk but not at some interfaces: the mobility of the LC molecule at the interface is restricted by their interaction, which is called as anchoring effect. On the strong anchoring surface, the orientation of LC is fixed to the easy axis and not changed by external fields. Even in this case, however, the LC molecule apart from the interface can be aligned, and hence the external field stores an elastic energy between LC molecules on the interface and in bulk owing to their orientational gap. This energy can act as a driving force, which makes the alignment of LC in bulk back to the original one determined by the surface anchoring. Actually, this mechanism is widely used in current LC devices. Off course, any elastic energy is not induced, if the restriction of LC molecules at the surface is so weak to allow the orientational change the same as in bulk. Such weak anchoring is expected to provide a good platform to study fundamental properties of LC[1,2] and to develop an advanced LC device with high efficiency and responsiveness.[3] Especially, an in-plane isotropic surface with weak anchoring can achieve LC devices with memory properties.[4]

The degree of anchoring strength can be understood by two factors, zenithal anchoring strength (A_1) and azimuthal anchoring strength (A_2), which prescribe how easily the alignment of the LC molecule can be changed in the normal in-plane directions of the surface, respectively. In general, it is difficult to achieve weak anchoring, especially weak zenithal anchoring. Up to now,

it was reported that the surface modification by a liquid layer and a flexible oligomer/polymer layer could weaken the azimuthal anchoring strength.[5-10] The key to success is to shield the interaction between LC molecules and their strongly anchored solid surface. Among others, a polymer coating has an advantage in stabilizing such a so-called stealth layer and keeping it on the surface. However, weak anchoring had not been achieved in a wide range of temperatures.

Sato and coworkers investigated the LC-anchoring property on concentrated polymer brushes (CPB),[11] i.e., assemblies of densely end-grafted polymers and revealed the following features: (i) strong and weak anchoring was achieved at low and high temperatures on the CPB of poly (ethyl methacrylate) (PEMA)[12] and polystyrene,[13] (ii) at medium temperature, their response to external fields was viscoelastic, which is related to the concept of gliding anchoring,[14] and (iii) among others, the CPB of poly (hexyl methacrylate) (PHMA) showed near-zero azimuthal anchoring over a wide range of temperature.[12,15] This strongly suggests that the mobility of polymer layer should play an important role for LC anchoring, but the detail is still unclear.

In this chapter, the author aimed to reveal anchoring mechanism on a polymer layer. For this purpose, the author selected the coating layer of bottlebrushes because of the following reasons: (i) some bottlebrush films were reported to show a weak anchoring property similarly to the case of the corresponding CPB,[16] (ii) a thicker film can be prepared by controlling the amount of coating and the degree of crosslinking, and (iii) the mixture of (uncross-linked) bottlebrush and LC can be a good reference to evaluate viscoelastic properties, which is one of the most important points.

6-2. Experimental Section

6-2-1. Materials

Nematic liquid crystal JC-5051XX (JNC; a nematic–isotropic transition temperature,

T_{NI} = 112.7 °C) was used as LC. All other reagents were commercially available and used without further purification.

6-2-2. Synthesis and Characterization of Bottlebrushes

As shown in Scheme 1, the bottlebrushes studied in this chapter were synthesized from a macroinitiator, poly(2-(2-iodo-2-methylpropionyloxy)ethyl methacrylate) (200 mer; M_n = 4.2×10^4 and M_w/M_n = 2.1 determined as polystyrene-calibrated values by SEC) by the procedure of the reversible chain transfer catalyzed polymerization (RTCP) with iodide. As the side chain of bottlebrushes, two types of polymers, PHMA and PEMA, were introduced with and without cross-linkable terminal segment, which was given by the block copolymerization of 3-(methoxysilyl)propyl methacrylate (MOPS). A typical polymerization procedure was as follows. The macroinitiator (0.64 g, 2.0 mmol), monomer, hexyl methacrylate (HMA) or ethyl methacrylate (EMA) (293 mmol), and tetra n-butylammonium iodide (2.16 g, 5.85 mmol) were dissolved in diglyme (78.9 g). After the solution was purged with Ar gas, the polymerization was carried out at 80 °C for a prescribed time. In some cases, MOPS (0.46 g, 1.9 mmol) was added during the reaction for the block copolymerization. After the polymerization, the reaction mixture was diluted with THF (58.5 g), to which diethyl phosphonate (0.81 g, 5.9 mmol) was added and stirred at 60 °C for 1 h to remove iodide at the end of side chains. Then, the bottlebrush was recovered and purified via reprecipitation in methanol. The monomer conversion was estimated by gravimetry (not only after the polymerization but also before the addition of MOPS in the case of the block copolymerization). The content of MOPS at the block copolymerization was also determined from the nuclear magnetic resonance (NMR) spectra in $CDCl_3$ on JEOL JNS-ECS 400SS spectrometers (400 MHz; JEOL, Tokyo, Japan). The cross-linkable samples were stored as a solution of propyleneglycol monomethyl ether acetate (PGMEA).

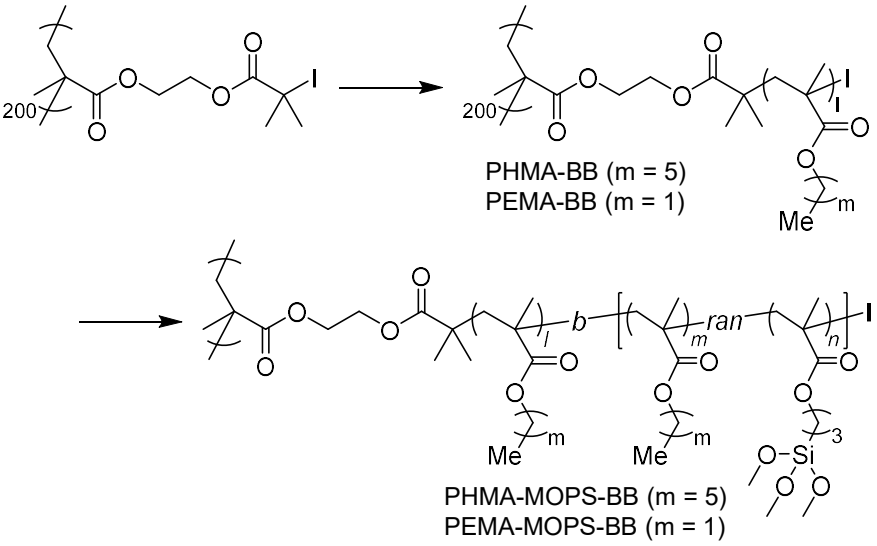

Scheme 6-1. Synthesis route and chemical structures of bottlebrushes.

The obtained bottlebrushes were further characterized by cutting off the side chain from the main chain and measuring its molecular weights by SEC. A typical cutting-off procedure is as follows. A bottlebrush sample (0.10 g) was dissolved in THF (0.75 g), to which NaOMe in MeOH (28 w%) (0.47 g) was added at room temperature. After the reaction for 4 d, the solution was neutralized with acetic acid, extracted with $CHCl_3$, and repeatedly washed with water. Finally, the organic phase was concentrated with evaporator and dried in vacuum oven at 60 °C overnight. After this treatment, the SEC chart gave no peak of the original bottlebrush but a new sharp peak in the lower-molecular-weight region, which was ascribed to the side chain. Thus, the degree of polymerization (DP_{meas}) and polydispersity index (PDI) of the side chain were estimated. The initiating efficiency (f) was given as the ratio of DP_{meas} to the DP calculated from the conversion (DP_{theo}). Table 6-1 summarizes the molecular characteristics of the studied bottlebrushes. It should be noted that the f value is higher for PEMA than for PHMA, which is reasonably understood because of a larger steric hindrance of HMA monomer. Almost equivalent bottlebrushes were obtained with and without cross-linkable segment, suggesting that PEMA-BB and PEMA-BB

could serve as model compounds of PHMA-MOPS-BB and PEMA-MOPS-BB.

SEC analysis of the purified product was carried out at 40 °C on a Shodex GPC-104 high-speed liquid chromatography system (Showa Denko K.K., Tokyo, Japan) equipped with a KF-G (Shodex) guard column, two KF-404 HQ (Shodex) columns, and an RI-74S differential refractometer (Shodex). Tetrahydrofuran (THF) was used as the eluent at a flow rate of 0.3 mL min^{-1}. PMMA standards were used to calibrate the SEC system.

Table 6-1. Molecular characteristics of bottlebrushes and their side chains.

sample	bottlebrush			Side chain				
	M_n[a] (g/mol)	PDI[a]	f_{MOPS}[b]	DP_{theo}[c]	DP_{meas}[d]	PDI[d]	f[e]	$f_{MOPSchain}$[f]
PHMA-BB	6.14×10^5	1.43	—	74	1.5×10^5	1.5	0.50	—
PHMA-MOPS-BB	6.21×10^5	1.55	5.4×10^{-4}	90	1.7×10^2	1.4	0.53	9.1×10^{-2}
PEMA-BB	4.74×10^5	1.57	—	85	1.0×10^2	1.5	0.82	—
PEMA-MOPS-BB	6.10×10^5	2.62	6.2×10^{-4}	84	1.1×10^2	1.5	0.78	6.7×10^{-2}

[a] Determined by GPC with PSt standard

[b] Calculated from ^{1}H NMR spectra.

[c] Calculated from Conversion.

[d] Determined by GPC with PMMA standard

[e] Initiation efficiency (DP_{theo}/DP_{meas})

[f] Fraction of side chain with MOPS segment ($f_{MOPS}\times DP_{meas}$)

6-2-3. Preparation and Characterization of the mixture of bottlebrush and LC

The bottlebrush and LC of different compositions were dissolved in a co-solvent, CH_2Cl_2, and dried in vacuum oven at 60 °C for 1.5 h to yield their mixtures. A mixture was put in between slide glasses with a spacer (cover glass; 0.12 ~ 0.17 mm in thickness) and observed by

POM (BX53, Olympus, Tokyo, Japan) equipped with camera (SPOT Idea CMOS 1.3MP, Cornes Technologies, Tokyo, Japan) to judge its mixing state. A mixture was also subjected to rheological measurements performed on MCR 302 (Anton Paar, GRAZ, Austria) with 8 mm parallel plate. Before measurement, the mixture was annealed at 140 °C between the plates. The measured frequency range was 0.01 to 100 rad/s. The obtained dynamic data with different temperature were corrected with shift factor a_T to construct a master curve with a reference temperature at 25 °C using time−temperature superposition principle.

6-2-4. Preparation and Characterization of cross-linked bottlebrush films

The cross-linkable bottlebrush with MOPS was spin-coated from its solution in propyleneglycol monomethyl ether acetate on a precleaned substrate, annealed at 210 °C for 15 min for cross-linking, subjected to the following experiments. The degree of swelling of the cross-linked film on a Si wafer by LC was evaluated by measuring the film thicknesses before and after swelling using Ellipsometer (M-2000 UL, J.A.Woollam Inc., Lincoln, Nebraska, USA) using the refractive index of PMMA. After the swelling equilibrium achieved by annealing the film with LC at 140 °C for 10 min, the surplus LC was removed, for the ellipsometric measurement, by standing the sample substrate upright at room temperature for PHMA bottlebrush and at 50 °C for PHMA bottlebrush for over than 30 min.

A twist anchoring coefficient of LC on the cross-linked film of bottlebrushes was measured using a LC cell shown in Figure 6-1. Two glass plates with a comb-shaped electrode and a rubbed polyimide (RPI) (JSR AL16301)-coated layer were separated with a gap d = 3 μm. The crosslinked bottlebrush layer was fabricated on the electrode plates. The rubbing direction of the RPI plate was tilted by 15° against the direction of the comb-shaped electrodes. After injecting

LC into the cell, the electro-optical properties were measured using an LCD-5200 (Otsuka Electronics): the rectangular tooth voltage with 60 Hz was applied from 0 V to 20 V.

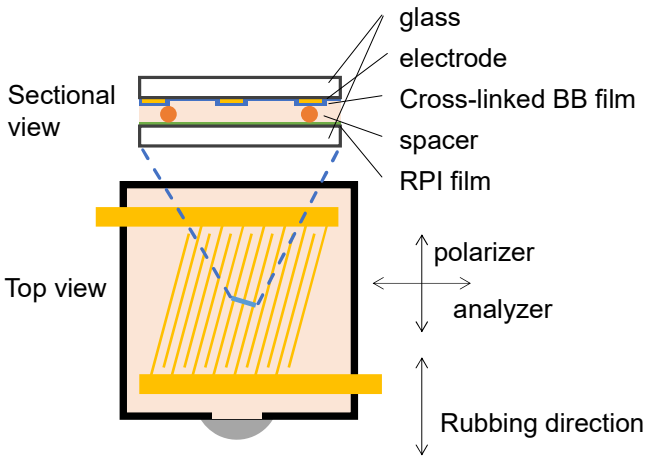

Figure 6-1. Schematic illustration of LC cell.

6-3. Results and Discussion.

6-3-1. Azimuthal Anchoring Strength of Cross-Linked Bottlebrush Films

The author measured the dependency of light transmittance on voltage of LC cell at different temperatures to evaluate the LC mobility (azimuthal anchoring coefficient, A_2) on cross-linked bottlebrush films. Before the measurement, the LC cell were annealed at 140 °C and cooled to room temperature in order to reset the effect of the LC-injection process and to homogeneously align the LC molecules along the rubbing direction. By this processing, the transmittance was zero under the cross-Nicol condition with the analyzer parallel to the rubbing direction. When the voltage is applied to the comb-shaped electrode, the torque occurs to align the LC molecule perpendicularly to the rubbing direction owing to the electric field. If the applied voltage exceeds a threshold voltage (V_{th}), the LC molecule starts to rotate. Because of the inverted electric field applied, the rotation angle of the LC director against the original direction increases with

increasing applied voltage. With rotating of the LC director, the transmittance firstly increases and then decreases because of rotation over the diagonal position under the cross-Nicol condition. Figure 6-2 shows the voltage-transmittance (*V*-*T*) curves obtained for the cross-linked film of PHMA-MOPS-BB and PEMA-MOPS-BB. Here, V_{th} was determined as the voltage at which the transmittance was 2% of the maximum transmittance.

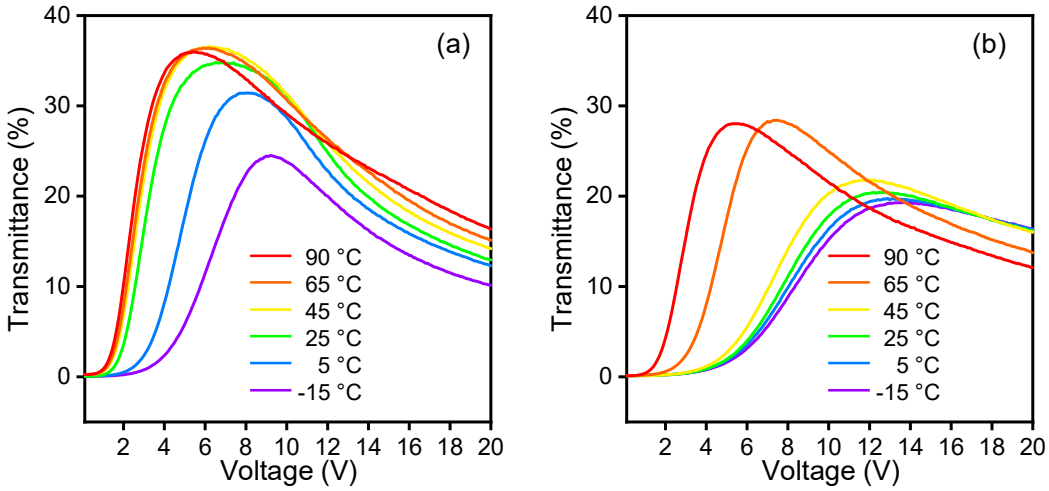

Figure 6-2. *V*-*T* curves for LC cell with cross-linked PHMA-MOPS-BB (a) and PEMA-MOPS-BB (b).

The value of V_{th} depends on the azimuthal anchoring coefficient (A_2) of the surface. The following relationships, Equations 6-1 and 6-2, were derived for the LC cell with both interfaces of strong anchoring[17] and that of weak anchoring,[18] respectively.

$$V_{\mathrm{th,RPI}} = \frac{\pi l}{d}\sqrt{\frac{K_2}{\varepsilon_0 \Delta\varepsilon'}} \tag{6-1}$$

$$V_{\mathrm{th}} = \frac{\pi l}{d + 2K_2/A_2}\sqrt{\frac{K_2}{\varepsilon_0 \Delta\varepsilon'}} \tag{6-2}$$

where l, d, K_2, ε_0 and $\Delta\varepsilon$' represent electrode distance, cell gap, twist elastic constant of LC, electric constant in space and the electric constant anisotropy, respectively. For the studied LC

cell with interfaces of weak and strong anchoring, the author applied the following equation on the analogy of Equations 6-1 and 6-1.

$$V_{\mathrm{th}} = \frac{\pi l}{d + K_2/A_2}\sqrt{\frac{K_2}{\varepsilon_0 \Delta\varepsilon'}} \tag{6-3}$$

Consequently, the A_2 value estimated by the following equation.

$$A_2 = \frac{K_2}{\left(V_{\mathrm{th,RPI}}/V_{\mathrm{th}} - 1\right)d} \tag{6-4}$$

Table 6-2 lists V_{th} experimentally determined and A_2 calculated from Equation 6-4 as well as K_2 data as a function of temperature.

Table 6-2. LC-anchoring characteristics on the surface of cross-linked bottlebrushes.

Temp (°C)	K_2 (pN)[a]	PHMA-MOPS-BB		PEMA-MOPS-BB	
		V_{th} (V)	A_2 (Jm^{-2})	V_{th} (V)	A_2 (Jm^{-2})
-15	7.9	2.70	3.6×10^{-6}	3.00	4.7×10^{-6}
5	7.5	2.20	2.2×10^{-6}	2.90	4.0×10^{-6}
25	6.9	1.40	9.8×10^{-7}	3.10	4.5×10^{-6}
45	6.5	1.10	6.6×10^{-7}	2.90	3.5×10^{-6}
65	6.0	1.10	6.1×10^{-7}	2.00	1.5×10^{-6}
90	5.5	1.00	5.0×10^{-7}	1.20	6.3×10^{-7}

[a] provided by JNC corporation.

Figure 6-3 shows the estimated A_2 values as a function of temperature for the cross-linked bottlebrush films. The A_2 for the PEMA system was almost constant below 25 °C and decreased with increasing temperature over 25 °C. On the other hand, the A_2 value for the PHMA system decreased in a lower temperature range and leveled off over 45 °C. These data possibly suggest that there exist two states of weaker and stronger anchoring depending on temperature and that its transition temperature is lower for the PHMA system than for the PEMA system. This trend is

similar to that for the corresponding CPBs of the same chemical species[12] except that the difference in A_2 was much larger, the reason for which is still unclear at present and a target of the future work. Anyhow, the author concluded that these two systems were good enough to discuss the mechanism of weak LC-anchoring because they gave the temperature-dependent A_2 in the studied range of temperature with different transition temperature.

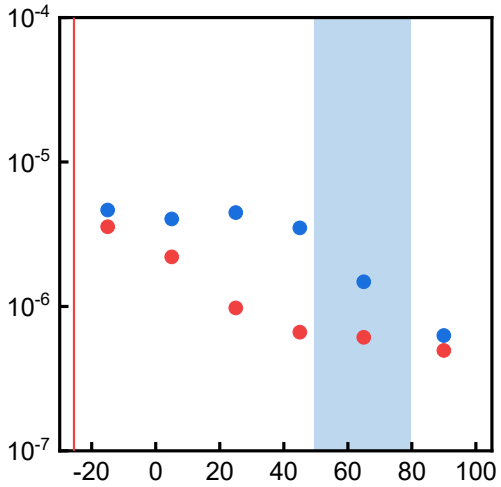

Figure 6-3. The dependency of A_2 on temperature for the thin films of PHMA-MOPS-BB (red circles) and PEMA-MOPS-BB (blue circles). The red line and blue band represent the characteristic temperature of the side-chain relaxation of PHMA-MOPS-BB and PEMA-MOPS-BB, respectively.

6-3-2. Miscibility of Bottlebrushes and LC

The degree of swelling of crosslinked film was determined. Figure 6-4 shows the relationship between the film thicknesses in a dry and swollen states. The proportional relationship indicates that the films were swollen by the LC with lateral uniformity and that the excessive LC was removed by the simple procedure described in Experimental section. From the slope of the lines in the figure, the degree of swelling was estimated to be 1.6 for PHMA-MOPS-BB and 1.2 for PEMA-MOPS-BB, which will be discussed in the next section.

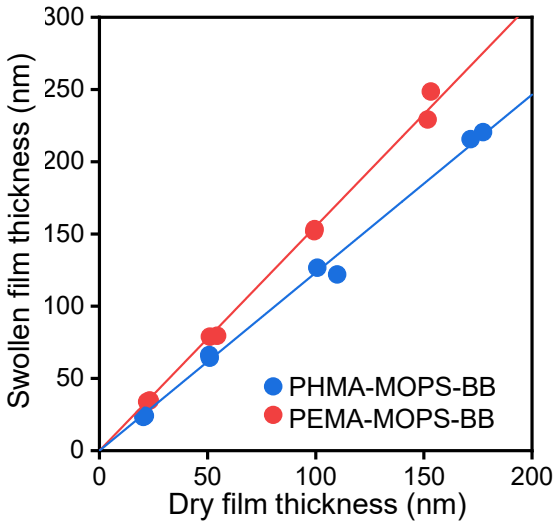

Figure 6-4. The relationship between swollen and dry cross-linked bottlebrush films.

In order to discuss the miscibility of the bottlebrushes and the LC, the author carried out the POM observation on the mixtures of (non-cross-linked) PHMA- or PEMA-BB and LC of different compositions. The phase states were clearly classified into two cases, i.e., a miscible state with optical isotropy and a phase-separated state with optical anisotropy. Figure 6-5 shows the phase diagram of the mixtures. At low LC compositions, neither phase separation nor light

transmittance was observed under open- and cross-nicol conditions, respectively, suggesting that the bottlebrush and the LC formed a homogeneous (miscible) mixture with a random orientation. On the other hand, at high LC compositions, a domain structure and a light transmittance, i.e., an optical anisotropy, were observed under open- and cross-nicol conditions, respectively. This strongly suggests that the mixtures were phase separated into two domains, i.e., a bottlebrush-rich phase and a LC-rich phase, the latter of which is in a LC state. The difference in the LC composition of phase boundary between PHMA- and PEMA-BB was attributed to the higher affinity of the former. In Figure 6-5, the green circular symbols represent the LC compositions of the swollen cross-linked film, which were calculated from the swelling ratio (given by Figure 6-4) and the density of LC and linier PHMA and PEMA (instead of PHMA- and PEMA-BB). These compositions are located in a homogeneous and isotropic phase near the phase boundary. This suggests that the cross-linked bottlebrush film was swollen by the LC with the degree, which was mainly controlled by its chemical composition but not much limited by cross-linking. In other words, the studied bottlebrushes were reasonably understood to be slightly crosslinked so as to hardly restrict the chain mobility and to keep the original molecular characteristics, as expected because the molar fraction of MOPS unit of the cross-linkable bottlebrushes was as low as approximately 0.1 %.

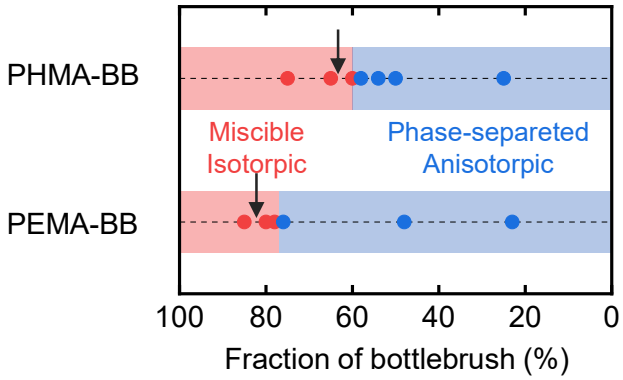

Figure 6-5. The phase diagram of the mixture of bottlebrush and LC. The red circles represent that the mixture was homogeneous and not birefringent. The blue circles represent that the mixture was inhomogeneous and birefringent. The arrows represent the weight fraction of bottlebrush in the swollen cross-linked bottlebrush film.

6-3-3. Rheological Properties of the Mixtures of Bottlebrushes and LC

LC anchoring including gliding anchoring on a polymer-coated surface was expected to depend on the reorientation of polymer chains. In order to clarify the anchoring mechanism, therefore, it is very important to understand the rheological property of the polymer-coated layer as it is. However, the crosslinked film in this study was too thin to carry out the rheological measurement. Fortunately, as discussed in the above section, the studied cross-linked system was reasonably assumed to be equivalent to the mixture of (uncross-linked) bottlebrushes and LC of the same composition at least in local and/or segmental dynamics, on which the author will focus. Consequently, the author carried out the rheological measurements on the mixture of bottlebrush without MOPS and LC of the same composition as the LC-swollen film of cross-lined bottlebrushes.

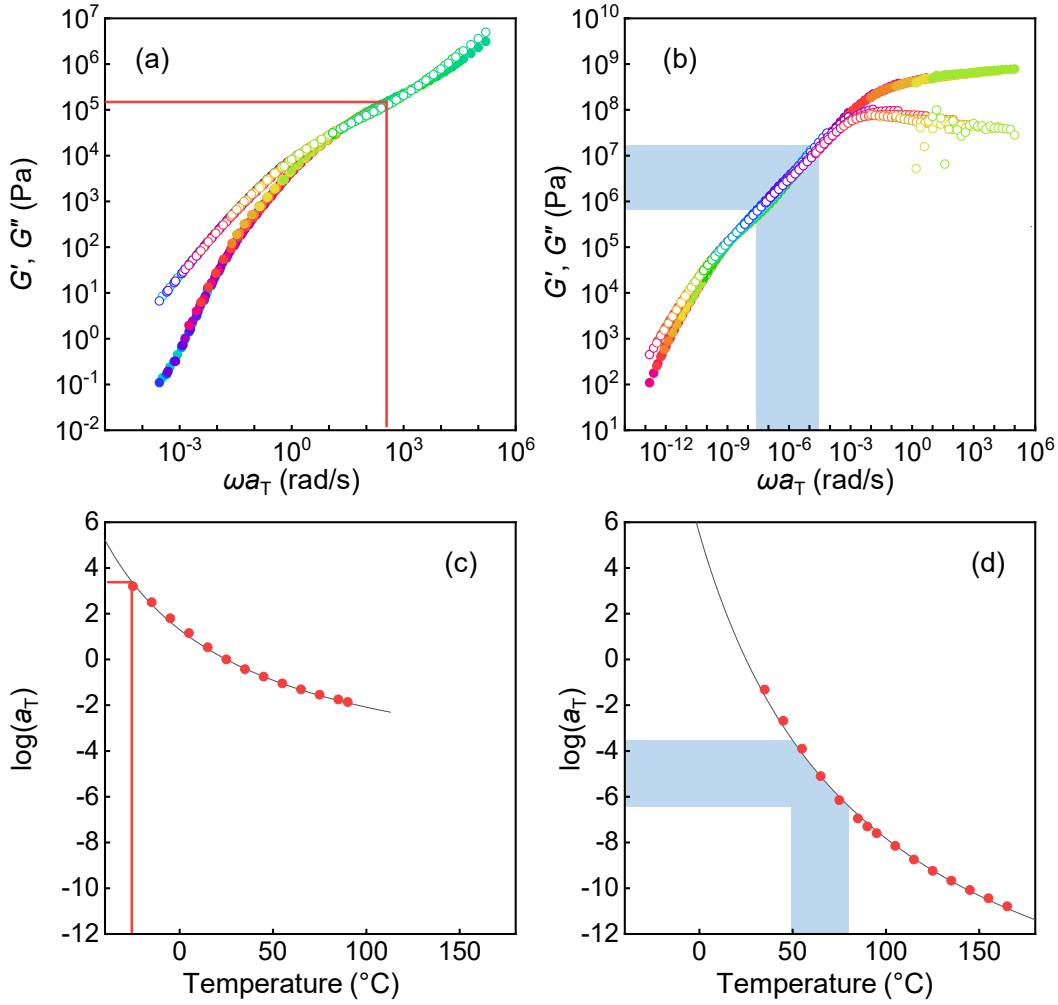

Figure 6-6. Master curves of G' and G" and temperature dependency of shift factor a_T for the mixture of PHMA-BB (a, c) and PEMA-BB (b, d) with LC: the LC composition was 63 w% and 82 w%, respectively.

Figure 6-6 shows the temperature-dependent dynamic viscoelastic data for the mixtures. Well-defined master curves were obtained at a reference temperature of 25 °C, similarly to the bulk bottlebrush system in its shape. This means that the mixture gave little drastic change of miscibility and LC anisotropy in the studied range of temperature. The viscoelastic property of a bottlebrush was expected to be characterized by sequential relaxation modes from the glassy state to the terminal flow, being assigned to the dynamics of side- and whole-chains of a bottlebrush in

addition to the glass transition. Therefore, the viscoelastic master curve should be divided into the segmental, arm, and terminal regimes. As for the PEMA system, a glassy regime was obviously observed at high frequency region. The PHMA system was more flexible, as was expected because the PHMA system has a lower T_g in bulk of the polymer segment constituting the bottlebrush as well as a higher LC composition. In Figure 6-6, the plateaus assignable to the relaxations other than the glass transition were not obvious. In order to discuss these relaxation modes in a larger scale, the author carried out van Gurp–Palmen analysis:[19,20] van Gurp–Palmen plot, i.e., the plot of tan δ versus storage modulus, could provide the plateau modulus of these modes as a minimum.[21,22] Figure 6-7 shows the Gurp–Palmen plot for the data measured at different temperatures frequencies (plotted in Figure 6-6). The data for the PHMA system at different temperatures gave a well-overlapped master curve with a single minimal point. A single minimal point was observed also for the PEMA system but incompletely overlapped at different temperatures. Figure 6-7 shows the G' value at the minimal point as a function of temperature. The exact reason for the temperature dependency is still unclear, but the glass transition may affect the side-chain dynamics because these two modes are very closely located.[23] Finally, the author ascribed the minimal point to the dynamics of the side chain of bottlebrushes. The G' value at the minimal point, i.e., the plateau modulus of the side-chain relaxation was estimated to be 1.3×10^5 Pa and 6.6×10^5 - 1.7×10^7 Pa for the PHMA and PEMA systems, respectively. These data are reasonably lower than that in the glassy state (1×10^9 Pa clearly observed for the PEMA system). The difference in the plateau modulus of the side-chain relaxation between the two system is reasonably understood since the PHMA system has a higher LC composition and a constituted polymer segment of a lower T_g. It should be noted that in these systems, the relaxation mode of whole bottlebrush chain was not obviously observed. This is presumably because the main-chain length (the degree of polymerization of main chain = 200) is not so large as compared

with the side-chain length (DP_{meas} = 171 of PHMA-BB and 108 of PEMA-BB), suggesting a more or less star-like conformation for the bottlebrushes.[23]

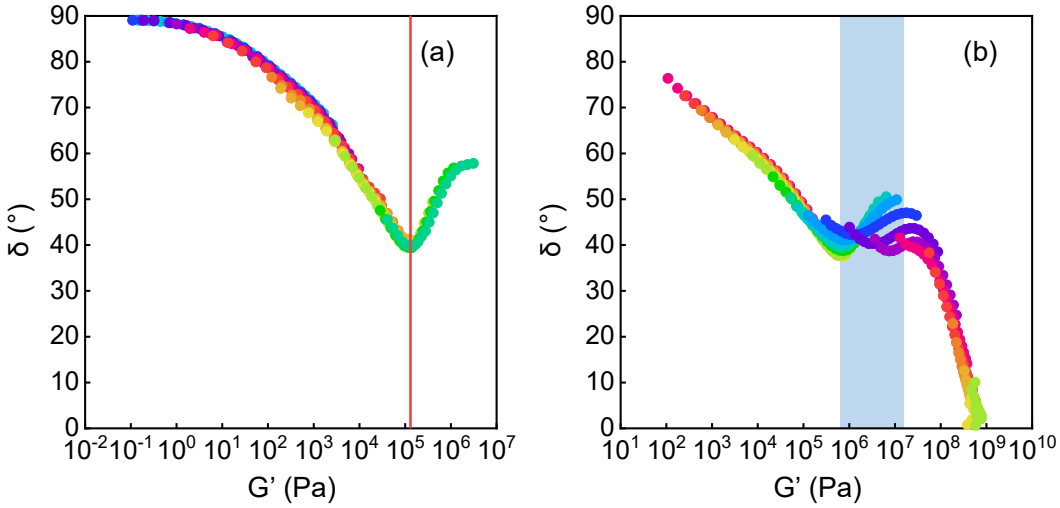

Figure 6-7. Van Gurp–Palmen plot for the mixture of LC and PHMA-BB (a) and PEMA-BB (b). the first derivative of the phase angle respect to the storage modulus for the mixture of LC and PHMA-BB (c) and PEMA-BB (d).

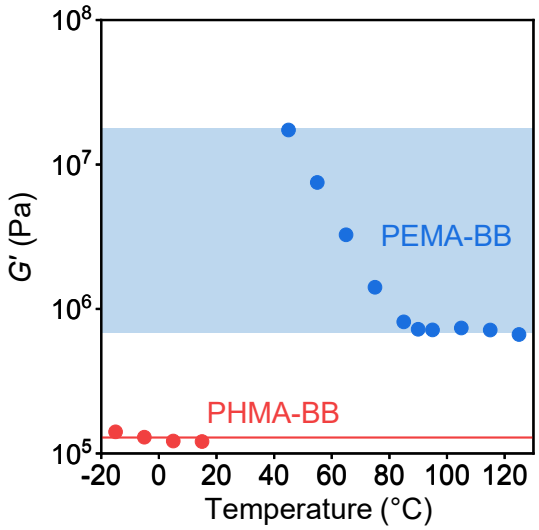

Figure 6-8. Temperature dependence of G' value at minimal point in van Gurp–Palmen plot for the PHMA and PEMA systems.

6-3-4. Correlation between LC anchoring and bottlebrush dynamics

Concerning two types of cross-linked bottlebrush films, their temperature-dependent A_2 (shown in Figure 6-3) were insufficiently correlated with their G' and G'' values as well as the glass transition temperature. Therefore, the author more focuses on their side-chain dynamics, which was clarified in the previous section, and attempts to evaluate the corresponding characteristic temperature via the a_T parameter and to compare it with the temperature-dependent A2. From the plateau modulus of the side-chain relaxation, the corresponding ωa_T and hence a_T values were estimated for the PHMA and PEMA systems as shown by lines and bar in Figure 6-6a and b. Here, the author set 0.1 rad/s for ω corresponding to the measurement of LC anchoring by assuming $\omega = 2\pi/t_{max}$, where t_{max} is the time taken to achieve the maximum transmittance in Figure 6-2. Then, the characteristic temperature of the side-chain relaxation was given as −26 °C and 50 - 81 °C for the PHMA and PEMA systems, respectively (Figure 6-6c and d). These temperatures are also shown by line and band in Figure 6-3. The author concluded that the

estimated characteristic temperature of side-chain relaxation was reasonably correlated with the temperature range of A_2 decreasing. This means that weak anchoring property of the bottlebrush film was mainly understood as the gliding anchoring enhanced by the side-chain motion.

6-4. Conclusions

In this section, the author revealed the temperature-dependent A_2 on two types of cross-linked bottlebrushes similarly to the corresponding CPB. The temperature range of A_2 decreasing was lower for the PHMA system than for the PEMA system. For better understanding of such anchoring mechanism, the swollen and crosslinking state of the cross-linked bottlebrushes by the LC molecule was firstly investigated also using the mixtures of (uncross-linked) bottlebrushes and LC as references, suggesting that the bottlebrushes are slightly crosslinked with keeping their original characters in affinity with LC and possibly in dynamics of side-chain relaxation. This means that the mixtures of (uncross-linked) bottlebrushes with the same LC composition were sufficiently good reference systems for the cross-linked system. Then, the viscoelastic data were obtained for the reference mixtures to discuss the LC-anchoring mechanism from the viewpoint of chain dynamics. The author successfully applied van Gurp–Palmen analysis to clarify the side-chain relaxation mode and estimated its characteristic temperature for the PHMA and PEMA systems by assuming the frequency corresponding to the LC-anchoring measurements. Finally, the author found a good correlation between the temperature dependency in A2 and the side-chain relaxation and concluded that the bottlebrushes slightly swollen by LC molecule plays an important role not only in decreasing the interaction with the LC molecule but also in enhancing the gliding anchoring by side-chain dynamics. This understanding is expected to provide a newly designed concept of highly functionalized polymer coating toward a next-generation LC display and other applications.

6-5. Acknowledgment

All bottlebrushes were kindly supplied by Dainichiseika Color & Chemicals Mfg. Co., Ltd., Tokyo, Japan. The *V-T* curve measurement with LC cell was carried out in LG Japan lab co. (Tokyo, Japan). The author thanks Dr. Osamu Sato (Japan Advanced Institute of Science and Technology) for advice on *V-T* curve measurement,

6-6. References

1. Blanc, C.; Svensek, D.; Zumer, S.; Nobili, M. Dynamics of Nematic Liquid Crystal Disclinations: the Role of the Backflow. *Phys. Rev. Lett.* **2005**, *95*, 097802.
2. Stoenescu, D. N.; Nguyen, H. T.; Barois, P.; Navailles, L.; Nobili, M.; Martinot-Lagarde, P.; Dozov, I. Optical Studies of Chiral Mesophases in Sandwich Cells with Planar Degenerated Anchoring. *Mol. Cryst. Liq. Cryst.* **2006**, *358*, 275-286.
3. Nie, X.; Lu, R.; Xianyu, H.; Wu, T. X.; Wu, S. T. Anchoring Energy and Cell Gap Effects on Liquid Crystal Response Time. *J. Appl. Phys.* **2007**, *101*, 103110.
4. Yamamoto, J.; Yokoyama, H.; Watanabe, J. Zero Surface Anchoring the Liquid Crystal Alignment Method and a Liquid Crystal Device. JP4053530B2, April 21, 2007.
5. Bryan-Brown, G. P.; Wood, E. L.; Sage, I. C. Weak Surface Anchoring of Liquid Crystals. *Nature* **1999**, *399*, 338-340.
6. Ramdane, O. O.; Auroy, P.; Forget, S.; Raspaud, E.; Martinot-Lagarde, P.; Dozov, I. I. Memory-Free Conic Anchoring of Liquid Crystals on a Solid Substrate. *Phys. Rev. Lett.* **2000**, *84*, 3871-3874.
7. Nespoulous, M.; Blanc, C.; Nobili, M. Ultraweak azimuthal anchoring of a nematic liquid crystal on a planar orienting photopolymer. *J. Appl. Phys.* **2007**, *102*, 073519.
8. Oswald, P.; Dequidt, A.; Zywocinski, A. Sliding Planar Anchoring and Viscous Surface Rorque in a Cholesteric Liquid Crystal. *Phys. Rev. E* **2008**, *77*, 061703.
9. Dozov, I.; Stoenescu, D. N.; Lamarque-Forget, S.; Martinot-Lagarde, P.; Polossat, E. Planar Dgenerated Anchoring of Liquid Crystals Obtained by Surface Memory Passivation. *Appl. Phys. Lett.* **2000**, *77*, 4124-4126.
10. Rijeesh, K.; Higuchi, H.; Okumura, Y.; Yamamoto, J.; Kikuchi, H. Liquid Crystal Anchoring Transitions and Weak Anchoring Interface Formation at Surfaces Created by Uniquely Designed Acrylate Copolymers. *Polymer* **2017**, *116*, 447-451.

11. Tsujii, Y.; Ohno, K.; Yamamoto, S.; Goto, A.; Fukuda, T. Structure and Properties of High-Density Polymer Brushes Prepared by Surface-Initiated Living Radical Polymerization. In *Surface-Initiated Polymerization I*, Jordan, R., Ed. Springer: Berlin, Heidelberg, 2006; pp 1-45.
12. Sato, O.; Iwata, N.; Kasai, T.; Tsujii, Y.; Kang, S. M.; Watanabe, J.; Tokita, M. Nematic Liquid Crystal Anchoring Strengths of High Density Polymer Brush Surfaces. *Liq. Cryst.* **2015**, *42*, 181-188.
13. Sato, O.; Kasai, T.; Nomura, A.; Tsujii, Y.; Kang, S.; Tokita, M.; Watanabe, J. Viscoelastic PS Brush Surface Offering Strong Anchoring at Low Temperature and Near-Zero Anchoring at High Temperature for LC Molecules. *Liq. Cryst.* **2012**, *40*, 221-227.
14. Janossy, I. Kinetics of Director Gliding on a Polymer-Liquid-Crystal Interface. *Phys. Rev. E* **2010**, *81*, 031714.
15. Sato, O.; Kasai, T.; Sato, M.; Sakajiri, K.; Tsujii, Y.; Kang, S.; Watanabe, J.; Tokita, M. High-Density Poly(hexyl methacrylate) Brushes Offering a Surface for Near-Zero Azimuthal Anchoring of Liquid Crystals at Room Temperature. *J. Mater. Chem. C* **2013**, *1*, 7992-7995.
16. Sato, O.; Okuno, H.; Adachi, I.; Watanabe, J.; Tokita, M.; Sakakibara, K.; Kinose, Y.; Goto, A.; Tsujii, Y. Novel In-Plane Switching Liquid Crystal Display with an Extremely High Transmittance Using a Well-Designed Bottlebrush as a Zero-Azimuth Anchoring Material. *Jpn. J. Appl. Phys.* **2019**, *58*, 066503.
17. Oh-e, M.; Kondo, K. Electro-Optical Characteristics and Switching Behavior of the In-Plane Switching Mode. *Appl. Phys. Lett.* **1995**, *67*, 3895-3897.
18. Yoneya, M.; Iwasaki, K.; Tomioka, Y.; Kondo, K. Cell Gap Margin Enlargement of In-Plane Switching Mode Liquid Crystal Displays Using Weak-Anchoring Effects. *Appl. Phys. Lett.* **1999**, *74*, 803-805.
19. Trinkle, S.; Friedrich, C. Van Gurp-Palmen-Plot: a Way to Characterize Polydispersity of Linear Polymers. *Rheol. Acta* **2001**, *40*, 322-328.
20. Trinkle, S.; Walter, P.; Friedrich, C. Van Gurp-Palmen Plot II - Classification of Long Chain Branched Polymers by Their Topology. *Rheol. Acta* **2002**, *41*, 103-113.
21. Alexandris, S.; Peponaki, K.; Petropoulou, P.; Sakellariou, G.; Vlassopoulos, D. Linear Viscoelastic Response of Unentangled Polystyrene Bottlebrushes. *Macromolecules* **2020**, *53*, 3923-3932.
22. Hu, M.; Xia, Y.; McKenna, G. B.; Kornfield, J. A.; Grubbs, R. H. Linear Rheological Response of a Series of Densely Branched Brush Polymers. *Macromolecules* **2011**, *44*, 6935-6943.
23. Dalsin, S. J.; Hillmyer, M. A.; Bates, F. S. Linear Rheology of Polyolefin-Based Bottlebrush Polymers. *Macromolecules* **2015**, *48*, 4680-4691.

Chapter 7

Time Dependent and LC Anchoring and Bottlebrush Polymer Dynamics Revealed by High-Speed Polarized Microscopy

7-1. Introduction

In bulk the liquid crystal (LC) molecule rotates according to external fields and changes its orientation. However, the mobility of LC molecule on surface is suppressed by the interaction between LC molecules and surface, which is called as anchoring effect. On strong anchoring surface, the LC molecule is fixed and could not rotate. On the contrary, on zero anchoring surface, as the limiting case of weak anchoring, the rotation of LC molecule on surface is not restricted and the easy axis changes.[1-5] Controlling anchoring strength is important to assemble LC device since it affects the responsibility of LC in bulk to the external field.

Generally, the strong anchoring surface is utilized in commercial LC device. On the other hand, offering weak anchoring surface is still in an investigational stage. Sato and coworkers demonstrated the concentrated polymer and cross-linked bottlebrush film consisting mainly of poly(hexyl methacrylate) (PHMA) (PHMA-BB) could offer weak azimuthal anchoring surface.[6-8] In chapter 6, the author investigated the mechanism of cross-linked bottlebrush film offering weak anchoring from the viewpoint of chain dynamics. As a result, it is revealed that the azimuthal anchoring strength (A_2) is constant below the temperature range of the relaxation of side chain of bottlebrush[9,10] where A_2 decrease with increasing temperature. This indicated that the mobility of LC molecule on bottlebrush film depend on multiple relaxation mode, such as the relaxation associated with side chain and viscosity of LC.

In this chapter, the author observed the response of transmittance of LC cell with cross-

linked PHMA bottlebrush to stepwise applying electric field with high-speed camera equipped in microscope. Strictly speaking, the torque on LC molecules is differ depending on area because the electric field is lateral and vertical direction between electrode and on electrodes, respectively. The observations with microscope have an advantage that it could isolate the lateral rotation detect since it could distinguish the area on and between electrodes, while the macroscopic observation of LC device detects lateral and vertical rotation of LC. Note, in this chapter, the author analyzed the change in transmittance without extracting LC between electrodes. The obtained data of time evolution was analyzed by relaxation function. As reference, the LC with cross-linked bottlebrush consisting mainly of poly(methyl methacrylate) (PMMA) (PMMA-BB) was observed, too. Then, the relaxation modes were discussed from viewpoint of side chain dynamics.

7-2. Experimental Section

7-2-1. Materials

Nematic liquid crystal JC-5051XX (JNC Corporation, Tokyo, Japan; a nematic–isotropic transition temperature, T_{NI} = 112.7 °C and refractive index anisotropy Δn = 0.081) was used as LC. The in-plane switching LC cell configuration was same to the cell used in chapter 6. The crosslinked bottlebrush layer was fabricated with PHMA-MOPS-BB or PMMA-MOPS-BB (Table 7-1) synthesized in the same scheme in chapter 6. Figure 7-1 displays the estimated dependency of A_2 on temperature calculated from equation 6-4 with data of LC cell with PHMA-BB and PMMA-BB measured with a LC display evaluation system (LCD-5200, Otsuka Electronics Co., Ltd., Osaka, Japan). The author expect that the cross-linked PMMA bottlebrush film and LC formed a homogeneous (miscible) mixture with a random orientation in the swollen PMMA bottlebrush film alike poly(ethyl methacrylate) (PEMA) system in chapter 6.

Table 7-1. Molecular characteristics of bottlebrush.

sample	M_n[a] (g/mol)	PDI[a]	DP_{theo}[b]
PHMA-MOPS-BB	7.07×10^5	2.34	88
PMMA-MOPS-BB	2.82×10^5	1.77	19

[a] Determined by GPC with polystyrene standard

[b] Degree of polymerization calculated from Conversion.

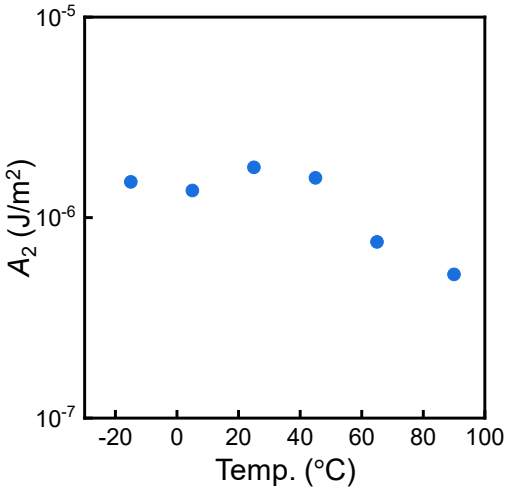

Figure 7-1. The dependency of A_2 on temperature for the thin films of PMMA-MOPS-BB.

7-2-2. Instrumentation and Measurements

Figure 7-2 show the schematic illustration of experimental set up. The change in the transmittance of LC cell was recorded by polarized optical microscope (BX53, Olympus, Tokyo, Japan) equipped with a halogen light source (U-LH100-3, Olympus) and a high-speed camera (MEMORECAM Q1m, NAC image technology, Tokyo, Japan). The exposure time was set to 0.5 ms. When the LC cell was heated in a hot stage (HS82, Mettler Toledo, Ohio, United States) with a temperature control unit (HS1, Mettler-Toledo), the exposure time was set to 4 ms. The voltage

(10 Vp-p, 60 Hz, square wave) was applied to LC cell by a function generator (WF1974, NF Corporation, Kanagawa, Japan).

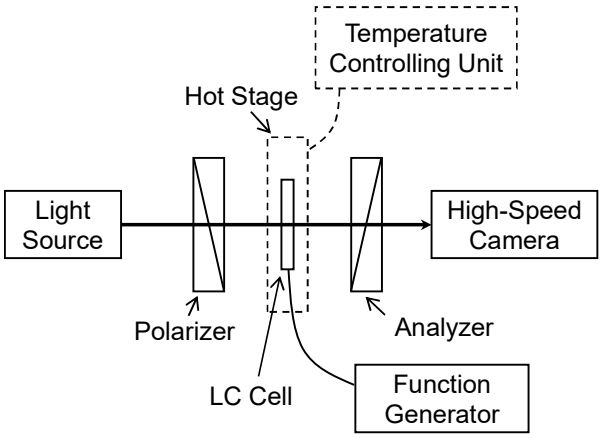

Figure 7-2. Schematic illustration of the experimental setup.

7-3. Results and Discussion

In Figure 6-3, the dependency of LC cell with cross-linked bottlebrush on temperature exhibit the intriguing curves: The A_2 for the PEMA system was almost constant below 45 °C and decreased with increasing temperature over 45 °C; the A_2 value for the PHMA system decreased in a lower temperature range and leveled off over 45 °C. From this data as well as Figure 7-1, the author proposed the unified anchoring model on bottlebrush film: the A_2 value is constant at lower temperature, which is mainly determined the viscous LC and the interaction between LC molecules and swollen bottlebrush film with frozen side chain (corresponding to the PEMA and PMMA system below 25 and 45 °C, respectively); the A_2 value decrease with temperature, which is related with the relaxation of side chain of the bottlebrush film (corresponding to PHMA system below 45°C, and PEMA and PMMA system over 25 and 45 °C, respectively); the A_2 value is level off, which is associated with bottlebrush film with highly mobile side chain (corresponding to PHMA system over 45°C) (Figure 6-2). Therefore, the mobility of LC on the bottlebrush film

may reflect the multiple relaxation mode of LC and the swollen bottlebrush films with LC.

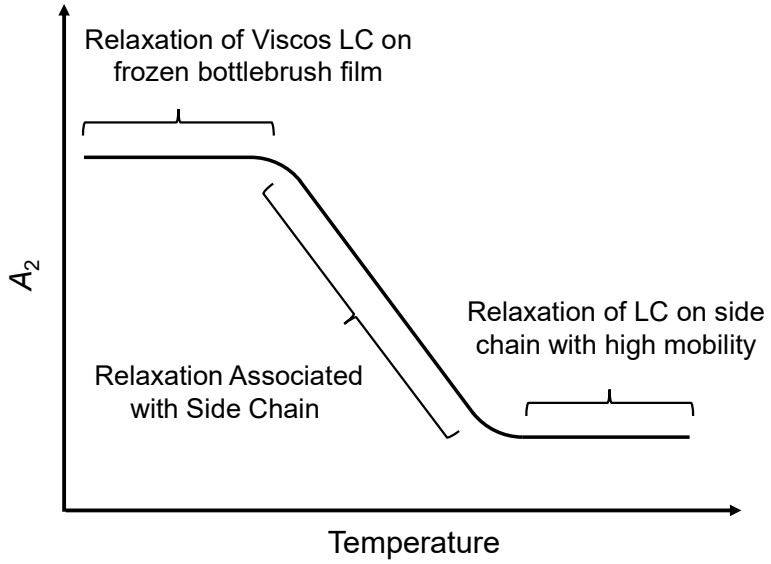

Figure 7-3. schematic illustration of relaxation mode of LC on bottlebrush

Figure 7-4 shows the time evolution of the transmittance of LC cell with PHMA-MOPS-BB and PMMA-MOPS-BB coat at different temperatures. LC cell with PHMA at 90 °C, after the voltage of 5V was applied, the transmittance started to increase and reached to maximum, then slightly decreased to level out. This may be because in LC cell with PHMA-MOPS-BB at 90 °C, the LC molecule twisted too much, and the retardation exceeded the level which makes the transmittance maximum. This is supported by *V-T* curve for the LC cell with PMMA at 90 °C where the transmittance almost reached the maximum at voltage 5V (Figure 6-2). On the other hand, in PHMA system at 45 °C and PMMA system, the transmittance monotonically increased and approached asymptotically to constant value. Thus, it was assumed that the LC in those sample did not reach to the retardation which makes the transmittance maximum. In the PHMA system at 15 and 25 °C, the transmittance gradually was increasing 1 s after stepwise applying electric field, which is attributed to the rotating easy axis. Note that the transmittance could not been compared between the experiment with and without a hot stage because the light intensity

and the exposure time of camera were different.

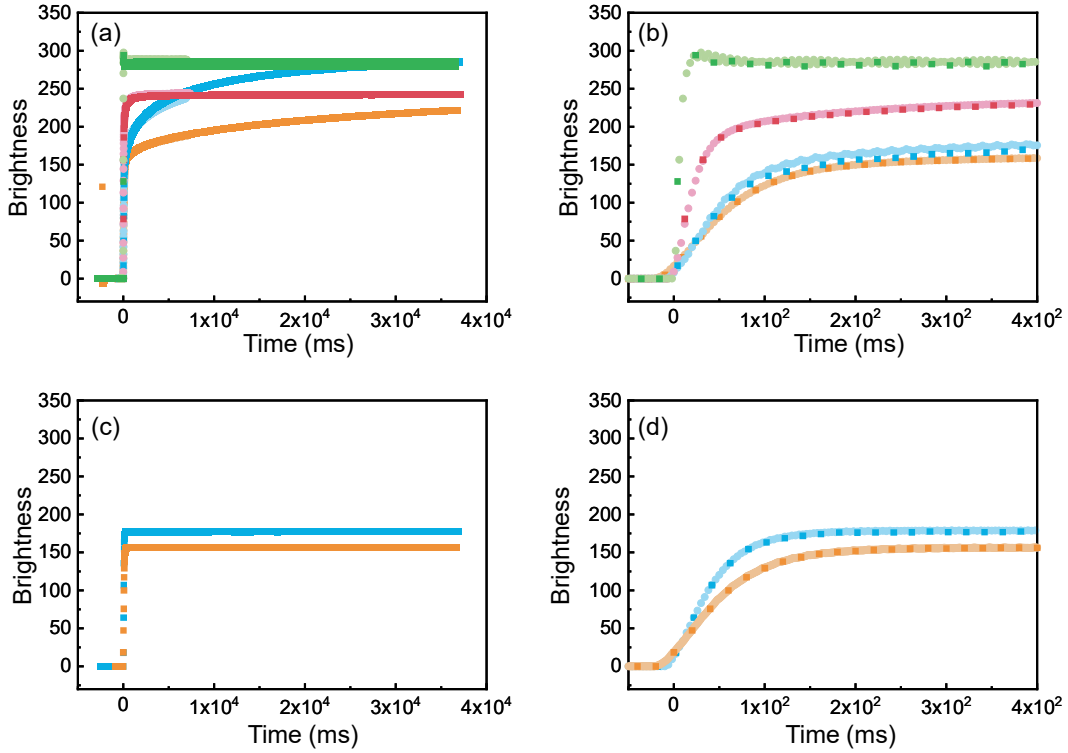

Figure 7-4. Time evolution of the transmittance of LC cell (yellow, bule red and green dots represent the data at 15, 25, 45 and 90 °C; in b and d, the dots with pale color represent the data of 250 frames per second, and the other dot represent data of 50 frame per second)

The time evolution of transmittance was analyzed with the following multiple-exponential function.[5]

$$C = C_{total} \sum C_i \left(1 - e^{t/\tau_i}\right) \tag{7-1}$$

where, C_{total}, C_{i}, τ_{i} and t represent the transmittance, the fraction of relaxation mode, relaxation time and time.

Concerning LC cell with PMMA system, the data was approximated to the single exponential. On the other hand, the data of PHMA system was not represented by single nor double but triple exponential function. As for data for LC cell with PHMA at 90 °C was tentatively

fitted by doble exponential function (Figure7-5). Table 7-2 shows the parameters.

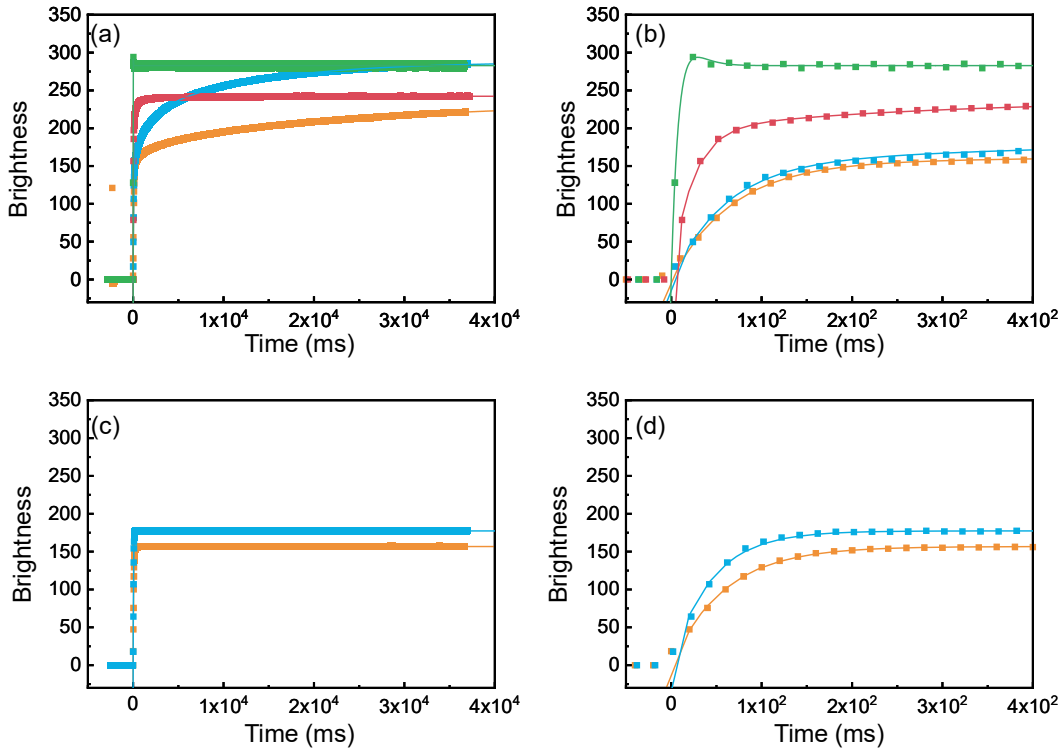

Figure 7-5. Relaxation function of response to stepwise applying electric field. Yellow, bule red and green dots represent the data at 15, 25, 45 and 90 °C (a and b, PHMA system: c and d, PMMA system).

Table 7-2. Coefficient and time constant of response for

	Temp. (ºC)	C_{total}	C_1	τ_1 (ms)	C_2	τ_2 (ms)	C_3	τ_3 (ms)
PHMA-MOPS-BB	15	234	0.66	6.6×10	0.084	1.9×10^3	0.25	2.3×10^5
	25	288	0.54	6.1×10	0.20	1.6×10^3	0.254	1.2×10^5
	45	242	0.81	2.3×10	0.16	2.7×10^2	0.019	4.5×10^4
	90	—	—	(1.1×10)	—	(1.1×10)	—	—
PMMA-MOPS-BB	15	157	1	5.8×10	—	—	—	—
	25	177	1	4.3×10	—	—	—	—

As with PEMA system, the dependency of A_2 on temperature for the PMMA system at 15 and 25 °C exhibit the constant region, which indicating that the side chains are in glass state (Figure 7-1). Consequently, the τ_1 value for PMMA system corresponded to the relaxation mode of viscous LC on the swollen bottlebrush film with randomly oriented LC. As for PHMA system, its exhibit the τ_1 value comparable to for the τ_1 value for PMMA, indicating that this relaxation corresponds to that of PMMA system. Thus, as for PHMA system, the author considered that residual relaxation modes with relaxation mode with longer time scale, τ_2 and τ_3, are derived from viscous properties of the swollen bottlebrush film with LC, for example the relaxation of the side chains of bottlebrush. They could not be negligible in long time scale, though those relaxation modes do not affect the orientation of LC immediately after stepwise applying electric field. In chapter 6, the anchoring strength is estimated form the data obtained by LC display evaluation system (LCD 5200). In this system, the electric field gradually increases (in the order of 10 – 100 s) and the threshold voltage, at which the transmittance start to increase, is detected. Thus, the A_2 in chapter 6 is considered that to reflect the relaxation modes with long as well as long time scale on surface. The value τ_1, τ_2 and τ_3, in the LC cell with PHMA, and τ_1 in the LC cell with PEMA

decreased as temperature increased (Table 7-2, Figure 7-6), which indicating that in PHMA system at 45 °C, the easy axis changed (possibly corresponding to τ_2 and τ_3) immediately after stepwise applying electric fields. From above results, the author concluded that this measurement method of transmittance with high-speed camera and stepwise applying electric field enable to obtain the relaxation modes with a wide range of time scale and the anchoring properties associated to them.

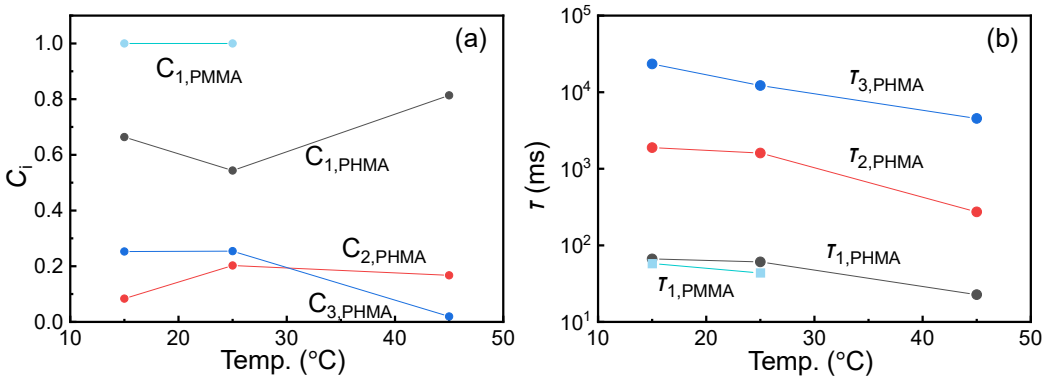

Figure 7-6. The dependency of C_i and τ_i on the temperature (a) and the dependency of C_i and τ_i on the temperature (b)

7-4. Conclusions

In this section, the author observed time evolution of transmittance LC cell with bottlebrush film after stepwise applying electric fields to extracts multiple relaxation modes of LC on bottlebrush surface. As a result, the PHMA and PMMA system have single and multiple relaxation mode, respectively. This indicating that the bottlebrush with frozen side chain offers relaxation associated with viscos LC; the bottlebrush with mobile side chains offers the relaxation mode with longer time scale as well as viscos LC corresponding to the bottlebrush with frozen side chains. Extraction the time evolution of LC between electrode where the electric field is lateral is future work. This may give benefit to improvement and functionalization of LC device.

7-5. Acknowledgment

All bottlebrushes were kindly supplied by Dainichiseika Color & Chemicals Mfg. Co., Ltd., Tokyo, Japan. The *V-T* curve measurement with LC cell was carried out in LG Japan lab co. (Tokyo, Japan). The author thanks Dr. Osamu Sato (Japan Advanced Institute of Science and Technology) for advice on *V-T* curve measurement,

7-6. References

1. Nespoulous, M.; Blanc, C.; Nobili, M. Ultraweak azimuthal anchoring of a nematic liquid crystal on a planar orienting photopolymer. *J. Appl. Phys.* **2007**, *102*, 073519.
2. Yamamoto, J.; Yokoyama, H.; Watanabe, J. Zero Surface Anchoring the Liquid Crystal Alignment Method and a Liquid Crystal Device. JP4053530B2, April 21, 2007.
3. Ramdane, O. O.; Auroy, P.; Forget, S.; Raspaud, E.; Martinot-Lagarde, P.; Dozov, I. I. Memory-Free Conic Anchoring of Liquid Crystals on a Solid Substrate. *Phys. Rev. Lett.* **2000**, *84*, 3871-3874.
4. Janossy, I. Kinetics of Director Gliding on a Polymer-Liquid-Crystal Interface. *Phys. Rev. E* **2010**, *81*, 031714.
5. Lee, J. H.; Yoon, T. H. Surface Gliding of the Easy Axis of a Polymer-Stabilized Nematic Liquid Crystal and its Dependence on the Constituent Monomers. *Phys. Rev. E: Stat., Nonlinear, Soft Matter Phys.* **2011**, *84*, 051701.
6. Sato, O.; Kasai, T.; Sato, M.; Sakajiri, K.; Tsujii, Y.; Kang, S.; Watanabe, J.; Tokita, M. High-Density Poly(hexyl methacrylate) Brushes Offering a Surface for Near-Zero Azimuthal Anchoring of Liquid Crystals at Room Temperature. *J. Mater. Chem. C* **2013**, *1*, 7992-7995.
7. Sato, O.; Iwata, N.; Kasai, T.; Tsujii, Y.; Kang, S. M.; Watanabe, J.; Tokita, M. Nematic Liquid Crystal Anchoring Strengths of High Density Polymer Brush Surfaces. *Liq. Cryst.* **2015**, *42*, 181-188.
8. Sato, O.; Okuno, H.; Adachi, I.; Watanabe, J.; Tokita, M.; Sakakibara, K.; Kinose, Y.; Goto, A.; Tsujii, Y. Novel In-Plane Switching Liquid Crystal Display with an Extremely High Transmittance Using a Well-Designed Bottlebrush as a Zero-Azimuth Anchoring Material. *Jpn. J. Appl. Phys.* **2019**, *58*, 066503.
9. Hu, M.; Xia, Y.; McKenna, G. B.; Kornfield, J. A.; Grubbs, R. H. Linear Rheological Response of a Series of Densely Branched Brush Polymers. *Macromolecules* **2011**, *44*, 6935-

6943.

10. Alexandris, S.; Peponaki, K.; Petropoulou, P.; Sakellariou, G.; Vlassopoulos, D. Linear Viscoelastic Response of Unentangled Polystyrene Bottlebrushes. *Macromolecules* **2020**, *53*, 3923-3932.

Summary

This thesis has dealt with two subjects, synthetic and molecular/structural studies on homo- and Janus-type cellulosic bottlebrushes in Part 1 and mechanistic studies on LC anchoring controlled by the dynamics characteristic to bottlebrushes in Part 2.

In **Chapter 1**, the background, purpose, and outline of this thesis were described.

In **Chapter 2**, new synthetic routes were established to synthesize the well-defined cellulosic bottlebrushes possessing two kinds of side chains at 2,3-*O* and 6-*O* positions with regioselectivity. The sequentially two-step grafting-to method was successfully achieved without spoiling mutual reactions and already introduced side chains. By this method, poly(ethylene glycol) (PEO) and polystyrene (PSt) were introduced to the cellulosic chain (PEO-PSt-cellulose) via the esterification and click reactions, respectively. The degrees of substitution of PEO and PSt (at 2,3-*O* and 6-*O* positions) were estimated to be 1.6 and ~1.0, respectively. Slightly insufficient substitution with PEO was considered to be due to imperfect dehydration, which was not intrinsic but will be improved by further dehydration of coupling reaction mixture. Another route developed in this chapter was the combination approach using the grafting-from polymerization followed by the grafting-to reaction: poly(ε-caprolactone) (PCL) was grown from the hydroxyl groups of the cellulose by the ring-opening polymerization, and then PSt was introduced by the same reaction as in the former method (PCL-PSt-cellulose). Both routes were demonstrated to successfully synthesize Janus-type bottlebrushes. The former is suitable for scaling up the reaction and achieving a higher molecular weight. By the similar strategies, homo-type cellulosic bottlebrushes with a single-component side chain regioselectively introduced, e.g., PSt at 6-*O* position (PSt-cellulose), was also synthesized and used as a reference for the Janus types in the following chapters.

In **Chapter 3**, the conformational study was carried out on the PSt-cellulose of different molecular weights in DMF. The cross-sectional radius of gyration (S_c^2) of the bottlebrushes was determined using the cross-sectional Guinier approximation with data obtained by small-angle X-ray scattering (SAXS) measurement, revealing that the radius was proportional to the molecular weight of side chain. This means that the side chains are in "collapsed state", which can be understood by sufficiently high density to prevent from forming a pear-necklace structure even in a poor solvent for the side chain. The main-chain conformation was analyzed using a wormlike chain model with data concerning the relationship between the radius of gyration (S^2) and the degree of polymerization of the main chain, which were obtained by size exclusion chromatography-multi angle light scattering measurement. The stiffness parameter of main chain of cellulosic bottlebrushes was equivalent to that of unsubstituted cellulose. This means that the excluded-volume effect among neighboring side chains was too small to affect the main-chain conformation of the cellulosic bottlebrush in a studied range of molecular weight of side chain. In other words, the original stiffness of cellulose chains was demonstrated to play a role in keeping a brush-like structure of side chains even in a poor solvent.

In **Chapter 4**, the intramolecular phase separation in PEO-PSt-cellulose was demonstrated with data of S_c^2 value determined by SAXS measurement. Then, the cross-sectional structure of PEO-PSt-cellulose was determined from the dependency of S_c^2 on the molecular weight of side chain assuming possible models. As a result, it was revealed that the two kinds of side chains of PEO-PSt-cellulose were phase-separated in a dilute solution of DMF, forming a Janus-type structure. To date, much less experimental analysis has been done on the microphase separation of a Janus-type bottlebrush in a dilute solution. Thus, this work should help to utilize the Janus-type bottlebrush as a building block.

In **Chapter 5**, the Janus-type cellulosic bottlebrush, PCL-PSt-cellulose, was confirmed

to form a high order structure in bulk. The structure was observed by SAXS and a transmission electron microscope (TEM). As a result, PCL-PSt-cellulose was microphase-separated into a lamellar structure when the PS/PCL volume fraction was around 50/50. For the sample stained with RuO_4, three distinguishable regions were observed by TEM and assigned to PSt domain and amorphous and crystal PCL domains, the latter two of which were also confirmed by the data of differential scanning calorimetry. This means that the PCL close to the cellulose backbone was restricted in its mobility and prohibited from crystalizing.

In **Chapter 6**, the mechanism of a weak anchoring of liquid crystal (LC) was investigated on the cross-linked films of bottlebrushes consisting of poly(hexyl methacrylate) (PHMA) and poly(ethyl methacrylate) (PEMA). The azimuthal anchoring coefficient A_2 was estimated for these two systems from the voltage-transmittance curve at different temperatures: the PHMA and PEMA systems gave a temperature-dependent weak anchoring property with A_2 decreasing in a lower-temperature range for the former. The degree of swelling of these two systems (crosslinked films) by the LC was determined and compared with the phase diagram for the corresponding mixtures without crosslinking, indicating that the degree of crosslinking was not so high to restrict the dynamics of bottlebrushes. To discuss the dynamics of the crosslinked bottlebrush, therefore, the rheological measurement was carried out for the LC mixture instead of LC-swollen crosslinked film, clearly demonstrating the relaxation of side chains in addition to the glass transition. Assuming the time scale for the A_2 determination, the characteristic temperature corresponding to the side-chain motion was evaluated, giving a reasonably good correlation with the A_2-decereasing temperature range. Finally, the author concluded that weak anchoring could be enhanced by the polymer-chain dynamics, which was expected to be accelerated by a bottlebrush structure as well as LC swelling (depending on the affinity of the bottlebrush component with the target LC). The knowledge gained in this study will aid in designing a novel

weak anchoring system by polymer coating.

In **chapter 7**, the relaxation of LC molecule on the cross-linked films of bottlebrushes consisting of PHMA and poly(mehyl methacrylate) (PMMA) was analyzed. In particular, the time evolution of the transmittance of in-plane LC cell with bottlebrush film after stepwise applying electric fields at different temperatures was recorded with high-speed camera equipped in polarized microscope and the data was analyzed with relaxation function. The PMMA system, the transmittance steeply increased and then become constant immediately after applying electric field. This time evolution was reproduced single exponential function, indicating this relaxation is related with viscous LC on bottlebrush film with frozen side chains. On the other hand, that of PHMA system at low temperature showed the transmittance steeply increased to some extent immediately after stepwise applying electric field and then gradually increased, while at higher temperature it displayed the time evolution similar to that of PMMA system. Those time evolutions of PHMA system were reproduced by triple exponential function. By combining the obtained results, the author considered that the extra two relaxation mode with longer time scale could be attributed to dynamics of side chain in cross-linked bottlebrush film and related to the change in easy axis. Additionally, the author estimated that the easy axis changed immediately after applying electric field in PHMA system at higher temperature, based on the relaxation time of the extra mode in PHMA system decreasing with temperature. in the future, this measurement method would bring new information about LC anchoring effect related with dynamics of bottlebrush polymer film because microscopy could extract the transmittance in area between electrodes where lateral electric field is applied.

List of Publication

chapter 2,

(1) Synthesis of cellulosic bottlebrushes with regioselectively substituted side chains and their self-assembly

K. Sakakibara, Y. Kinose, Y. Tsujii. *Cellulose Science and Technology* **2018**, 49-65.

chapter 3,

(2) Main-Chain Stiffness of Cellulosic Bottlebrushes with Polystyrene Side Chains Introduced Regioselectively at the *O*-6 Position

Y. Kinose, K. Sakakibara, H. Ogawa, and Y. Tsujii. *Macromolecules* **2019**, *52*, 8733–8740.

chapter 4,

(3) Intramolecular Microphase Separation of Janus-Type Cellulosic Cottlebrushes in Solution

Y. Kinose, K. Sakakibara, H. Ogawa, and Y. Tsujii. To be submitted.

chapter 5,

(4) Regioselective Synthesis of Cellulosic Janus Bottlebrushes with Polystyrene and Poly(ε-caprolactone) Side Chains and their Solid-State Microphase Separation

K. Sakakibara, H. Ishida, Y. Kinose, and Y. Tsujii. Submitted to Cellulose.

chapter 6,

(5) Near-zero Azimuthal Anchoring of Liquid Crystals Assisted by Viscoelastic Bottlebrush Polymers

Y. Kinose, K. Sakakibara, O. Sato, and Y. Tsujii. Submitted to ACS Appl. Mater. Interfaces.

chapter 7,

(6) Time Dependent and LC Anchoring and Bottlebrush Polymer Dynamics Revealed by High-Speed Polarized Microscopy

O. Sato, H. Okuno, I. Adachi, J. Watanabe, M. Tokita, K. Sakakibara, Y. Kinose, A. Goto and Y. Tsujii. *Japanese Journal of Applied Physics* **2019**, *58*, 066503.

Acknowledgements

The present investigations were carried out under the direction of Prof. Yoshinobu Tsujii at the Institute for Chemical Research (ICR), Kyoto University in the period from April 2012 to March 2021.

Firstly, author would like to express my sincerest gratitude to Prof. Yoshinobu Tsujii for his guidance, valuable discussion, and warm encouragement throughout this work. Grateful acknowledgement is due to Assoc. Prof. Kohji Ohno and Assist. Prof. Keita Sakakibara for their constructive guidance, valuable discussion and encouragement. I wish to express my appreciation to Prof. Mikihito Takenaka and Prof. Kazunari Akiyoshi (Department of Polymer Chemistry, Kyoto University) for their helpful advices on this thesis. I wish to acknowledge Prof. Osamu Sato (Japan Advanced Institute of Science and Technology) and Assoc. Prof. Hiroki Ogawa for their valuable discussion and technical support in part of the thesis.

The author is also thankful to all the members of Prof. Tsujii's Laboratory for their kind helps, particularly, to, Assoc. Prof. Kohji Ohno for his valuable suggestion and kind encouragement, and Mr. Hisayuki Ishida, Ms. Kimiyo Nakamichi and Mr. Moriki Yoshihito for their support in experiments.

Finally, the author wishes to express his heartfelt thanks to my parents Ms. Taeko Kinose and Hideo Kinose and his sister Ms. Yuko Suzuki for their continuous supports and encouragements.

March 2021

Yuji Kinose